

# **High-precision metrology with high-frequency nonclassical light sources**

Von der QUEST-Leibniz-Forschungsschule  
der Gottfried Wilhelm Leibniz Universität Hannover  
zur Erlangung des Grades

**Doktor der Naturwissenschaften  
Dr. rer. nat.**

genehmigte Dissertation  
von

**Dipl.-Phys. Timo Denker**

2016

Referent: Juniorprof. Dr. Michèle Heurs  
*QUEST, Universität Hannover*

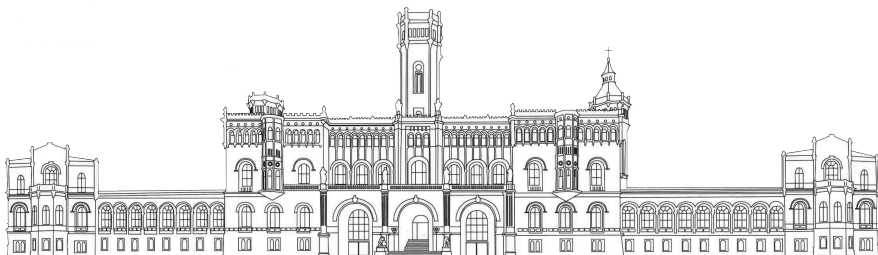
Korreferent: Prof. Dr. Karsten Danzmann  
*AEI, Universität Hannover*

Tag der Disputation 17.06.2016



Diese Arbeit wurde angefertigt am

Max-Planck-Institut für Gravitationsphysik  
(Albert-Einstein-Institut)  
und Institut für Gravitationsphysik,  
Leibniz Universität Hannover,  
Callinstrasse 38, 30167 Hannover, Germany





# Abstract

The first direct observation of a gravitational wave signal by a laser interferometric gravitational wave detector (GWD) impressively demonstrates the importance and potential of high-precision metrology. The injection of squeezed vacuum states (proposed by Caves) can increase the sensitivity in such a GWD. This leads to a reduction of quantum noise. Generally speaking, the quality of a measurement can be increased either by enhancing the signal or by decreasing the noise. In the context of interferometric GWD or precision spectroscopy, the former can be achieved by using a cavity with higher finesse or by up-shifting the signal of interest to a regime with less influence of technical noise via modulation techniques.

This thesis presents the development and implementation of a nonclassical light source for fundamental research in the fields of frequency stabilization and high-precision spectroscopy. A novel pump-phase locking technique that makes use of weak pump depletion (WPD) – an unavoidable effect that is usually neglected – in a sub-threshold optical parametric oscillator (OPO) is proposed and presented. The phase difference between the fundamental field at a wavelength of 1064 nm and the second-harmonic field at a wavelength of 532 nm is imprinted on both light fields by the nonlinear interaction in the crystal and is read out without disturbing the squeezed output. Our new locking technique allows for the first experimental realization of a pump-phase lock by reading out the pre-existing phase information in the pump field. A pump phase stabilization of the OPO via WPD locking while generating squeezed light at levels up to 2.5 dB has been achieved in this work.

In order to utilize the generated squeezed light for downstream experiments different stabilization setups to control the OPO and its pump phase are necessary. Different schemes to achieve this task are investigated.

This thesis presents the idea of an enhanced spectroscopy setup consisting of up-shifted signals via a cascaded phase modulation and a Fabry-Pérot cavity with squeezed light injection. A theoretical investigation of this scheme is presented, including the theoretical derivation

of the cavity dynamics and modeling of the expected variance of the up-shifted signals on a reduced noise floor, lowered by the introduced squeezed light. The experimental realization will result in improved high-precision phase measurements in cavity spectroscopy, with possible applications for cavity ring-down spectroscopy (CRDS), in the fields of optical frequency metrology or studies of light-matter interactions.

Keywords:

Squeezed states, Parametric oscillators, spectroscopy

# Kurzfassung

Die erste direkte Beobachtung eines Gravitationswellensignals durch ein laserinterferometrischen Gravitationswellendetektor (GWD) zeigt eindrucksvoll die Bedeutung und das Potential hochpräziser Metrologie. Die Implementierung von gequetschten Vakuumzuständen (vorgeschlagen von C. Caves) kann die Empfindlichkeit eines solchen GWDs durch Reduktion von Quantenrauschen weiter steigern. Prinzipiell kann die Qualität einer Messung entweder durch eine Verstärkung des Signals oder durch die Verringerung des Rauschens erhöht werden. Vor dem Hintergrund einer sensitiven Spektroskopie oder der interferometrischen Messung im GWD kann ersteres entweder durch die Verwendung eines Resonators mit höherer Finesse erreicht werden oder durch Verschieben des Signals mit Hilfe von Modulationstechniken in einen Frequenzbereich mit weniger Rauscheinflüssen. Diese Arbeit stellt die Entwicklung und Umsetzung einer nichtklassischen Lichtquelle für die Grundlagenforschung in den Bereichen Frequenzstabilisierung und hochpräzise Spektroskopie vor.

Im Rahmen dieser Arbeit wird eine neue Stabilisierungstechnik der Pumpphase eines unter dem Schwellwert betriebenen optischen parametrischen Oszillators (OPO) vorgestellt, die den schwachen Abbau des Pumpfeldes (*weak pump depletion*, WPD) – ein omnipräserter Effekt, der normalerweise vernachlässigt wird, – ausnutzt. Die Phase zwischen dem fundamentalen Feld bei 1064 nm und dem Pumpfeld bei 532 nm wird dabei durch die nichtlineare Wechselwirkung im Kristall auf beide Lichtfelder aufgeprägt und kann über das Pumpfeld ohne Störung der erzeugten gequetschten Zustände im fundamentalen Feld ausgelesen werden. Der mit dieser Technik erstmals in der Pumpphase stabilisierte OPO erzeugte Vakuumzustände von 2,5 dB.

Um die erzeugten gequetschten Zustände für weiterführende Experimente nutzen zu können, sind weitere Stabilisierungstechniken für den OPO und die Pumpphase notwendig. Diese hierfür erforderlichen Änderungen im experimentellen Aufbau werden gegenübergestellt und bewertet.

Darüber hinaus stellt diese Arbeit einen Spektroskopie-Aufbau vor, bestehend aus einer kaskadierten Phasenmodulation zur Frequenzver-

schiebung des Detektionssignals und einem Fabry-Pérot Resonator, der durch die Implementierung von gequetschten Vakuumzuständen rauschreduziert ist. In einer theoretischen Untersuchung des Resonatorverhaltens werden die frequenzverschobenen Signale und das reduzierte Rauschen simuliert. Die experimentelle Realisierung wird verbesserte hochpräzise Phasenmessungen ermöglichen und kann in der Cavity-ring-down-Spektroskopie (CRDS) Anwendung finden, z.B. im Bereich der optischen Frequenzmetrologie oder der Studie von Licht-Materie-Wechselwirkungen.

Schlagworte:

Gequetschtes Licht, Parametrischer Oszillator, Spektroskopie



# Contents

<b>Contents</b>	<b>ix</b>
<b>List of Figures</b>	<b>xiii</b>
<b>List of Tables</b>	<b>xvii</b>
<b>List of Abbreviations and Symbols</b>	<b>xix</b>
<b>1. Introduction</b>	<b>1</b>
<b>2. Quantum nature of light</b>	<b>7</b>
2.1. The electromagnetic field . . . . .	8
2.2. Quantization by canonical transformation . . . . .	10
2.2.1. The Hamiltonian of the electromagnetic field . . . . .	10
2.3. Quadrature operators . . . . .	11
2.3.1. Heisenberg's Uncertainty Principle (HUP) . . . . .	12
2.3.2. Linearization and fluctuations . . . . .	13
2.4. States of light . . . . .	14
2.4.1. States of light in phasor diagrams . . . . .	14
2.4.2. Vacuum State . . . . .	15
2.4.3. Number or Fock states . . . . .	15
2.4.4. Coherent states . . . . .	16
2.4.5. Squeezed states . . . . .	18
2.4.6. Coherent squeezed states . . . . .	22
2.5. Modulation of light . . . . .	23
2.5.1. Phase modulation . . . . .	24
2.5.2. Amplitude modulation . . . . .	25
2.5.3. Modulation in the sideband picture . . . . .	25
<b>3. Detection of light</b>	<b>29</b>
3.1. Direct detection with a single photodetector . . . . .	30
3.2. Balanced homodyne detection . . . . .	31
3.3. Self-homodyne detection . . . . .	33
3.4. Polarization-based homodyne detection . . . . .	34

## CONTENTS

3.5.	The influence of optical losses and detection efficiencies	35
3.5.1.	Homodyne mode mismatch . . . . .	37
<b>4.</b>	<b>Fundamentals of optical resonators</b>	<b>39</b>
4.1.	The two-mirror resonator: a linear Fabry-Pérot cavity	39
4.1.1.	Light field amplitudes . . . . .	40
4.1.2.	Properties and characteristics of a linear Fabry-Pérot cavity . . . . .	42
4.2.	Cavity dynamics . . . . .	46
4.2.1.	Equations of motion for light fields . . . . .	46
4.2.2.	Input-output formalism . . . . .	47
<b>5.</b>	<b>Cavity dynamics with <math>\chi^{(2)}</math> nonlinearities</b>	<b>51</b>
5.1.	Interaction with $\chi^{(2)}$ nonlinearities . . . . .	51
5.1.1.	Polarization density . . . . .	52
5.1.2.	Parametric down-conversion and second harmonic generation . . . . .	53
5.1.3.	Phase matching . . . . .	54
5.2.	Intracavity dynamics with interacting $\chi^{(2)}$ nonlinearities	58
5.2.1.	Hamiltonian and equations of motion . . . . .	58
5.2.2.	Noise variances in quadrature operators . . . . .	60
<b>6.</b>	<b>Generation of squeezed states</b>	<b>63</b>
6.1.	Frequency locking techniques . . . . .	64
6.1.1.	Cavity length control mechanisms . . . . .	64
6.1.2.	Pound-Drever-Hall locking . . . . .	65
6.1.3.	Dither locking . . . . .	66
6.1.4.	Polarization-based homodyne locking . . . . .	66
6.2.	Frequency stabilizing a cavity for frequency doubling .	69
6.2.1.	Frequency doubling in a linear cavity . . . . .	69
6.2.2.	Frequency doubling in a bow-tie cavity . . . . .	70
6.3.	Frequency stabilizing a cavity for parametric down conversion . . . . .	73
6.3.1.	The OPO cavity design consideration . . . . .	73
6.3.2.	Front lock of the OPO by polarization-based homodyne locking . . . . .	75
6.3.3.	Rear lock of the OPO with conventional PDH-lock	76
6.4.	Comparison of OPO frequency stabilization techniques	80

<b>7. Demonstration of weak pump depletion phase locking</b>	<b>83</b>
7.1. Theory of weak pump depletion . . . . .	84
7.1.1. Cavity dynamics . . . . .	85
7.1.2. The effect of WPD on squeezing and antisqueezing	87
7.1.3. Gain and losses . . . . .	88
7.2. Experimental realization . . . . .	89
7.2.1. Error signals . . . . .	91
7.3. Results . . . . .	93
7.3.1. Comparison between theory and experiment . .	96
7.4. Conclusion . . . . .	97
<b>8. High-precision metrology enhanced with squeezed light</b>	<b>99</b>
8.1. Squeezed states and signals at sideband frequencies . .	101
8.1.1. Signal modulation in the linear Fabry-Pérot cavity	101
8.1.2. Theory of squeezing and signals in Fourier space	104
8.1.3. Simulations of combined signal peaks and squeezed light in the linear Fabry-Pérot cavity . . . . .	108
8.2. The experimental setup . . . . .	110
8.2.1. Linear Fabry-Pérot cavity . . . . .	113
8.2.2. Polarization-based homodyne locking of a linear Fabry-Pérot cavity . . . . .	114
8.2.3. Tuning the free spectral range of the Fabry- Pérot cavity . . . . .	118
<b>9. Summary &amp; Outlook</b>	<b>121</b>
<b>A. Appendix</b>	<b>123</b>
A.1. Calculation of the nonlinearity factor with measure- ment values . . . . .	123
A.2. High frequency (homodyne) detectors . . . . .	124
A.2.1. Photodetector circuit . . . . .	126
A.2.2. High frequency bandwidth photodetector . . .	128
A.3. High FSR detection for multiplexing experiments . . .	129
A.3.1. Squeezing comb detection . . . . .	129
A.4. Theorems for the Fourier transformation . . . . .	131
A.4.1. Fourier transform of the Gaussian function . .	131
A.4.2. Derivation of the unit impulse function by sub- stitution . . . . .	132
<b>Bibliography</b>	<b>133</b>

*CONTENTS*

<b>Acknowledgements</b>	<b>143</b>
<b>Curriculum Vitae</b>	<b>145</b>
<b>Compendium of publications</b>	<b>147</b>

# List of Figures

2.1.	Different states of light in the quantum phasor picture	15
2.2.	Squeezed vacuum state of light . . . . .	20
2.3.	Squeezed states of light in the sideband picture . . . . .	21
2.4.	Displaced squeezed vacuum state of light . . . . .	23
2.5.	Plot of the phase-modulated electric field versus time .	24
2.6.	Plot of the amplitude-modulated electric field versus time	24
2.7.	Phase modulation of a coherent state in the sideband picture representation . . . . .	26
2.8.	Amplitude modulation of a coherent state in the sideband picture representation . . . . .	27
3.1.	Overview of different schemes for light detection . . .	30
3.2.	Schematic illustrating the detection of a light field with a beamsplitter . . . . .	36
3.3.	Resulting noise variances of the light field as a function of the detection efficiency for different input variances	37
4.1.	Schematic of light field amplitudes interacting with a cavity . . . . .	40
4.2.	Stability diagram for different resonator configurations	45
4.3.	Schematic of a bow-tie cavity for a detailed description of the different light fields . . . . .	46
5.1.	PDC and SHG in the energy and momentum pictures	54
5.2.	Phase-matching conditions in phasor representation .	56
5.3.	Schematic of a bow-tie cavity for a detailed description of the nonlinear interactions . . . . .	58
5.4.	Simulation of squeezed noise variances over several FSRs	61
5.5.	Plot of Eq. (5.15) for squeezed noise variances over several FSRs with introduced losses . . . . .	61
5.6.	Simulation of the squeezing and antisqueezing variances of the third FSR . . . . .	62

## LIST OF FIGURES

6.1. Schematical setup and error signal plot of Pound-Drever-Hall locking . . . . .	65
6.2. Schematic of polarization based homodyne locking setup	66
6.3. Measurement of error signal and cavity mode scan for polarization-based homodyne locking . . . . .	67
6.4. Schematic of the linear and the bow-tie cavity for frequency doubling . . . . .	69
6.5. Comparison of the performance of linear and bow-tie cavities for second-harmonic generation . . . . .	72
6.6. Schematic of the bow-tie cavity for optical parametric oscillation with cavity parameters . . . . .	73
6.7. Experimental setup of OPO frequency stabilization via front and rear lock I . . . . .	75
6.8. Experimental setup of OPO frequency stabilization via front and rear lock II . . . . .	77
6.9. Experimental setup of OPO frequency stabilization via front and rear lock III . . . . .	79
6.10. Comparison between front and rear lock . . . . .	80
7.1. Plot of detected variance of the OPO as a function of total loss . . . . .	89
7.2. Schematic overview of the experimental setup utilizing weak pump depletion for pump phase stabilization . .	90
7.3. Error signals for stabilizing the pump phase via weak pump depletion . . . . .	92
7.4. Simulation of the error signal for stabilizing the pump phase via weak pump depletion . . . . .	93
7.5. Zero span measurements of the shot noise levels . . . . .	94
7.6. Squeezing spectrum around the first FSR . . . . .	95
7.7. Plot of pump power . . . . .	96
8.1. Sideband pictures of the process of cascaded signal modulations in the linear Fabry-Pérot cavity . . . . .	102
8.2. Comparison between theory and measurement of OPO performance . . . . .	105
8.3. Simulations of signal peaks with a squeezed light field in a linear Fabry-Pérot cavity . . . . .	109
8.4. Schematic of the complete experimental setup . . . . .	111
8.5. Experimental setup of the FP cavity for sensitive optical phase shift measurements . . . . .	113

*LIST OF FIGURES*

8.6.	Schematic of a linear Fabry-Pérot cavity stabilized via polarization based homodyne locking . . . . .	114
8.7.	Plot of reflected fields of s- and p-polarization . . . . .	116
8.8.	Simulation of the intensities on both photodiodes in a homodyne detection setup . . . . .	116
8.9.	Simulation of the resulting error signal in a homodyne detection setup . . . . .	117
8.10.	Simulation of scanned sideband frequencies to find FSR of the Fabry-Pérot cavity . . . . .	118
8.11.	Measurements of tuned sideband frequencies to determine the FSR of the linear Fabry-Pérot cavity . . . . .	119
A.1.	Plot of the shot noise levels of the Australian high frequency homodyne detector over the full range of 2.5 GHz	124
A.2.	Plot of the shot noise levels of HFHD(v2) over the full range of 2.5 GHz . . . . .	125
A.3.	Schematic of the high frequency homodyne detector V2	127
A.4.	Plot of the transfer function of a broadband frequency photodetector . . . . .	128
A.5.	Plot of generated squeezing comb at different FSRs over a broad frequency range . . . . .	129
A.6.	Plot of generated squeezing comb at different FSRs over a broad frequency range . . . . .	130





# List of Tables

6.1. Comparison of frequency doubling in a linear and a bow-tie cavity . . . . .	72
6.2. Comparison of squeezing values . . . . .	81
7.1. Overview of the parameters characterizing the OPO. . . . .	91
8.1. Overview of the parameters characterizing the OPO and the frequency-shifted signal detection in the Fabry-Pérot cavity. . . . .	108



# List of Abbreviations and Symbols

AC	Alternate current
AR	Anti-reflection
BS	Beamsplitter
CRDS	Cavity ring-down spectroscopy
cw	Continuous-wave
DBS	Dichroic beamsplitter
DC	Direct current
EOM	Electro-optical modulator
FI	Faraday isolator
FWHM	Full width half maximum
GR	General theory of relativity
GWD	Gravitational wave detector
HD	(balanced) Homodyne detector
HR	High-reflection
HV Amp	High-voltage amplifier
HV	High voltage
HFHM	Half width half maximum
LiNbO <sub>3</sub>	Lithium niobate
LO	Local oscillator
MC	Mode cleaner cavity
Nd:YAG	Neodymium-doped yttrium aluminum garnet

## *List of Abbreviations and Symbols*

NPRO	Non-planar ring-oscillator
OPO	Optical parametric oscillation, optical parametric oscillator
PBS	Polarizing beamsplitter
PDC	Parametric down-conversion
PDH	Pound-Drever-Hall
PD	Photodetector
PPKTP	Periodically-poled potassium titanyl phosphate
PZT	Piezoelectric transducer
QPM	Quasi-phase-matching
QWP	Quarter-wave-plate
ROC	Radius of curvature
SHG	Second-harmonic generation
SNR	Signal-to-noise ratio
SQL	Standard quantum limit
SR	Special theory of relativity
TEM	Transverse electromagnetic Hermite Gauss
VIS	Visibility
WPD	Weak pump depletion
$\langle \hat{O} \rangle$	Expectation value of operator $\hat{O}$
$[\hat{A}, \hat{B}]$	Commutator of operators $\hat{A}$ and $\hat{B}$
$\hat{a}^\dagger$	Creation operator
$\hat{a}$	Annihilation operator
$\chi^{(2)}$	Second-order term in susceptibility
$\chi^{(3)}$	Third-order term in susceptibility

*List of Abbreviations and Symbols*

$\Delta^2\hat{O}, V(\hat{O})$	Variance of operator $\hat{O}$
$\Delta\hat{O}$	Standard deviation of operator $\hat{O}$
$\epsilon_0$	Electrical permeability
$E_n$	Energy eigenvalue
$\eta$	Total detection efficiency
$\eta_{\text{esc}}$	Escape efficiency
$\eta_{\text{prop}}$	Propagation efficiency
$\eta_{\text{homo}}$	Homodyne efficiency = VIS <sup>2</sup>
$\eta_{\text{qe}}$	Quantum efficiency of a photodiode
$\mathfrak{F}$	Finesse
$f$	Frequency
$\kappa$	Cavity decay rate
$h$	Planck constant
$\hbar = h/2\pi$	Reduced Planck constant
$\hat{\mathcal{H}}, \mathcal{H}$	Hamiltonian
$l$	Cavity round-trip length
$\mu_0$	Magnetic permeability
$P$	Laser power
$r$	Amplitude reflection coefficient
$R = r^2$	Power reflectivity
$\tau$	Cavity round-trip time
$t$	Amplitude transmission coefficient
$T = t^2$	Power transmittance
$\theta_{\text{b}}$	Phase angle (between seed and pump field)
$\omega$	Angular frequency

*List of Abbreviations and Symbols*

$\hat{X}_1 = \hat{X}^{\theta_b=0}$       Amplitude-quadrature operator

$\hat{X}_2 = \hat{X}^{\theta_b=\pi/2}$       Phase-quadrature operator

# 1

## Chapter 1

# Introduction

Over the past three decades, research on nonclassical light has come a long way. After its theoretical conception in 1976 by Yuen [Yue76], the first experimental realization by Slusher et al. [SHY<sup>+</sup>86] showed a mere 0.3 dB of noise reduction in this groundbreaking experiment. Nowadays, noise reduction of up to 12.7 dB below the vacuum level can be produced [ESB<sup>+</sup>10]. In the early 1980s the theoretical work on squeezed light was already well developed. In contrast, the experimental research in this area lagged significantly due to technical requirements for the nonlinear material and the detection devices. This gap between theory and experiment was aptly summarized by Marc D. Levenson at the seventh International Laser Spectroscopy Conference (ICOLS VII) on Maui in 1985: “(Squeezed) states have eluded experimental demonstration, at least so far. From an experimentalist’s point of view squeezed state research can be best described as a series of difficulties that must somehow be overcome”. He finished by listing “Nine difficulties” as future work proceedings [Yue83]. This list has been slowly but surely settled.

Nonclassical-light-enhanced gravitational wave detectors have become a cornerstone for gravitational wave astronomy [VKL<sup>+</sup>10]. The fact that 2015 was nominated as the “International Year of Light and Light-based Technologies” by the United Nations General Assembly (UNGA) and the first direct observation of a gravitational wave signal [CC16] by a laser interferometer emphasizes the significance of light and gravitation. This motivates a short review of the history of light and general relativity.

## 1. Introduction

---

“And God said, ‘Let there be light,’ and there was light”  
*Genesis 1:3*

In 1861 the Scottish physicist James Clerk Maxwell (1831 – 1879) published his work “On Physical Lines of Force” [Max61] which postulates the four well-known “Maxwell’s equations”. Today we refer to this formalism, which is nearly 150 years old, as the “classical” framework of electromagnetic theory. However, Albert Einstein doubted their validity and worked on alternative ideas involving quanta of light and the concept of relativity. This approach led to his proposal of the distribution of light in discrete wave packets called *photons* (for which he was awarded the Nobel Prize in Physics in 1921) and the special theory of relativity (SR). A hundred years ago, in November 1915, Albert Einstein presented his work on the general theory of relativity (GR) to the Prussian Academy of Sciences. Solutions to his “field equations” [Ein16b] describe the evolution of the universe on various scales, and postulate the existence of black holes and gravitational waves. An entirely new view of space and time was developed by Einstein, the so called *spacetime*, which up until that point had been figuratively considered a rigid stage of nature performing “its spectacular show” witnessed by us. Einstein’s theory with its groundbreaking insights changed this: colloquially speaking, the performance of nature affects the stage and in turn the stage itself affects the progress of the performance.

The field of gravitational physics reached yet another milestone recently, in February 2016. The gravitational-wave event GW150914<sup>1</sup>, detected on September 14th 2015, is a direct confirmation of one of the last remaining unproven predictions of general relativity, unlocking a new set of techniques for investigating the origins and evolution of our universe, namely *gravitational wave astronomy*. This first direct observation of a gravitational-wave signal was made by the interferometric gravitational-wave detectors (GWD) LIGO (**L**aser **I**nterferometer **G**ravitational-Wave **O**bservatory) in Hanford and Livingston [CC16]. The particular Michelson-type interferometer topology of gravitational-wave detectors (GWDs) allows for a tuning of the instrument’s sensitivity by the injection of nonclassical “squeezed” light. While the detectors that measured the first event, leading to this important discovery, were not equipped with squeezed-light injection, it has been demonstrated in the past that squeezed light increases the

---

<sup>1</sup>The abbreviation for “**G**ravitational **W**ave detected 2015-09-14”.



---

sensitivity of GWDs [MSM<sup>+</sup>02, AAA<sup>+</sup>13]. Therefore, it is a likely option for upgrades in the near future.

“Spacetime tells matter how to move; matter tells spacetime how to curve.”  
*John Archibald Wheeler*

Albert Einstein’s theory of GR [Ein16a] can be considered one of the most important scientific achievements in recent times. His approach was revolutionary in its ability to describe gravity, space, time and geometry. In Isaac Newton’s theory of universal gravitation [New87], gravity is a force between two massive objects, which points along the line intersecting both centers of masses. In contrast, Einstein’s theory describes the effect of gravity by the the curvature of spacetime. Einstein’s restated mathematical model describes a four-dimensional continuum by combining the common three-dimensional Euclidean space with the dimension of time. The curvature of spacetime leads to geodesics as an extension of the classical rules of geometry, where parallels never meet. Massive bodies curve the surrounding spacetime and their movement is determined as moving on straight lines in a now-curved spacetime. Due to this correlation, the motion of these massive bodies and the geometry of spacetime are in permanent evolution. As a consequence, Einstein predicted gravitational waves as perturbations in spacetime propagating at the speed of light [Ein16b]. In contrast to an electromagnetic wave, which propagates through spacetime and strongly interacts with matter, a gravitational wave is almost unperturbed by matter.

This establishes a completely new perspective in astronomy, which is traditionally based on electromagnetic radiation (and more recently, neutrinos) and thus confined to observable types of radiation in the electromagnetic spectrum. Therefore, it is impossible to observe the presence of dark matter or dark energy, or to detect anything from farther back than the time of photon decoupling in the recombination epoch. Gravitational wave observations could offer insight into the very early universe that was opaque to electromagnetic radiation. As gravitational waves interact only weakly with matter, they are long-range but also difficult to detect. The gravitational waves come in two polarization states,  $h_+$  and  $h_\times$ . If the gravitational wave propagates perpendicularly to the area spanned by a ring of test masses, the ring is compressed and stretched periodically in orthogonal directions. The amplitude of this compression and stretching is specified by its induced fractional length change, the so called *strain*  $h$ , given by  $h = \Delta L/L$

## 1. Introduction

---

with  $\Delta L$  as the length change over a given length  $L$ . The more energy per unit time the astrophysical event causing gravitational waves releases<sup>2</sup>, the larger the strain  $h$ . However, the signal in the first direct observation had a peak gravitational wave-strain of  $1.0 \times 10^{-21}$  [CC16]. Before the first direct detection was announced, there was only indirect evidence for the existence of gravitational waves. In 1993 Hulse and Taylor received the Nobel price for their studies of a pulsar in a binary neutron star system PSR B1913+16 [HT75]. Using pulsar timing measurements, they discovered a shift in the orbital period of the binary system over time. This suggested that the system must emit the predicted gravitational radiation [TW82, TW89].

Interferometric GWDs are a prominent example of ultra-high sensitivity metrology. Another field of applications that can also benefit from squeezed-light injection is spectroscopy based on laser light. It provides excellent opportunities to measure and study atoms and molecules. High-precision laser absorption spectroscopy, achieved by cavity ring-down spectroscopy (CRDS), allows measurements of the concentration of atoms and molecules in a dilute gas phase [PHS<sup>+</sup>98]. Typically, continuous wave (cw) laser light is injected into a resonator consisting of two low-loss mirrors, and the ring-down time of the cavity (the decay of the intracavity light field) is detected after the laser is switched off. If atoms or molecules are placed inside the cavity the decay rate decreases in a characteristic manner for the concentration or composition of the absorbing substance in the cavity. This is used in different fields of spectroscopy, such as studies of light-matter interactions [FSMA08] or optical frequency metrology [BSCH11]. The sensitivity in phase spectroscopy is in general limited by the ratio of the power of the detected signal of interest and the power of the noise. This is called *signal-to-noise ratio* (SNR). One can increase the SNR either by increasing the signal or by decreasing the noise. One can increase the signal by using a cavity with higher finesse or one can implement modulation techniques to up-shift the signal of interest to a regime with less influence of technical noise. If the desired signal (e.g. the interference signal in a GWD due to the fractional length change induced by a gravitational wave) is very small and cannot be enhanced, then the other option is to reduce the noise floor. If the noise is already at the quantum limit the use of nonclassical light can further increase the sensitivity of the spectroscopic measurement.

---

<sup>2</sup>For example, all forms of compact binaries, supernovae or rotating neutron stars create such waves.

---

Since nonclassical light offers a sub-shot-noise measurement by a low-noise homodyne detector with a strong local oscillator (LO) [LPS<sup>+</sup>98] a possible combination of techniques is imaginable. Using squeezed light at higher free spectral ranges (FSRs) superimposed with the up-converted signal of interest the SNR can be increased significantly, leading to higher sensitivity of the spectroscopic method.

## Structure of this thesis

This thesis examines nonlinear light sources and their implementation for high-precision phase measurements. For this purpose, a sub-threshold bow-tie optical parametric oscillator (OPO) was locked via a completely novel stabilization scheme utilizing weak pump depletion that arises from the interaction of the light fields in the nonlinear crystal. Besides the implementation of squeezed states of light in future gravitational wave detectors, there are other relevant applications at the quantum noise limit including atomic force microscopy [PDGVHG92], spectroscopy [PCK92], and cavity enhanced absorption spectroscopy [LLW<sup>+</sup>08]. In one of the experiments described in this thesis, the squeezed light field was combined in a high-finesse Fabry-Pérot (FP) cavity with a signal of interest that was up-shifted to higher free spectral ranges (FSR) of the OPO (and simultaneously the FP cavity) via an electro-optical modulator (EOM). This signal is masked by technical baseband noise and only manifests itself at higher FSRs due to the absence of technical noise and the reduced noise floor, which is suppressed by the introduced squeezed light. Using a high-frequency photodetector, measurements of several FSRs of the nonclassical light source were possible and a “squeezing comb” was detected. Having several squeezing ports available makes multiplexed entanglement possible, which has possible applications in quantum communication.

Chapter 2 describes the mathematical and theoretical background of quantum optics. The nature of light in its different manifestations (or states) is described, and different visualizations are presented. Special attention is placed on the modulation of light which is required for error signal generation and stabilization purposes.

Chapter 3 contains the formalism of quantum optics related to the detection of light fields and their variances.

Chapter 4 gives a theoretical quantum optical description of cavity dynamics in general. Furthermore, the input-output-formalism for the cavity dynamics is derived, following [WM07].

## 1. Introduction

---

In Chapter 5 the  $\chi^{(2)}$  susceptibility term for the nonlinear interaction of light and matter is introduced to describe frequency-doubled light and squeezed states. The cavity dynamics are expanded by the nonlinear interaction terms. Based on this, different cases are considered: cavity dynamics with and without depletion of the pump field and cavity behavior off-resonance for investigation of signals at frequencies corresponding to higher free spectral ranges of the cavity.

Chapter 6 introduces different schemes for stabilizing a resonator to control the sub-threshold bow-tie OPO and its pump phase in the experimental setup for this work. Several experimental approaches are presented and compared.

In Chapter 7 a detailed discussion of a novel locking scheme utilizing weak pump depletion is given. The theoretical background and experimental realization are explained and the achieved squeezing level is presented and discussed.

Chapter 8 details an advanced experimental setup with the generated squeezed states for cavity-enhanced spectroscopy. In this representation the main components are described in detail. Particular emphasis is placed on the theory of cavity-enhanced spectroscopy with a high finesse FP cavity and squeezed-light injection.

Chapter 9 concludes this thesis with a summary of the experiments combining the simulations and the measured results. It also presents an outlook on possible improvements and extensions for future research.

# 2

## Chapter 2

# Quantum nature of light

Initially described as an electromagnetic wave by James Clerk Maxwell, the Hamiltonian of an electromagnetic field is established in this chapter followed by its quantization where the operator formalism is introduced. The quantization of light implies a change in paradigm. Light is not only a continuous wave but consists of quanta, so-called *photons*. This concept is called *wave-particle duality*. Adopting the photon picture in the context of high precision measurements, a statistical treatment of photon counting is essential. A classic example for the corresponding quantum noise is continuous measurement by simple detection of the electromagnetic amplitude with a photodetector. The result is a Poissonian distribution for the number of photons counted. This quantum noise limits the accuracy of many experiments that rely on measurements of the electric field. As we shall see, the quantum nature of light allows us, however, to redistribute the associated uncertainty between different degrees of freedom of the field and thus reduce the quantum noise in the domain of interest.

This chapter deals with the quantum mechanical treatment of light and introduces the mathematical description for electromagnetic field theory. Although we can purely physically motivate the quantization of light [BBB15] this chapter examines the common, more abstract derivation of the quantization by a vector potential in the Coulomb gauge. The quantization of this light field leads to its description with quadrature operators which are determined by the Heisenberg uncertainty principle. This inequality establishes a fundamental limit of uncertainty for measuring two non-commuting variables/quadratures. It is possible to decrease the uncertainty (noise) in one quadrature at the expense of increasing the noise in the other, thus preserving the

## 2. Quantum nature of light

---

validity of the Heisenberg uncertainty principle. These quadratures span a vector space for a so-called *phasor diagram* to visualize the amplitude and noise distribution of light. By means of that phasor diagram different states of light and their modifications in terms of phase or amplitude modulations are explained.

### 2.1. The electromagnetic field

The electromagnetic interaction is one of the four fundamental forces in addition to gravitation, and the weak and strong interactions. This field is composed of an electric field induced by stationary charges and a magnetic field induced by moving charges. The standard quantum optics formalism used in this chapter can be found in text books [WM07].

#### Maxwell equations and the vector potential

To investigate a light field freely propagating in space we start with the classical electromagnetic field equations in vacuum:

$$\begin{aligned}\nabla \cdot \mathbf{B} &= 0, \\ \nabla \cdot \mathbf{E}\epsilon_0 &= 0, \\ \nabla \times \mathbf{E} &= -\frac{\partial \mathbf{B}}{\partial t}, \\ \nabla \times \mathbf{B} &= \epsilon_0\mu_0\frac{\partial \mathbf{E}}{\partial t},\end{aligned}\tag{2.1}$$

where  $\mathbf{E}$  is the electric field (a vector field) and  $\mathbf{B}$  is the magnetic field<sup>1</sup> and  $\epsilon_0$  and  $\mu_0$  are the electric permittivity of free space and magnetic permeability, which satisfy  $\mu_0\epsilon_0 = 1/c^2$ .

The electric field  $\mathbf{E}$  and the magnetic field  $\mathbf{B}$  from Eq. (2.1) can be expressed in terms of a vector potential  $\mathbf{A}(\mathbf{r},t)$ . Due to the nature of the equations,  $\mathbf{A}(\mathbf{r},t)$  is not uniquely defined but allows for so called *gauge transformations*, which leave the physical equations for the fields unaltered, but can reasonably simplify calculations in the context of quantum optics. Using the Coulomb gauge fixing condition  $\nabla \cdot \mathbf{A}(\mathbf{r},t) = 0$  the introduced vector potential  $\mathbf{A}(\mathbf{r},t)$  defines the electric field and

---

<sup>1</sup>For convenience in all equations vectors are written in **bold** letters in the following work.

the magnetic field as follows:

$$\begin{aligned}\mathbf{B} &= \nabla \times \mathbf{A}, \\ \mathbf{E} &= -\frac{\partial \mathbf{A}}{\partial t}.\end{aligned}\tag{2.2}$$

By substituting Eq. (2.2) into Eq. (2.1), the Maxwell equations have been used to obtain the wave equation in terms of this vector potential  $\mathbf{A}(\mathbf{r}, t)$  of the electromagnetic field:

$$\nabla^2 \mathbf{A}(\mathbf{r}, t) = \frac{1}{c^2} \frac{\partial^2 \mathbf{A}(\mathbf{r}, t)}{\partial t^2}.\tag{2.3}$$

Plane waves are one such solution to Eq. (2.3) and it is customary to use the standing waves of a cubic volume of sidelength  $L$ :

$$\mathbf{u}(\mathbf{r}) = \frac{1}{L^3} \mathbf{h}_{\text{pol}} e^{i\mathbf{k}\mathbf{r}},\tag{2.4}$$

with  $\mathbf{h}_{\text{pol}}$  as the polarization vector and  $\mathbf{k}$  as the wave vector of the electromagnetic wave. This gives us the vector potential of the electromagnetic field:

$$\mathbf{E}(\mathbf{r}, t) = i \sum_k \left( \frac{\hbar \omega_k}{2\epsilon_0} \right)^{\frac{1}{2}} [a_k \mathbf{u}(\mathbf{r}) e^{-i\omega_k t} - a_k^* \mathbf{u}(\mathbf{r})^* e^{+i\omega_k t}],\tag{2.5}$$

where  $a_k$  and its complex conjugate are the dimensionless, complex Fourier field amplitudes.

### Paraxial approximation for Gaussian beams

According to [KL66] light that is propagating along the  $z$ -axis with narrow amplitude distribution can be represented as a plane wave with an envelope function

$$u(r, z) = e^{-i\left(P + \frac{k}{2q} r^2\right)} e^{-ikz},\tag{2.6}$$

where  $r = \sqrt{x^2 + y^2}$  and  $k = 2\pi/\lambda$  is the magnitude of the wave vector. This illustrates how the Gaussian fundamental beam differs from regular plane waves. The complex parameters  $P$  and  $q$  describe the beam expansion and curvature evolution of the wave front over the distance of propagation [KL66]. Recasting the parameter  $q$  into the

## 2. Quantum nature of light

---

two real parameters ROC (radius of curvature) and  $w$  (beam radius) leads to the familiar definition of

$$u(r, z) = \frac{w_0}{w} e^{-\frac{r^2}{w^2}} e^{-i\frac{kr^2}{2\text{ROC}}} e^{-i(kz-\phi)}, \quad (2.7)$$

where  $\phi$  is called the Gouy phase and  $w_0$  is the waist of the beam (it is the beam radius at its narrowest point).

### 2.2. Quantization by canonical transformation

Characterizing the single, discrete levels of energy of a light field by the harmonic oscillator leads to the introduction of the creation ( $\hat{a}^\dagger$ ) and annihilation operators ( $\hat{a}$ ). These operators decrease and increase the energy in the light field by adding or subtracting single photons from the ensemble.

The normalization factors in Eq. (2.5) have been chosen such that the amplitudes  $a_k$  and  $a_k^*$  are dimensionless. In classical electromagnetic theory these Fourier amplitudes are complex numbers. The normalized complex amplitude function  $\mathbf{u}(\mathbf{r}) = u_0(\mathbf{r})e^{i\phi(\mathbf{r})}$  contains the phase information of the wavefront as well as the absolute phase with respect to a reference wave. By transforming these complex amplitudes into pairwise Hermitian adjoint operators the electromagnetic field reads, in its quantized form, as:

$$\mathbf{E}(\mathbf{r}, t) = i \sum_k \left( \frac{\hbar\omega_k}{2\epsilon_0} \right)^{\frac{1}{2}} \left[ \hat{a}_k \mathbf{u}(\mathbf{r}) e^{-i\omega_k t} - \hat{a}_k^\dagger \mathbf{u}(\mathbf{r})^* e^{+i\omega_k t} \right]. \quad (2.8)$$

As photons are bosons the annihilation and creation operators  $a_k$  and  $a_k^\dagger$  obey the bosonic commutation relations:

$$[\hat{a}_k, \hat{a}_{k'}] = [\hat{a}_k^\dagger, \hat{a}_{k'}^\dagger] = 0, \quad [\hat{a}_k, \hat{a}_{k'}^\dagger] = \delta_{kk'}. \quad (2.9)$$

#### 2.2.1. The Hamiltonian of the electromagnetic field

The classical Hamiltonian describing the total energy of the electromagnetic field from Eq. (2.5) is given by

$$\mathcal{H} = \frac{1}{2} \int_V \left( \epsilon_0 \mathbf{E}^2 + \frac{\mathbf{B}^2}{\mu_0} \right) d^3\mathbf{r}, \quad (2.10)$$



### 2.3. Quadrature operators

where  $\epsilon_0$  is the electric permittivity of free space,  $\mu_0$  is the magnetic permeability and  $\mathbf{E}$  and  $\mathbf{B}$  are the amplitudes of the electric and magnetic field. Similarly the Hamiltonian can be canonically transformed into the following form:

$$\hat{\mathcal{H}} = \sum_k \hbar\omega_k \left( \hat{a}_k^\dagger \hat{a}_k + \frac{1}{2} \right), \quad (2.11)$$

where the product of the annihilation operator  $\hat{a}$  and creation operator  $\hat{a}^\dagger$  represents the photon number operator  $\hat{a}_k^\dagger \hat{a}_k = \hat{n}_k$ . Multiplied by the photon energy  $\hbar\omega_k$  one can find each energy level of the  $k$  modes and in addition to the energy of vacuum fluctuations  $\hbar\omega_k/2$ .

### 2.3. Quadrature operators

The bosonic commutation relations (see Eq. (2.9)) reveal a big difference in the classical and quantum optics approach. Since the classical complex Fourier amplitudes in Eq. (2.5) commute they prevail as observables and consequently are detectable. In quantum mechanics operators must be Hermitian ( $\hat{X}_1 = \hat{X}_1^\dagger$ ) to describe physical observables. However, with the annihilation and creation operators ( $\hat{a}$ ,  $\hat{a}^\dagger$ ) one can construct the Hermitian adjoint amplitude quadrature operator  $\hat{X}_1$  and phase quadrature operator  $\hat{X}_2$ :

$$\begin{aligned} \hat{X}_1 &= \hat{a} + \hat{a}^\dagger, \\ \hat{X}_2 &= i(\hat{a} - \hat{a}^\dagger), \end{aligned} \quad (2.12)$$

which leads to the modified equation for the electromagnetic field:

$$\mathbf{E}(\mathbf{r}, t) = i \sum_k \left( \frac{\hbar\omega_k}{2\epsilon_0} \right)^{\frac{1}{2}} \left[ \hat{X}_1 \cos(\omega t) - \hat{X}_2 \sin(\omega t) \right]. \quad (2.13)$$

The inverse quadrature operator relations for the annihilation and creation operators are:

$$\begin{aligned} \hat{a} &= \frac{1}{2} (\hat{X}_1 - i\hat{X}_2), \\ \hat{a}^\dagger &= \frac{1}{2} (\hat{X}_1 + i\hat{X}_2). \end{aligned} \quad (2.14)$$

From Eq. (2.13) it is evident that these quadrature operators correspond to oscillating field amplitudes with a phase shift of  $90^\circ$  with

## 2. Quantum nature of light

---

respect to each other. The phase of the field is then defined as the phase angle  $\phi$  with respect to the amplitude quadrature, given by

$$\phi = \tan^{-1} \left( \frac{\hat{X}_2}{\hat{X}_1} \right). \quad (2.15)$$

Because the amplitude and phase quadratures are constructed by  $\hat{a}$  and  $\hat{a}^\dagger$ , they are equally non-commuting (see Eq. (2.9)). This gives rise to the commutation relation  $[\hat{X}_1, \hat{X}_2] = \hbar i = 2i$  (where the Planck constant is set to 2 due to normalization). A linear combination of  $\hat{X}_1$  and  $\hat{X}_2$  is used to define an operator for any quadrature angle  $\vartheta$ :

$$\begin{aligned} \hat{X}_\vartheta &= \hat{X}_1 \cos(\vartheta) + \hat{X}_2 \sin(\vartheta) \\ &= \hat{a}^\dagger e^{i\vartheta} + \hat{a} e^{-i\vartheta}. \end{aligned} \quad (2.16)$$

### 2.3.1. Heisenberg's Uncertainty Principle (HUP)

In his uncertainty principle [GD08] Heisenberg determines the fundamental limit of the accuracy of simultaneous measurements on both quantities of a pair of non-commuting observables A and B that obey the commutation relation  $[\hat{A}, \hat{B}] = C$ . Measuring one observable with higher precision comes at the cost of a decreased precision in the other according to the uncertainty relation:

$$\Delta \hat{A} \Delta \hat{B} \geq \frac{|C|}{2}, \quad (2.17)$$

where the standard deviation of the operator  $\hat{A}$  is defined as

$$\Delta \hat{A} = \sqrt{\langle \hat{A}^2 \rangle - \langle \hat{A} \rangle^2}, \quad (2.18)$$

and  $\hat{B}$  accordingly. Applying Eq. (2.17) to the quadrature operators of the electromagnetic field the HUP states that

$$\Delta \hat{X}_1 \Delta \hat{X}_2 \geq 1. \quad (2.19)$$

For  $\Delta \hat{X}_1 = \Delta \hat{X}_2 = 1$  the standard deviation of phase and amplitude quadrature has its minimum of quantum fluctuation. States fulfilling this limit are called *minimum uncertainty states*. The squeezed states described in Sec. 2.4.5 are a special class of minimum uncertainty states. Although the uncertainty is not equally distributed amongst the phase and amplitude quadratures, squeezed states must also obey the HUP.

### 2.3.2. Linearization and fluctuations

With the help of the linearization formalism [Yur84] operators can be decomposed into two parts: the steady-state component is time independent and represented by a complex number, whereas the time-varying component is represented by a fluctuation operator. The annihilation and creation operators take the form:

$$\begin{aligned}\hat{a}(t) &= \alpha + \delta\hat{a}(t), \\ \hat{a}^\dagger(t) &= \alpha^* + \delta\hat{a}^\dagger(t),\end{aligned}\tag{2.20}$$

where the complex numbers  $\alpha$  and  $\alpha^*$  are the steady state expectation values of the field operators, which are equivalent to the amplitudes of the light field in classical physics. For convenience the time dependence of this operator is omitted in the following sections. This approximation does not affect the operator relations of the quadrature operators:

$$\begin{aligned}\hat{X}_1 &= X_1 + \delta\hat{X}_1 \\ &= (\alpha + \alpha^*) + (\delta\hat{a} + \delta\hat{a}^\dagger), \\ \hat{X}_2 &= X_2 + \delta\hat{X}_2 \\ &= i(\alpha - \alpha^*) + i(\delta\hat{a} - \delta\hat{a}^\dagger).\end{aligned}\tag{2.21}$$

Determining the variance of the quadrature operators to be  $V = \Delta^2 \hat{X}_o \equiv \langle |\Delta \hat{X}_o|^2 \rangle - \langle |\Delta \hat{X}_o| \rangle^2$  Eq. (2.21) leads to the following variances of the quadrature operators:

$$\begin{aligned}\Delta^2 \hat{X}_1 &= \left\langle \left( \delta\hat{a} + \delta\hat{a}^\dagger \right)^2 \right\rangle = \left\langle \left( \delta\hat{X}_1 \right)^2 \right\rangle, \\ \Delta^2 \hat{X}_2 &= \left\langle \left( -i\delta\hat{a} + \delta\hat{a}^\dagger \right)^2 \right\rangle = \left\langle \left( \delta\hat{X}_2 \right)^2 \right\rangle.\end{aligned}\tag{2.22}$$

The detection of a light field is directly related to the number of photons. Therefore, the number operator needs to be linearized to investigate its fluctuating behavior

$$\begin{aligned}\hat{n} &= \hat{a}^\dagger \hat{a} \\ &= \alpha^2 + \alpha \left( \delta\hat{a} + \delta\hat{a}^\dagger \right) + \mathcal{O}(\delta^2) \\ &= \alpha^2 + \alpha \delta\hat{X}_1.\end{aligned}\tag{2.23}$$

This shows that for a coherent light field the fluctuations around a mean value scale with the mean value itself.

### 2.4. States of light

The laser light field and its noise distribution are the basis for almost every quantum optics experiment. For a better understanding of the various states of light it is useful to have a picture in mind. The linearized formalism of the quantum mechanical operators in Eq. (2.20) leads to two complementary visualizations. Firstly, the quantum phasor picture (so-called “*ball-on-a-stick*” picture) explains the different states of light with their noise contributions. It is an extended form of the phasor diagram of an electromagnetic field well-known from classical physics. The ball on top of the classical steady-state field phasor visualizes the Gaussian-distributed quantum noise in the phase space formulation. The dashed contour circle represents the variance of the Gaussian-distributed quantum noise (see [GZ04]). This representation is used in Sec. 2.4 to describe the different states of light.

Secondly, the sideband picture is introduced to understand the concepts of amplitude and phase modulation of a light field. In this frequency domain picture the frequency of the light acts as a reference, the so-called “carrier”. By choosing the coordinate system in such a way that it is rotating with the same frequency one obtains a stationary picture. In this *rotating frame* [GC85] every other frequency term (modulation, randomly noise distribution) is represented by a sideband that rotates clockwise or counter-clockwise with respect to the carrier frequency. This representation is used in Sec. 2.4.5 and Sec. 2.5.3.

#### 2.4.1. States of light in phasor diagrams

For a better understanding of the mathematical descriptions of the different states of light it is useful to illustrate the physical conditions (see Fig. 2.1). Analogous to the phasor representation in electrical engineering or classical field theory, the steady state amplitude and the phase of a certain state of light are depicted by a vector in the complex plane and the angle of the vector to the amplitude axis [L<sup>+</sup>98]:

$$\alpha = \alpha_0 e^{i\theta}. \quad (2.24)$$

The Gaussian-distributed quantum noise (quasi-probability distribution function) is often shown by a “blurry ball” on top of the arrow with a dashed circle indicating its uncertainty fluctuations.

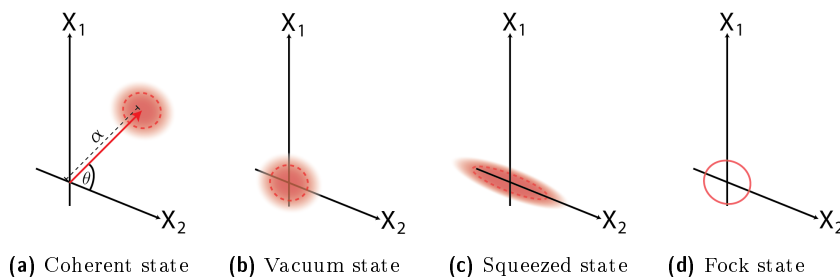


**Figure 2.1.:** Different states of light in the quantum phasor picture. (a) A coherent state with a certain amplitude  $\alpha$  (the classical steady-state field phasor depicted by the red arrow) and a phase  $\theta$  corresponding to the angle with respect to the amplitude quadrature axis. The Gaussian distributed quantum noise (quasi-probability distribution function) is depicted by a blurry “ball” with a dashed circle marking its variance. (b) Without an amplitude (arrow) only the noise distribution remains. This is called the vacuum state. (c) If this quantum noise is not equally distributed among the phase and amplitude quadrature, it is described as a squeezed state. (d) One particular non-classical state of light is the Fock state or number state. Due to the well-defined number of quanta the blurry ball of the noise distribution becomes exactly the circle of the distribution variance.

### 2.4.2. Vacuum State

The vacuum state (or ground state)  $|0\rangle$  represents the field in its photon-less state, with minimal quantum-limited fluctuations [GK05]. It has no coherent amplitude, i.e.  $\alpha = \alpha^* = 0$  (see Eq. (2.20)). In the phasor picture, the vacuum state is just the “ball” of Gaussian-distributed quantum noise without the “stick” (see Fig. 2.1b).

Vacuum fluctuations play a significant role in every quantum optics experiment as they couple in whenever optical loss is introduced. Beyond occupying an unused optical port of a beamsplitter, the vacuum field replaces every part of the light field that is lost due to absorption or scattering [McK08].

### 2.4.3. Number or Fock states

We describe the electromagnetic field by its Hamiltonian (Eq. (2.11)) to highlight the information of the energy level for one single mode of  $k$  modes. Denoting  $|n\rangle$  as the mode’s energy eigenstate with its energy eigenvalue  $E_n$  leads to the eigenvalue equation of the harmonic

## 2. Quantum nature of light

---

oscillator [GK05]:

$$\hat{\mathcal{H}}|n\rangle = \hbar\omega \left( \hat{n} + \frac{1}{2} \right) |n\rangle = E_n |n\rangle. \quad (2.25)$$

The same eigenstates can be expressed as eigenstates of the number operator as follows:

$$\hat{n}|n\rangle = n|n\rangle, \quad (2.26)$$

where  $n$  is a non-negative integer describing the number of photons in that eigenstate.

The annihilation and creation operators  $\hat{a}$  and  $\hat{a}^\dagger$  act in the same way on the energy eigenstate and on the number state: they decrease or increase the photon mode number respectively by lowering or raising the energy level of the new corresponding eigenstate

$$\begin{aligned} \hat{\mathcal{H}}(\hat{a}|n\rangle) &= (E_n - \hbar\omega)(\hat{a}|n\rangle), \\ \hat{\mathcal{H}}(\hat{a}^\dagger|n\rangle) &= (E_n + \hbar\omega)(\hat{a}^\dagger|n\rangle). \end{aligned} \quad (2.27)$$

Normalizing the new lower and higher number eigenstates leads to

$$\begin{aligned} \hat{a}|n\rangle &= \sqrt{n}|n-1\rangle, \\ \hat{a}^\dagger|n\rangle &= \sqrt{n+1}|n+1\rangle. \end{aligned} \quad (2.28)$$

With these results it becomes apparent that every arbitrary number state can be produced by iterative application of the creation operator  $\hat{a}^\dagger$  to the ground state  $|0\rangle$ :

$$|n\rangle = \frac{(\hat{a}^\dagger)^n}{\sqrt{n!}}|0\rangle. \quad (2.29)$$

These special states are called number states or Fock states. Due to the well-defined number of quanta the blurry ball of the noise distribution becomes exactly the circle of the distribution variance (see Fig. 2.1d).

### 2.4.4. Coherent states

While a Fock state is well suited to describe a low photon count number field, the coherent state more suitably represents high photon number light fields, such as those generated by continuous wave lasers. Coherent states are an eigenstate of the annihilation operator  $\hat{a}$  and

## 2.4. States of light

have the minimal quantum limited fluctuations which are equally distributed in both amplitude and phase quadratures:  $\Delta X_1 = \Delta X_2 = 1$ . In the phasor picture the coherent state is described by a certain amplitude  $\alpha$  (the classical steady-state field phasor depicted by the red arrow, see Fig. 2.1) and a phase  $\theta$  corresponding to the angle of the arrow to the amplitude quadrature axis (see Eq. (2.24)). The Gaussian-distributed quantum noise (quasi-probability distribution function) is depicted by the blurry “ball” with the dashed circle marking the variance of the noise distribution (see Fig. 2.1a). The eigenvalue relation for a coherent state  $|\alpha\rangle$  is [Gla63]:

$$\hat{a}|\alpha\rangle = \alpha|\alpha\rangle, \quad (2.30)$$

where the eigenvalue  $\alpha$  is a complex number. By following the approach of [GK05], a coherent state can be expanded in the basis of Fock states as follows

$$|\alpha\rangle = e^{-\frac{|\alpha|^2}{2}} \sum_{n=0}^{\infty} \frac{\alpha^n}{\sqrt{n!}} |n\rangle. \quad (2.31)$$

### The coherent state as a displaced vacuum state

In addition to the previous two definitions there is a third way of defining the coherent state. It can also be generated by letting the displacement operator act on the vacuum state  $|0\rangle$

$$\hat{D}(\alpha)|0\rangle = |\alpha\rangle, \quad (2.32)$$

where the displacement operator is defined as

$$\hat{D}(\alpha) = e^{(\alpha\hat{a}^\dagger - \alpha^*\hat{a})}. \quad (2.33)$$

By means of the disentangling theorem [GK05]  $\hat{D}(\alpha)$  can be expressed as

$$\hat{D}(\alpha) = e^{-\frac{|\alpha|^2}{2}} e^{\alpha\hat{a}^\dagger} e^{-\alpha^*\hat{a}}. \quad (2.34)$$

## 2. Quantum nature of light

---

Applying this form of the displacement operator to the vacuum state leads to the familiar definition from Eq. (2.31):

$$\begin{aligned}
 |\alpha\rangle &= \hat{D}(\alpha)|0\rangle \\
 &= e^{-\frac{|\alpha|^2}{2}} \sum_{n=0}^{\infty} \frac{\alpha^n}{n!} (\hat{a}^\dagger)^n \sum_{l=0}^{\infty} \frac{(\alpha^* \hat{a})^l}{l!} |0\rangle \\
 &= e^{-\frac{|\alpha|^2}{2}} \sum_{n=0}^{\infty} \frac{\alpha^n}{n!} (\hat{a}^\dagger)^n |0\rangle \\
 &= e^{-\frac{|\alpha|^2}{2}} \sum_{n=0}^{\infty} \frac{\alpha^n}{\sqrt{n!}} |n\rangle.
 \end{aligned} \tag{2.35}$$

The displacement operator therefore generates coherent states from the vacuum state.

### 2.4.5. Squeezed states

There are states whose quadratures defined by Eq. (2.16) can be smaller than vacuum noise. It is possible to decrease the uncertainty noise in one quadrature at the expense of increasing the noise in the other quadrature, preserving the validity of the HUP (see Fig. 2.1c). To derive such a squeezed state in this section, we follow [GK05]. Based on the operator for any quadrature defined by its angle  $\vartheta$  (see Eq. (2.16)) a quadrature-squeezed state must satisfy:

$$\left\langle \left[ \Delta \hat{X}_\vartheta \right]^2 \right\rangle < 1. \tag{2.36}$$

This squeezed quadrature has a standard deviation that is less than the minimum fluctuation uncertainty. To preserve the validity of the HUP the standard deviation of its associated operator must be greater by at least the reciprocal factor  $x_{\text{sqz}}$ :

$$\begin{aligned}
 \Delta \hat{X}_1 = \frac{1}{x_{\text{sqz}}} \quad \wedge \quad \Delta \hat{X}_2 = x_{\text{sqz}} & \quad \text{squeezed amplitude quadrature} \\
 \Delta \hat{X}_1 = x_{\text{sqz}} \quad \wedge \quad \Delta \hat{X}_2 = \frac{1}{x_{\text{sqz}}} & \quad \text{squeezed phase quadrature,}
 \end{aligned} \tag{2.37}$$

where  $x_{\text{sqz}}$  is a positive integer. In Sec. 2.4.5 the squeezed states are illustrated in the frequency domain by Fig. 2.3.



### The squeeze operator

We follow the approach of the mathematical derivation in [GK05] and introduce the squeeze operator:

$$\hat{S}(\xi) = e^{\frac{1}{2}(\xi^* \hat{a}^2 - \xi \hat{a}^{\dagger 2})}, \quad (2.38)$$

where  $\xi = r e^{i\varsigma}$  is the squeeze parameter and  $r$  is the gain of the squeezing defined as  $0 \leq r < \infty$ . It is a measure of how elliptical the “compressed ball” becomes.  $0 \leq \varsigma \leq 2\pi$  is the phase angle that defines the squeezing quadrature. Examining the mechanism of the squeeze operator acting on states, the Baker-Hausdorff lemma yields [Bak02]:

$$\begin{aligned} \hat{S}^\dagger(\xi) \hat{a} \hat{S}(\xi) &= \hat{a} \cosh(r) - \hat{a}^\dagger e^{i\varsigma} \sinh(r), \\ \hat{S}^\dagger(\xi) \hat{a}^\dagger \hat{S}(\xi) &= \hat{a}^\dagger \cosh(r) - \hat{a} e^{-i\varsigma} \sinh(r). \end{aligned} \quad (2.39)$$

Since we are interested in how the squeeze operator affects the uncertainties of the quadrature operators we apply the squeeze operator to the vacuum state  $\hat{S}(\xi)|0\rangle$  and investigate the variances of the amplitude and phase quadratures:

$$\begin{aligned} \Delta^2 X_{\xi,1} &= \cosh^2(r) + \sinh^2(r) - 2 \sinh(r) \cosh(r) \cos(\varsigma) \\ &= \sin^2\left(\frac{\varsigma}{2}\right) e^{2r} + \cos^2\left(\frac{\varsigma}{2}\right) e^{-2r}, \end{aligned} \quad (2.40)$$

and

$$\begin{aligned} \Delta^2 X_{\xi,2} &= \cosh^2(r) + \sinh^2(r) + 2 \sinh(r) \cosh(r) \cos(\varsigma) \\ &= \cos^2\left(\frac{\varsigma}{2}\right) e^{2r} + \sin^2\left(\frac{\varsigma}{2}\right) e^{-2r}. \end{aligned} \quad (2.41)$$

For  $\varsigma = 0$  the amplitude quadrature is squeezed by the factor  $\exp(-2r)$  and the phase quadrature exhibits quantum noise increased by the inverse factor  $\exp(2r)$ . By steering the squeezing angle to  $\varsigma = \pi$  the situation is reversed. This is shown in Fig. 2.2.

## 2. Quantum nature of light

---

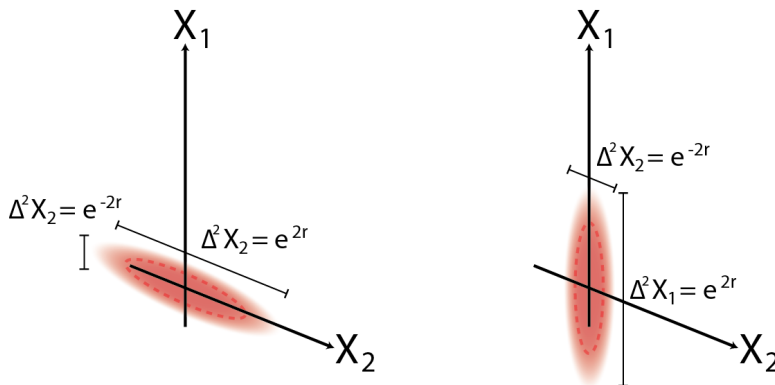


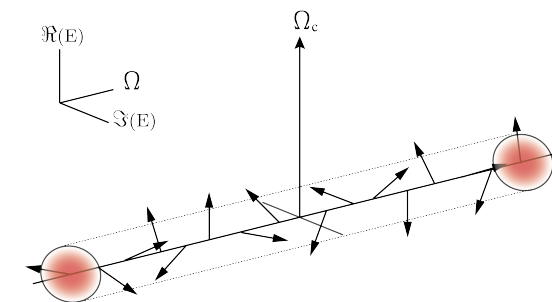
**Figure 2.2.:** Squeezed vacuum state of light. On the left the variance of the phase quadrature  $\Delta^2 X_2$  is squeezed by the factor  $\exp(-2r)$  whereas the variance of the amplitude quadrature  $\Delta^2 X_1$  exhibits quantum noise increased by the inverse factor  $\exp(2r)$ . On the right the squeezing angle is rotated by  $\zeta = \pi$ . Therefore,  $\Delta^2 X_1$  is squeezed and  $\Delta^2 X_2$  shows antisqueezing of the inverse factor  $\exp(2r)$ .

Under the assumption that no losses are introduced the squeezed states still obey the Heisenberg uncertainty principle (see Eq. (2.19)), so they are minimum uncertainty states. In an experimental realization it is impossible to produce or measure minimum uncertainty squeezed states, because due to every part of induced optical loss, the squeezed states statistics are replaced by those of the vacuum state.

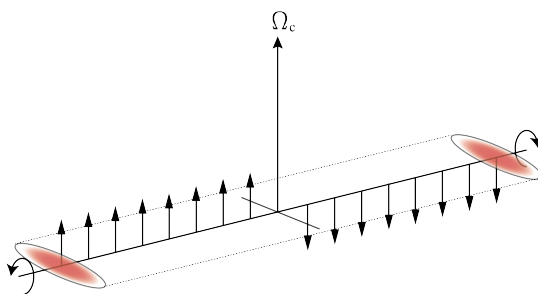
### Squeezed states of light in the sideband picture

Thus far we have introduced different theoretical concepts and descriptions of light, including quantization of the light field (see Sec. 2.2), operator nomenclature (see Sec. 2.3), linearized formalism of the quantum mechanical operators in Eq. (2.20), different states of light and phasor diagram representation (see Sec. 2.4.1). The sideband picture combines all of these descriptions into an intuitive paradigm.

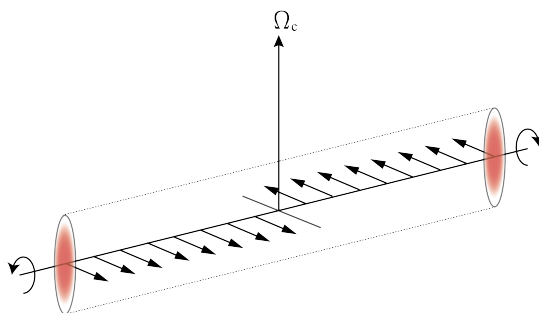
In the frequency domain the coherent (or vacuum) state is the carrier at frequency  $\Omega_c$  where its noise fluctuations are illustrated by the sidebands at all frequencies randomly orientated along the frequency axis (see Fig. 2.3a). This quantum sideband picture [Che07] is the equivalent to the ball on the phasor-arrow.



(a) Coherent state in frequency domain



(b) Amplitude-squeezed state in frequency domain



(c) Phase-squeezed state in frequency domain

**Figure 2.3.:** Squeezed states of light in the sideband picture. (a) A coherent state in the frequency domain. The noise contribution is equally distributed and uncorrelated (white noise). Since the sideband representation is in the rotating frame picture the carrier can be considered as the reference in frequency and phase. This is why there is no noise contribution on the carrier itself. (b) The amplitude-squeezed state has reduced noise in the amplitude quadrature (due to correlated phasors where the corresponding ones cause a decreasing of the noise level) and increased noise in the phase quadrature in accordance with the HUP (see Eq. (2.19)). (c) The phase-squeezed state shows the opposite behavior.

## 2. Quantum nature of light

---

Squeezing in the amplitude or phase quadrature arranges all these sidebands depending on their orientation with respect to the carrier. This means that sidebands with a higher frequency than the carrier (or a positive frequency as the carrier is the reference) are rotating clockwise whereas sidebands with a lower frequency are rotating counter-clockwise. The higher the sidebands frequency difference is with respect to the carrier the faster the rotation. Their orientation to each other depends on the type of squeezing or modulation (see Sec. 2.5); an amplitude-squeezed light field has its sidebands parallel to the carrier. The sidebands are correlated so that their noise distributions are almost not beating in the amplitude quadrature but only in the phase quadrature (see Fig. 2.3b). In contrast, the sidebands of a phase-squeezed light field are rotated by  $90^\circ$  so they are facing in the opposite direction when they are parallel to the carrier (see Fig. 2.3c). In order to detect a phase-modulated field it must be converted into amplitude modulation. By combining it with a strong local oscillator (LO) field where the carrier is rotated at  $90^\circ$  to be in the plane of sidebands of the phase modulation, a detectable beat signal is generated (see Sec. 3).

### 2.4.6. Coherent squeezed states

Beside the application of the squeeze operator to the vacuum state a more general case is considered by applying the displacement operator to a squeezed vacuum state [GK05]:

$$|\alpha, \xi\rangle = \hat{D}(\alpha)\hat{S}(\xi)|0\rangle. \quad (2.42)$$

Omitting the squeeze operator ( $\xi = 0$ ) obviously leads to a coherent state  $|\alpha\rangle = \hat{D}(\alpha)|0\rangle$ . When investigating the impact of the product of the displacement and squeeze operator on such a state and the operators  $\hat{a}$  and  $\hat{a}^\dagger$  it is necessary to identify the expectation value of the number operator  $\hat{n}$ :

$$\begin{aligned} \langle\alpha, \xi|\hat{n}|\alpha, \xi\rangle &= \langle\alpha, \xi|\hat{a}^\dagger\hat{a}|\alpha, \xi\rangle \\ &= |\alpha|^2 + \sinh^2(r). \end{aligned} \quad (2.43)$$

As a sanity check we can reduce Eq. (2.43) to the coherent state (displaced vacuum) by  $r \rightarrow 0$  or to a squeezed vacuum by  $\alpha \rightarrow 0$ . Beyond that, Eq. (2.43) shows the influence of the squeezing process since the average photon number of this state is increased by  $\sinh^2(r)$ .

The variance of the amplitude and phase quadrature operators for this state are given by:

$$\begin{aligned}\Delta^2 X_{\xi,\alpha,1} &= e^{-2r}, \\ \Delta^2 X_{\xi,\alpha,2} &= e^{2r},\end{aligned}\tag{2.44}$$

which leads to exactly the same variances as the squeezed vacuum state (see Eq. (2.40) and Eq. (2.41)), although the displaced squeezed state undergoes a coherent excitation  $\alpha$ .

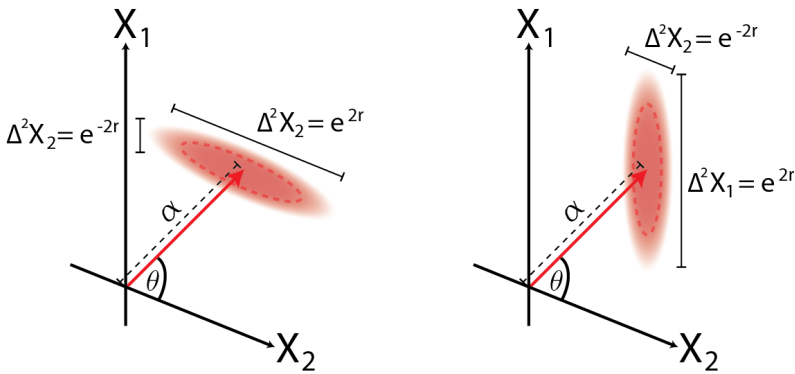


**Figure 2.4.:** Displaced squeezed vacuum state of light. The squeezed states of light in Fig. 2.2 are shifted by the displacement operator  $\hat{D}(\alpha)$ . On top of the arrow the elliptical shape of the noise distribution remains the same. On the left the variance of the phase quadrature  $\Delta^2 X_2$  is squeezed by the factor  $\exp(-2r)$ , whereas the variance of the amplitude quadrature  $\Delta^2 X_1$  exhibits increased quantum noise by the inverse factor  $\exp(2r)$ . On the right the squeezing angle is rotated by  $\varsigma = \pi$ . Therefore  $\Delta^2 X_1$  is squeezed and  $\Delta^2 X_2$  shows antisqueezing of the inverse factor  $\exp(2r)$ .

## 2.5. Modulation of light

Laser light can be described by its electric field. Considering a perfect laser this electric field is monochromatic. As modulation of light inherently implies that the electric field has multiple frequency components it can be depicted by an exemplary sine wave being phase-modulated or amplitude-modulated. The phase-modulated electric field in Fig. 2.5 has a decreased amplitude maximum and minimum, whereas the amplitude-modulated electric field in Fig. 2.6 is smaller at zero crossings [FS10].

## 2. Quantum nature of light

---

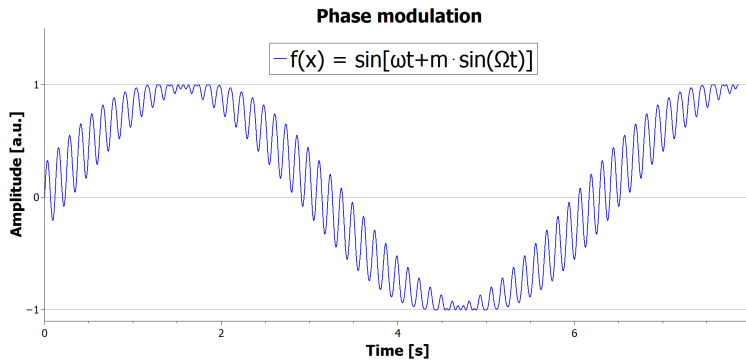


**Figure 2.5.:** Plot of the phase-modulated electric field versus time. A phase modulation corresponds to the variance of an amplitude-squeezed state, since it mostly affects the zero crossings of the sine wave and has a decreased amplitude maximum and minimum.

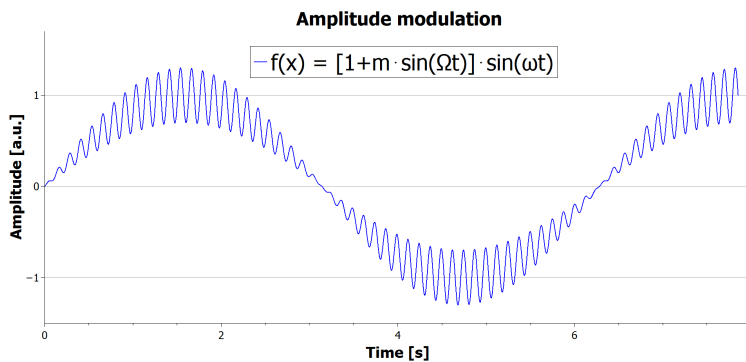


**Figure 2.6.:** Plot of the amplitude-modulated electric field versus time. An amplitude modulation corresponds to the variance of a phase-squeezed state, since it mostly affects the amplitude maximum and minimum and it has a decreased noise distribution at zero crossings.

These plots of amplitude-modulated and phase-modulated sine waves correspond to the variances of the squeezed states discussed in Sec. 2.4.5.

### 2.5.1. Phase modulation

Depending on the modulation depth the height of the generated higher-order sidebands at multiples of the modulation frequency is strongly decreased. For small modulation indices  $m$  it is usually safe to neglect higher-order sidebands. Following [FS10] and with the use

of Bessel functions a phase-modulated field can be described and approximated with the following equation:

$$\begin{aligned}
 E &= E_0 e^{i(\omega t + m \cos(\Omega t))} \\
 &= E_0 e^{i\omega t} \left( 1 - \frac{m^2}{4} + i \frac{m}{2} (e^{-i\Omega t} + e^{i\Omega t}) \right) \\
 &= \left( 1 - \frac{m^2}{4} \right) E_0 e^{i\omega t} + i \frac{E_0 m}{2} e^{i(\omega - \Omega)t} + i \frac{E_0 m}{2} e^{i(\omega + \Omega)t}.
 \end{aligned} \tag{2.45}$$

It shows that energy is shifted from the carrier to the sidebands of the modulation frequency  $\pm\Omega$  since the first factor  $\left(1 - \frac{m^2}{4}\right)$  decreases the amplitude of the carrier. The two sidebands  $i \frac{E_0 m}{2} e^{i(\omega \pm \Omega)t}$  are imaginary and hence in the phase quadrature.

### 2.5.2. Amplitude modulation

Compared to phase modulation with its modulation depth dependent comb of sidebands, amplitude modulation generates exactly two sidebands at frequencies  $\pm\Omega$ . An amplitude-modulated field can be described by the following equation:

$$\begin{aligned}
 E &= E_0 e^{i\omega t} (1 + m \cos(\Omega t)) \\
 &= E_0 e^{i\omega t} \left( 1 + \frac{m}{2} e^{-i\Omega t} + \frac{m}{2} e^{i\Omega t} \right) \\
 &= E_0 e^{i\omega t} + \frac{E_0 m}{2} e^{i(\omega - \Omega)t} + \frac{E_0 m}{2} e^{i(\omega + \Omega)t}.
 \end{aligned} \tag{2.46}$$

The two sidebands  $\frac{E_0 m}{2} e^{i(\omega \pm \Omega)t}$  are generated without reducing the amplitude of the carrier (the first term).

### 2.5.3. Modulation in the sideband picture

The sideband picture can more generally be used to understand the important concepts of amplitude and phase modulation of a carrier light field. This concept of signal modulation is very important for the experimental implementation of signal spectroscopy via cascaded phase modulation (see Chap. 8). In the frequency domain any kind of modulation generates new frequency components. These sidebands are rotating with a certain frequency with respect to the carrier. The sideband picture is useful to illustrate the different behaviors of the sidebands in the amplitude and phase quadratures with respect to the different modulations.

## 2. Quantum nature of light

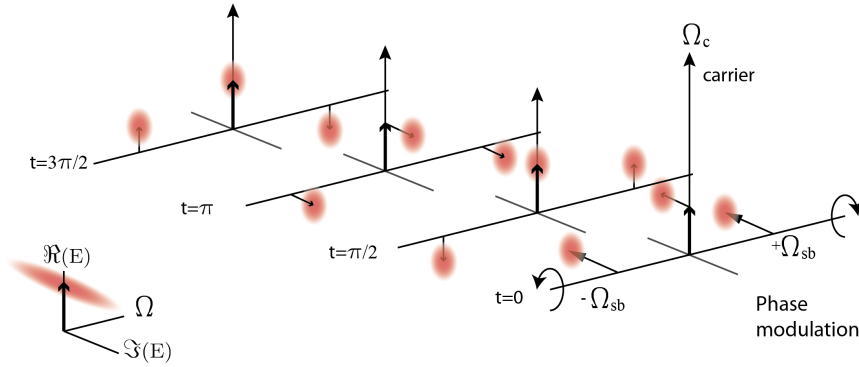


**Figure 2.7.:** Phase modulation of a coherent state in the sideband picture representation. In addition to the phasor diagrams in the frequency domain (see Fig. 2.3) the vacuum noise distributions are added on top of each phasor. The time evolution ( $t = 0, t = \pi/2, t = \pi, t = 3\pi/2$ ) of the measured quadratures of the amplitude-modulated states results in the orientation of the carrier phasor and its summated noise contribution. The obtained phase noise distribution over time is elliptical (shown on the left). In the phase quadrature ( $\Im(E) = X_2$ ) the noise distribution is increased for the benefit of a decreased noise distribution in the amplitude quadrature ( $\Re(E) = X_1$ ).



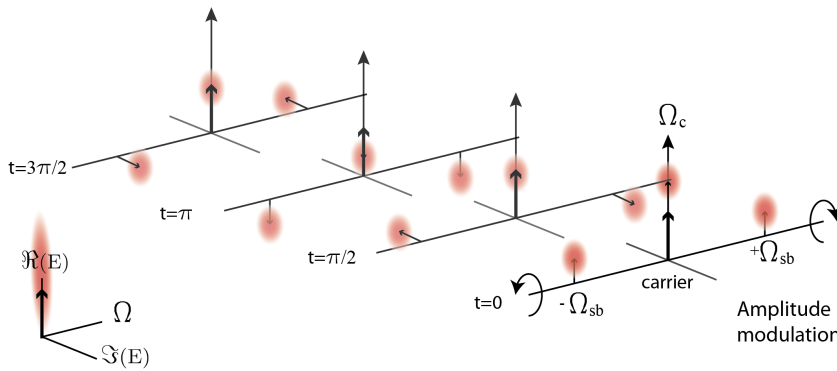


**Figure 2.8.:** Amplitude modulation of a coherent state in the sideband picture representation. In addition to the phasor diagrams in the frequency domain (see Fig. 2.3) the vacuum noise distributions are added on top of each phasor. The time evolution ( $t = 0, t = \pi/2, t = \pi, t = 3\pi/2$ ) of the measured quadratures of the amplitude-modulated states results in the orientation of the carrier phasor and its summated noise contribution. The obtained amplitude noise distribution over time is elliptical (shown on the left). In the amplitude quadrature ( $\Re(E) = X_1$ ) the noise distribution is increased for the benefit of a decreased noise distribution in the phase quadrature ( $\Im(E) = X_2$ ).



## 3

## Chapter 3

## Detection of light

The measurements presented in this work are taken via photodetection of optical fields, which can be expressed as observables  $\hat{X}_1$  and  $\hat{X}_2$ . When illuminated a photodetector produces a photocurrent proportional to the intensity of the light field, and therefore to the number of incident photons per unit time.

This chapter discusses the interaction of the light field with a photosensitive measurement device and provides an overview of different detection techniques of light fields.

### Methods of detecting light and quantum noise

Since laser light can be used as a precise “ruler” for the measurement of small differential length changes (for example those caused by gravitational waves), it is important to detect this light field with all its information about phase and amplitude as precisely as possible. This section outlines how light can be detected and how different detection schemes can yield information on its physical properties. Subsequently, different forms of photodetection are introduced. The initial concept of a single photodetector is first considered and extended to a balanced detection scheme. This leads to the polarization-based homodyne detection scheme which plays a crucial role in obtaining the experimental results presented in this work. The central issue of optical loss which couples as zero point field fluctuations in the signal noise variance is discussed following the approach of [BR04].

### 3. Detection of light

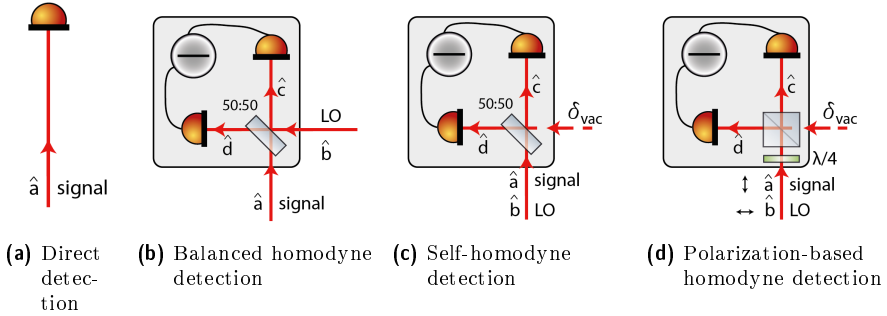


Figure 3.1.: Overview of different schemes for light detection.

#### 3.1. Direct detection with a single photodetector

A simple photodetector produces a photocurrent that is proportional to the power of the light field impinging on the photosensitive area [FS10], specified by the number of photons in the light field per unit time and the photon energy  $\hbar\omega$ . The direct detection of a laser beam with a single photodetector (see Fig. 3.1a) generates a photocurrent which is proportional to the number of absorbed photons, and also proportional to the number operator (see Eq. (2.23)):

$$\begin{aligned} i(t) &\propto \hat{a}^\dagger(t)\hat{a}(t) \\ &= \hat{n}(t). \end{aligned} \quad (3.1)$$

Omitting the time dependence and applying the previously introduced linearization approximation (see Sec. 2.3.2) on the number operator  $\hat{n}$ , Eq. (3.1) yields the fluctuating component of the light field; the detectable quantum noise in the amplitude quadrature  $\hat{X}_1$  appears as a correcting term with zero mean

$$i(t) \sim \alpha^2 + \alpha\delta\hat{X}_1(t). \quad (3.2)$$

The first term of this result describes the direct current (DC) part which is proportional to the intensity of the detected light field. This DC part is measurable with a power meter or any DC-coupled photodetector by the detection of the average photocurrent [BR04]. The second term which describes the alternating current (AC) part is represented by the fluctuating amplitude quadrature operator  $\delta\hat{X}_1$  scaled by the mean field amplitude  $\alpha$ , comparable to Eq. (2.23) [BR04]. Measuring the AC term of the photocurrent with a spectrum analyzer to

obtain a power spectrum corresponds to a Fourier transformation of the variance of the amplitude operator:

$$\begin{aligned} V_i(\omega) &\propto \alpha^2 \left\langle \left( \delta \hat{X}_1(\omega) \right) \right\rangle \\ &\propto \alpha^2 V_1(\omega). \end{aligned} \tag{3.3}$$

Since a direct detection of the light field with a single photodetector exclusively measures the variance of the amplitude quadrature  $V_1(\omega)$  scaled by the mean field amplitude  $\alpha$  no phase information can be obtained.

According to Eq. (2.37) either of the quadratures of a squeezed state can be less than the minimum fluctuation uncertainty. As we are interested in detecting such a squeezed state, the measurement of both phase and amplitude quadrature variance with a spectrum analyzer plays an important role in the investigation of the variance of an optical parametric oscillator (OPO) in terms of squeezing, described in this thesis.

## 3.2. Balanced homodyne detection

One method to gain phase information is a detection scheme with two photodiodes which is called *balanced homodyne detection*. For a phase-sensitive measurement of the signal field  $\hat{a}$  an additional LO field  $\hat{b}$  at the same laser frequency  $\omega$  is introduced as a phase reference. Additionally the local oscillator amplitude amplifies the fluctuations of the signal field we are interested in. Since there are different kinds of homodyne detection schemes (see Fig. 3.1) we will discuss balanced homodyne detection and two cases of self-homodyne detection separately. In the balanced homodyne detection scheme shown in Fig. 3.1b, the signal field  $\hat{a}$  and the LO field  $\hat{b}$  are split equally on a 50/50 power beamsplitter, leading to the amplitude coefficients for transmission  $t = 1/\sqrt{2}$  and reflection  $r = 1/\sqrt{2}$ , respectively. The resulting outputs  $\hat{c}$  and  $\hat{d}$  are detected with two separate photodiodes and their photocurrents are subtracted to obtain the phase sensitive differential signal. Using the matrix formalism and choosing the asymmetric beamsplitter convention [BR04] the fields can be calculated as

$$\begin{aligned} \begin{pmatrix} \hat{c} \\ \hat{d} \end{pmatrix} &= \begin{pmatrix} t & r \\ -r & t \end{pmatrix} \begin{pmatrix} \hat{a} \\ \hat{b} \end{pmatrix} \\ &= \frac{1}{\sqrt{2}} \begin{pmatrix} 1 & 1 \\ -1 & 1 \end{pmatrix} \begin{pmatrix} \hat{a} \\ \hat{b} \end{pmatrix}, \end{aligned} \tag{3.4}$$

### 3. Detection of light

---

which leads to the equations for the fields impinging on the two photodiodes

$$\begin{aligned}\hat{c} &= \frac{1}{\sqrt{2}} (\hat{a} + \hat{b}), & \hat{c}^\dagger &= \frac{1}{\sqrt{2}} (\hat{a}^\dagger + \hat{b}^\dagger), \\ \hat{d} &= \frac{1}{\sqrt{2}} (-\hat{a} + \hat{b}), & \hat{d}^\dagger &= \frac{1}{\sqrt{2}} (-\hat{a}^\dagger + \hat{b}^\dagger).\end{aligned}\quad (3.5)$$

Without loss of generality, the signal of interest is assumed to be real and can be represented by

$$\hat{a} = \alpha_{\text{sig}} + \delta\hat{a}, \quad (3.6)$$

and the LO superimposed on the signal field can be described as

$$\hat{b} = [\beta_{\text{LO}} + \delta\hat{b}] e^{-i\theta}, \quad (3.7)$$

where  $e^{i\theta}$  is the relative phase difference between the signal field and the LO field [BR04]. After combining the signal and the LO on the beamsplitter (as shown in Fig. 3.1b) the signals at the two photodiodes are composed of the following terms of field operators:

$$\begin{aligned}\hat{i}_1 \propto \hat{c}^\dagger \hat{c} &= \frac{1}{2} (\hat{a}^\dagger + \hat{b}^\dagger) (\hat{a} + \hat{b}), \\ \hat{i}_2 \propto \hat{d}^\dagger \hat{d} &= \frac{1}{2} (-\hat{a}^\dagger + \hat{b}^\dagger) (-\hat{a} + \hat{b}).\end{aligned}\quad (3.8)$$

Therefore the photocurrent on each photodiode can be expressed as:

$$\begin{aligned}\hat{i}_1 &= \frac{1}{2} [|\alpha_{\text{sig}}(t)|^2 + |\beta_{\text{LO}}(t)|^2 + 2\alpha_{\text{sig}}\beta_{\text{LO}} \cos(\theta) \\ &\quad + \alpha_{\text{sig}} (\delta\hat{a} + \delta\hat{a}^\dagger + \delta\hat{b}e^{-i\theta} + \delta\hat{b}^\dagger e^{i\theta}) \\ &\quad + \beta_{\text{LO}} (\delta\hat{b} + \delta\hat{b}^\dagger + \delta\hat{a}e^{i\theta} + \delta\hat{a}^\dagger e^{-i\theta}) + \mathcal{O}(\delta^2)],\end{aligned}\quad (3.9)$$

and accordingly for the second photodiode. By merging the field operators into new quadrature operators such that

$$\begin{aligned}\delta\hat{X}_o^+ &= \delta\hat{o} + \delta\hat{o}^\dagger, \\ \delta\hat{X}_o^- &= i(\delta\hat{o} - \delta\hat{o}^\dagger),\end{aligned}\quad (3.10)$$

and

$$\delta\hat{X}_o^{\mp\theta} = \delta\hat{o}e^{\pm i\theta} + \delta\hat{o}^\dagger e^{\mp i\theta}, \quad (3.11)$$

for an arbitrary operator ( $\hat{o}$ ), Eq. (3.9) becomes clearer. The photodiode currents are

$$\begin{aligned}\hat{i}_1 &= \frac{1}{2} [|\alpha_{\text{sig}}(t)|^2 + |\beta_{\text{LO}}(t)|^2 + 2\alpha_{\text{sig}}\beta_{\text{LO}} \cos(\theta) \\ &\quad + \alpha_{\text{sig}} (\delta\hat{X}_{\text{sig}}^+ + \delta\hat{X}_{\text{LO}}^\theta) + \beta_{\text{LO}} (\delta\hat{X}_{\text{LO}}^+ + \delta\hat{X}_{\text{sig}}^{-\theta})], \\ \hat{i}_2 &= \frac{1}{2} [|\alpha_{\text{sig}}(t)|^2 + |\beta_{\text{LO}}(t)|^2 - 2\alpha_{\text{sig}}\beta_{\text{LO}} \cos(\theta) \\ &\quad + \alpha_{\text{sig}} (\delta\hat{X}_{\text{sig}}^+ - \delta\hat{X}_{\text{LO}}^\theta) + \beta_{\text{LO}} (\delta\hat{X}_{\text{LO}}^+ - \delta\hat{X}_{\text{sig}}^{-\theta})].\end{aligned}\quad (3.12)$$

By subtracting the photodiode currents the steady-state amplitudes cancel each other out, leaving the differential current

$$\hat{i}_- \propto \hat{i}_1 - \hat{i}_2 = 2\alpha_{\text{sig}}\beta_{\text{LO}} \cos(\theta) + \alpha_{\text{sig}}\delta\hat{X}_{\text{LO}}^\theta + \beta_{\text{LO}}\delta\hat{X}_{\text{sig}}^{-\theta}. \quad (3.13)$$

Under the assumption that the LO field has a much higher intensity than the signal field ( $\alpha_{\text{sig}} \ll \beta_{\text{LO}}$ ) the middle term of the right hand side of Eq. (3.13) can be neglected. This assumption is also known as the *homodyne condition*, and

$$\hat{i}_- = 2\alpha_{\text{sig}}\beta_{\text{LO}} \cos(\theta) + \beta_{\text{LO}}\delta\hat{X}_{\text{sig}}^{-\theta} \quad (3.14)$$

leads to the variance of the measured differential current:

$$V_{\hat{i}_-} = \beta_{\text{LO}}^2 V(\delta\hat{X}_{\text{sig}}^{-\theta}). \quad (3.15)$$

It contains only the fluctuations of the signal field  $\delta\hat{X}_{\text{sig}}^{-\theta}$  scaled by the LO amplitude  $\beta_{\text{LO}}^2$ . Due to common mode rejection the fluctuations from the LO are canceled out, as long as  $\alpha_{\text{sig}} \ll \beta_{\text{LO}}$  [YC83].

It is important to consider the influence of the relative phase difference  $\theta$  between the signal field and the LO field for the desired quadrature in the detection scheme. A phase difference of  $\theta = 90^\circ$  enables the measurement of the phase quadrature. Accordingly, if the signal and LO field are in phase ( $\theta = 0^\circ$ ), an amplitude quadrature measurement is possible. This result shows how the fluctuations and modulations described by the quadrature operators can be detected, by amplifying them with the large amplitude of the mean value of the LO, without its fluctuations corrupting the measurement.

### 3.3. Self-homodyne detection

The significant feature of the self-homodyne detection scheme is that the signal field and LO field are spatially perfectly overlapped and

### 3. Detection of light

---

form the incoming field  $\hat{a} = \alpha_{\text{sig}} + \delta\hat{a} + \beta_{\text{LO}} + \delta\hat{b}$ . This field is split up on the power beamsplitter and both light fields are detected on photodiodes (see Fig. 3.1c). Having the LO coexist in the signal field enhances the fluctuating quadrature operator of the signal field by its mean field amplitude. However, there is no external phase reference, since the vacuum field  $\hat{v} = 0 + \delta\hat{v}_{\text{vac}}$ , which is coupled in by the beamsplitter, has no defined phase. This is why self-homodyne detection with the signal and LO exclusively allows measurements of the amplitude quadrature  $\hat{X}^+$ , amplified by the local oscillators amplitude. According to Eq. (3.8) the current for each photodiode is

$$\begin{aligned} \hat{i}_1 &= \frac{1}{2} \left( (\alpha_{\text{sig}} + \beta_{\text{LO}})^2 + (\alpha_{\text{sig}} + \beta_{\text{LO}}) \left( \delta\hat{X}_{\text{sig}}^+ + \delta\hat{X}_{\text{LO}}^+ + \delta\hat{X}_{\text{vac}}^+ \right) \right), \\ \hat{i}_2 &= \frac{1}{2} \left( (\alpha_{\text{sig}} + \beta_{\text{LO}})^2 + (\alpha_{\text{sig}} + \beta_{\text{LO}}) \left( \delta\hat{X}_{\text{sig}}^+ + \delta\hat{X}_{\text{LO}}^+ - \delta\hat{X}_{\text{vac}}^+ \right) \right). \end{aligned} \quad (3.16)$$

Deriving the sum and the difference of the photocurrents by considering the *homodyne condition* introduced in Sec. 3.2 leads to

$$\begin{aligned} \hat{i}_+ &\propto (\alpha_{\text{sig}} + \beta_{\text{LO}})^2 + (\alpha_{\text{sig}} + \beta_{\text{LO}}) \delta\hat{X}_{\text{sig}}^+, \\ \hat{i}_- &\propto (\alpha_{\text{sig}} + \beta_{\text{LO}}) \delta\hat{X}_{\text{vac}}^+. \end{aligned} \quad (3.17)$$

The difference of the photocurrents results in the shot noise level  $V_{\text{vac}}^+$ , whereas the sum of the photocurrents is a measurement of the amplitude quadrature fluctuation of the light field  $V_{\text{sig}}^+$  with high precision.

### 3.4. Polarization-based homodyne detection

In the polarization-based homodyne detection scheme the signal and LO copropagate in two perpendicular polarizations of the same light field. We consider the case where the signal field is vertically linearly polarized  $|V\rangle$  (in s-polarization) and the LO is horizontally linearly polarized  $|H\rangle$  (in p-polarization).

#### Polarization of light

Considering the propagation of light as an electromagnetic wave along the optical axis one property is its helicity [Jac99]. There are two possible orthogonal quantum states: right circular polarization  $|R\rangle$  and left circular polarization  $|L\rangle$ . In most of the experimental setups described in this work the light was linearly



### 3.5. The influence of optical losses and detection efficiencies

polarized; either in vertical polarization  $|V\rangle = (|R\rangle + |L\rangle) \sqrt{2}$ , in horizontal polarization  $|H\rangle = (|R\rangle - |L\rangle) \sqrt{2}$ , or in a linear combination of both polarizations called “diagonal” polarization.

In contrast to balanced homodyne detection, where the signal of interest and the LO have the same polarization when they meet on the power beamsplitter, polarization-based homodyne detection requires a combination of a quarter-waveplate (QWP) and a polarizing beamsplitter (PBS) to generate the superimposed signal, due to the fact that orthogonal polarizations do not interfere. Eq. (3.4) is then modified via the Jones-formalism [Jon47] to:

$$\begin{pmatrix} \hat{c} \\ \hat{d} \end{pmatrix} = \frac{1}{\sqrt{2}} \begin{pmatrix} e^{i\pi/4} & 0 \\ 0 & e^{-i\pi/4} \end{pmatrix} \frac{1}{\sqrt{2}} \begin{pmatrix} 1 & 1 \\ -1 & 1 \end{pmatrix} \begin{pmatrix} |H\rangle \\ |V\rangle \end{pmatrix}, \quad (3.18)$$

where  $|H\rangle$  is the polarization of the LO and  $|V\rangle$  is the polarization of the signal field. As we can see, this QWP creates mixed states with equal parts of  $|H\rangle$  and  $|V\rangle$  with a relative phase shift of  $\theta = \pi/2 = 90^\circ$ . By performing polarization spectroscopy (for example to stabilize a cavity, see Sec. 6.1.4) the signal field in s-polarization gets an additional phase shift  $\Delta\phi$  with respect to the LO in p-polarization leading to:

$$\begin{aligned} |H\rangle &= \beta_{\text{LO}} + \delta\hat{b}, \\ |V\rangle &= \alpha_{\text{sig}} + \delta\hat{a}e^{i\Delta\phi}, \end{aligned} \quad (3.19)$$

where  $\Delta\phi$  is the additional phase of the cavity picked up by the resonant s-polarized signal field  $|V\rangle$ . The fixed phase difference of  $\theta = \pi/2 = 90^\circ$  leads to the confinement of detecting the phase quadrature of the signal field fluctuations  $\delta X_{\text{sig}}^-$  which modifies Eq. (3.14) to:

$$\begin{aligned} \hat{i}_- \propto i_1 - i_2 &= 2\alpha_{\text{sig}}\beta_{\text{LO}} \cos\left(\frac{\pi}{2} + \Delta\phi\right) + \alpha_{\text{sig}}\delta X_{\text{LO}}^+ + \beta_{\text{LO}}\delta X_{\text{sig}}^-, \\ \hat{i}_- &= -2\alpha_{\text{sig}}\beta_{\text{LO}} \sin(\Delta\phi) + \beta_{\text{LO}}\delta X_{\text{sig}}^-. \end{aligned} \quad (3.20)$$

This particular form of homodyne detection is used in almost every part of the experimental setup described in this work. Its implementation is discussed in detail in Sec. 6.1.4.

### 3.5. The influence of optical losses and detection efficiencies

Ideally, a photodiode converts every incident photon into an electron so that the generated photocurrent is directly proportional to the in-

### 3. Detection of light

---

tensity of the light field. The fraction of converted photons is called the *quantum efficiency*  $\eta_{qe}$  of a photodiode and is at best  $\eta_{qe} = 1$ . However, the conversion from a photon to an electron by the photodiode experiences losses  $\epsilon$  such as absorption and scattering [BR04]. Therefore, a photodiode has a quantum efficiency smaller than unity.

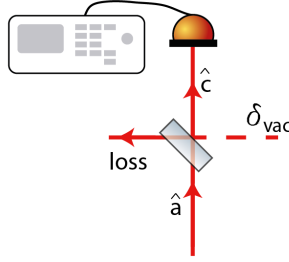


**Figure 3.2.:** Schematic illustrating the detection of a light field with a beamsplitter where losses are introduced. The beamsplitter has a power reflectivity  $\epsilon$  and transmittance  $\eta$ . A direct detection with including losses can be considered with the detection efficiency  $\eta = 1 - \epsilon$ .

A mathematical consideration of introducing losses can be represented by a partially transmissive beamsplitter with transmittance  $\eta = 1 - \epsilon$  (see Fig. 3.2). Since there is no light field entering the unused port, vacuum fluctuations  $\delta_{vac} = \delta\hat{\nu}$  couple into the light field of interest  $\hat{c}$  as follows

$$\hat{c} = \sqrt{\eta}\hat{a} + \sqrt{1 - \eta}\delta\hat{\nu}. \quad (3.21)$$

This leads to the following photocurrent at the detector:

$$\hat{i} \approx \hat{c}^\dagger \hat{c} = \eta\alpha^2 + \sqrt{\eta}\alpha \left( \sqrt{\eta}\delta\hat{X}_a^+ + \sqrt{1 - \eta}\delta\hat{X}_\nu^+ \right), \quad (3.22)$$

where the mean value of the field is scaled by the transmittance of the beamsplitter  $\eta$ , which is the equivalent to the detection efficiency and the fluctuating term in the amplitude quadrature. Calculating the variance yields

$$V_i = \eta\alpha^2 [\eta V_a^+ + (1 - \eta)], \quad (3.23)$$

which is comparable to the variance of a balanced homodyne detector reconsidered with the same loss model. Since the spectrum analyzer

### 3.5. The influence of optical losses and detection efficiencies

normally measures the variance  $V_{\text{dB}}$  in dB, the conversion to the linear variance  $V_{\text{lin}} = 10(V_{\text{dB}}/10)$ , taking the detection efficiency  $\eta$  into account, is:

$$V_{\eta,\text{dB}} = 10\log_{10} \left[ \eta 10^{\frac{V_{\text{dB}}}{10}} + (1 - \eta) \right]. \quad (3.24)$$

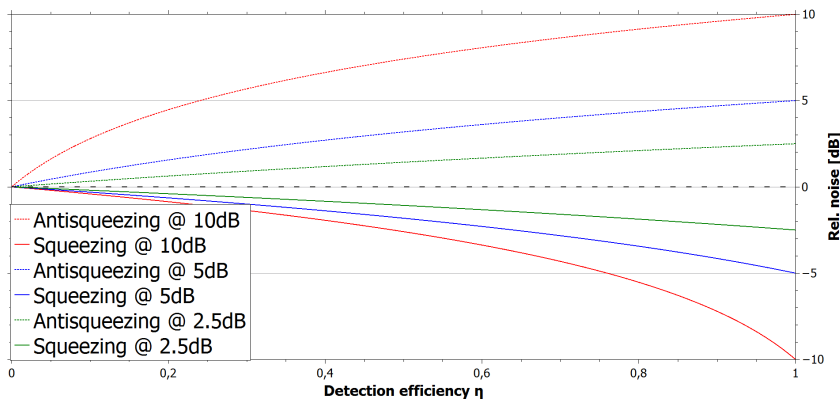


**Figure 3.3.:** Resulting noise variances of the light field as a function of the detection efficiency for different input variances. The shot noise (black dashed line) is the reference line at 0 dB. If the input variances experience more losses the detection efficiency is decreased and the resulting variances converge to the shot noise. The squeezed variance converges faster than the antisqueezed variance because it is more susceptible to losses.

The dependence of the resulting variance on losses affecting the input variance is depicted in Fig. 3.3. If the input variances experience more losses the detection efficiency is decreased and the resulting variances converge to the shot noise. The squeezed variance converges faster because it is more susceptible to losses [BR04]. If the relative noise of the variance is larger it decreases faster with the losses introduced. This shows the fragile nature of squeezed states and explains the effort to minimize incoupling losses in such a measurement setup. The vacuum state cannot be affected by losses since there is no change in its variance by adding vacuum noise.

#### 3.5.1. Homodyne mode mismatch

The essential part of balanced homodyne detection is the superimposing of the signal field and the LO field. A mismatch is equivalent to introduced losses, therefore the experimental realization of the best

### 3. Detection of light

---

possible interference is crucial due to many error sources such as spatial mode mismatch or polarization mismatch. The fringe visibility VIS can be used to describe the quality of the interference. It can be determined by the maximum intensity  $I_{\max}$  and minimum intensity  $I_{\min}$  of the interference fringe, by scanning the relative phase between signal field and LO field [L<sup>+</sup>98], by

$$\text{VIS} = \frac{I_{\max} - I_{\min}}{I_{\max} + I_{\min}}. \quad (3.25)$$

Calculating the effect of mode mismatch in a homodyne measurement with the linearization of the operators leads to the same loss calculation on a beamsplitter as already seen in Sec. 3.5. The square of the visibility results in the efficiency factor  $\eta_h$ :

$$\text{VIS}^2 = \eta_h. \quad (3.26)$$

The best possible mode matching is especially important to measure squeezed states since they are very susceptible to losses (see Fig. 3.3), meaning every loss introduces more vacuum fluctuations into the squeezed state and thereby reduces the degree of squeezing.

# 4

## Chapter 4

# Fundamentals of optical resonators

A typical interferometer layout for current GWDs consists of a beamsplitter that divides the incident laser beam into two perpendicular interferometer arms where the light field can interact with passing gravitational waves before it is recombined at the beamsplitter. By using resonators in these arms the effective interaction time between the light field and the gravitational wave is enhanced such that the length changes can be observed with increased sensitivity.

This chapter builds the theoretical background for an understanding of the principles of optical resonators (often called optical cavities). The experimental setups described in this work consist of several resonator types. The first section contains general considerations of the light field interacting with a linear Fabry-Pérot cavity, derived following the approach of [FS10]. For squeezed-state generation (see Chap. 6 and Chap. 7) – the main part of this work – a bow-tie cavity design was used. For this reason the cavity dynamics derived in the second part are adapted to the experimental setup. Subsequently, the equations of motion for a cavity are introduced and extended by the input-output formalism to describe how the intracavity dynamics affect the output of the cavity [WM07].

## 4.1. The two-mirror resonator: a linear Fabry-Pérot cavity

In general, optical cavities are a system of mirrors between which a closed path for light propagation exists. In the most simple case

## 4. Fundamentals of optical resonators

---

they consist of two opposing (flat or spherical) mirrors separated by a distance  $L$  (see Fig. 4.1). If the resonator's optical path length is an integer multiple of half wavelengths ( $n\lambda = 2L$ ) the light confined within interferes constructively.

### 4.1.1. Light field amplitudes

Derived from Eq. (2.5) and described further in Sec. 3 the interaction of light fields and optical devices is mathematically described by a beamsplitter (see Fig. 3.2). Similarly a mirror can be described with input and output ports with amplitude coefficients for reflection ( $r_j$ ) and transmission ( $t_j$ ) [FS10].

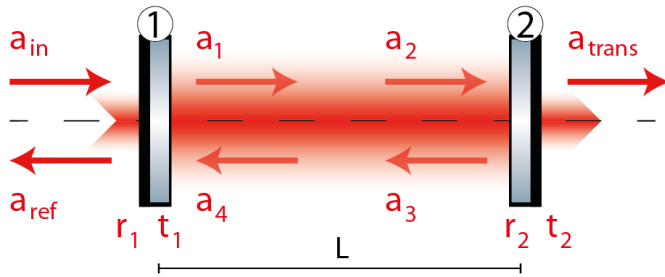


**Figure 4.1.:** Schematic of light field amplitudes interacting with a cavity consisting of two mirrors. Both mirrors are characterized by their amplitude coefficients for reflection ( $r_j$ ) and transmission ( $t_j$ ).

### Light on a mirror: Reflection, transmission and propagation

For the interaction of the light field with the FP cavity two processes must be considered: propagation through a medium (vacuum, air, mirror) and interaction with an optical surface (reflection or transmission) with a different index of refraction  $n$ .

The real amplitude coefficients for reflection  $r$  and transmittance  $t$  are related to the losses  $L$ , power reflectivity  $R$  and transmittance  $T$  via  $T + R + L = t^2 + r^2 + L = 1$ . If the light field  $a_{in}$  couples in at mirror 1 (see Fig. 4.1) the field amplitudes can be expressed as

$$\begin{aligned} a_1 &= r a_4 + i t a_{in}, \\ a_{ref} &= r a_{in} + i t a_4. \end{aligned} \quad (4.1)$$

## 4.1. The two-mirror resonator: a linear Fabry-Pérot cavity

The phase shift for the transition of the light field through mirror 1 into the cavity is given by the factor  $i$ . This differs from the phase shift of  $\pi/2$  used in the beamsplitter description of Eq. (3.4) for the two light fields in the homodyne detection scheme <sup>1</sup>.

If we restrict our analysis to the on-axis field and neglecting the gain of the Gouy phase we consider the light field as a plane wave (see Eq. (2.6)) along the optical axis of the distance  $L$  through a medium with the index of refraction  $n$ , which leads to

$$\begin{aligned} a_2 &= a_1 e^{-iknL}, \\ a_4 &= a_3 e^{-iknL}, \end{aligned} \quad (4.2)$$

A complete set of equations arises by combining the interactions of the light field with the two mirrors and its free propagation between them in vacuum ( $n = 1$ ):

$$\begin{aligned} a_1 &= it_1 a_{\text{in}} + r_1 a_4, \\ a_2 &= e^{-ikL} a_1, \\ a_{\text{trans}} &= it_2 a_2, \\ a_3 &= r_2 a_2, \\ a_4 &= e^{-ikL} a_3, \\ a_{\text{ref}} &= r_1 a_{\text{in}} + it_1 a_4. \end{aligned} \quad (4.3)$$

By successively inserting the separate equations into each other one can describe the reflected, transmitted and intracavity field as a function of the input field and the mirror parameters. This leads to the equation for the field after one cavity round trip:

$$a_4 = a_{\text{in}} \frac{ir_2 t_1 e^{-i2kL}}{1 - r_1 r_2 e^{-i2kL}}. \quad (4.4)$$

The reflected field is

$$a_{\text{ref}} = a_{\text{in}} \frac{r_1 - r_2 (r_1^2 + t_1^2) e^{-i2kL}}{1 - r_1 r_2 e^{-i2kL}}, \quad (4.5)$$

<sup>1</sup>There are two indices of refraction  $n_1$  and  $n_2$  involved in the reflection and transmission of light at the boundary between the optical media. Using Fresnel's equations [Ken08] one can derive phase relations between the individual coefficients in order to satisfy the energy conservation. One possible convention for a symmetric choice is to let each transmitted field ( $a_{\text{in}}$ ,  $a_4$ ) pick up a phase shift of  $\pi/2$  while the reflected fields remain at zero.

## 4. Fundamentals of optical resonators

---

and the transmitted field is:

$$a_{\text{trans}} = a_{\text{in}} \frac{-t_1 t_2 e^{-ikL}}{1 - r_1 r_2 e^{-i2kL}}. \quad (4.6)$$

For investigations into the polarization-dependent differences in the reflected fields the power reflectivities of the mirrors for s- and p-polarization (representative for mirror curvature or penetration depth) are taken into account, see Sec. 8.2.2.

### Coupling matrices

Instead of describing the interaction of the light field sequentially, coupling matrices offer a more compact system description. For various calculations of complex resonator schemes coupling matrices are very useful. Every single optical element of the system can be described by a matrix and therefore, the complete resonator can be described by the product of these matrices which can be successively multiplied,

$$M_{\text{cav}} = M_{\text{mirror}} \cdot M_{\text{inside}} \cdot M_{\text{mirror}}. \quad (4.7)$$

The two-mirror resonator from Eqs. (4.3) in matrix formalism leads to

$$\begin{pmatrix} a_{\text{in}} \\ a_{\text{ref}} \end{pmatrix} = \frac{-1}{t_1 t_2} \begin{pmatrix} e^{ikL} - r_1 r_2 e^{-ikL} & -r_2 e^{ikL} + r_1 e^{-ikL} \\ -r_2 e^{-ikL} + r_1 e^{ikL} & e^{-ikL} - r_1 r_2 e^{ikL} \end{pmatrix} \begin{pmatrix} a_{\text{trans}} \\ 0 \end{pmatrix} \quad (4.8)$$

This formalism extends effortlessly to more complex or coupled cavity mirror arrangements.

#### 4.1.2. Properties and characteristics of a linear Fabry-Pérot cavity

To investigate the behavior of a FP cavity some properties need to be calculated from the cavity parameters (namely the optical path length of the cavity  $L$ , the wavelength of the incoming light field  $\lambda$  and the parameters of the two mirrors: reflectivity  $r$  and transmittance  $t$ ). The transmittance of the cavity is given by its transfer function relating the input field  $a_{\text{in}}$  to the transmitted field  $a_{\text{trans}}$ ,

$$\frac{a_{\text{trans}}}{a_{\text{in}}} = \frac{-t_1 t_2 e^{-ikL}}{1 - r_1 r_2 e^{-i2kL}}. \quad (4.9)$$

Since the wave vector  $k = 2\pi f/c$  is frequency dependent Eq. (4.9) has its maximum for a certain frequency at cavity resonance  $kL =$



## 4.1. The two-mirror resonator: a linear Fabry-Pérot cavity

---

$2\pi f_c L/c = N\pi$ , where  $N$  is an integer. The spacing between two adjacent fundamental frequencies  $f_c = Nc/2L$  is the *free spectral range* (FSR) which for a linear cavity is defined as

$$\text{FSR} = \frac{c}{2L}. \quad (4.10)$$

The *linewidth*  $\Delta\nu$  of the cavity is a measure of the average lifetime of the photons  $\tau$  in the cavity and is determined by the reflectivities of the mirrors  $R_i = r_i^2$ . The higher the reflectivities the longer the lifetime of the photons in the cavity and the smaller the cavity decay rate. The *cavity decay rate*  $\kappa$  is defined by

$$2\kappa = -c/L \cdot \ln[R_1 \cdot R_2 \cdot (1 - l)]$$

(cf. [SH98]), where  $l$  is the intracavity loss,  $L$  the cavity length and  $c$  the speed of light. This link between the cavity decay rate and the linewidth can be expressed as

$$\kappa = \pi\Delta\nu. \quad (4.11)$$

The ratio of the FSR to the linewidth indicates the quality of the cavity as a function of its mirror reflectivities. This quality factor which is called the *finesse*  $\mathcal{F}$  is

$$\mathcal{F} = \frac{\text{FSR}}{\Delta\nu}. \quad (4.12)$$

It can be approximated as

$$\mathcal{F} = \frac{\pi\sqrt{r_1 r_2}}{1 - r_1 r_2} \quad (4.13)$$

for high reflectivities ( $r_j > 0.7$ ). In high-finesse cavities the intracavity field is enhanced significantly due to the small decay rate. As an example, a high intensity of the light field is useful to increase the efficiency of nonlinear interactions inside the cavity (see Sec. 5.1).

The linewidth of the cavity defines the bandwidth of the generated squeezed light which is described in Chap. 6. Furthermore it defines the characteristics of the cavity for transmittance and reflection leading which must be considered for various locking loops (see Sec. 6.1).

## 4. Fundamentals of optical resonators

---

### Cavity impedance matching

The transmitted and directly reflected fields of the FP cavity vary as a function of the mirrors' reflectivity. This leads to three possible scenarios [FS10]:

- Undercoupled cavity:  $T_1 < T_2$   
The amplitude of the directly reflected field is larger than that of the leaking cavity field. Since the incoming and reflected field are in phase there is constructive interference.
- Overcoupled cavity:  $T_1 > T_2$   
The amplitude of the directly reflected field is much weaker than that of the leaking cavity field. This is why the phase between the incoming and reflected fields is  $\pi$ .
- Impedance matched cavity:  $T_1 = T_2$   
The reflected field vanishes due to destructive interference of the directly reflected field and the outcoupled field on mirror 1.

The impedance matching conditions (and their resulting phases, see [FS10]) are important for considerations of frequency stabilization schemes where phase-sensitive measurements are needed for generating an error signal (see Sec. 6.3.3).

### Stability criteria

For the fully Gaussian beam (see Sec. 2.1) in the two-mirror resonator not all combinations of the mirror's radii of curvature (ROC) and distance  $L$  between the mirrors lead to a stable retroreflection. The stability condition relates the resonator geometry to how efficient the light field is reproduced periodically. This condition can be obtained by ray transfer matrix analysis [KL66]:

$$0 \leq \underbrace{\left(1 - \frac{L}{\text{ROC}_1}\right)}_{g_1} \underbrace{\left(1 - \frac{L}{\text{ROC}_2}\right)}_{g_2} \leq 1. \quad (4.14)$$

There are only certain value ranges for  $\text{ROC}_1$ ,  $\text{ROC}_2$ , and  $L$  that produce stable resonators. The stability criterion from Eq. (4.14) is shown graphically with the stability parameter  $g_j$  for each mirror in Fig. 4.2.

## 4.1. The two-mirror resonator: a linear Fabry-Pérot cavity

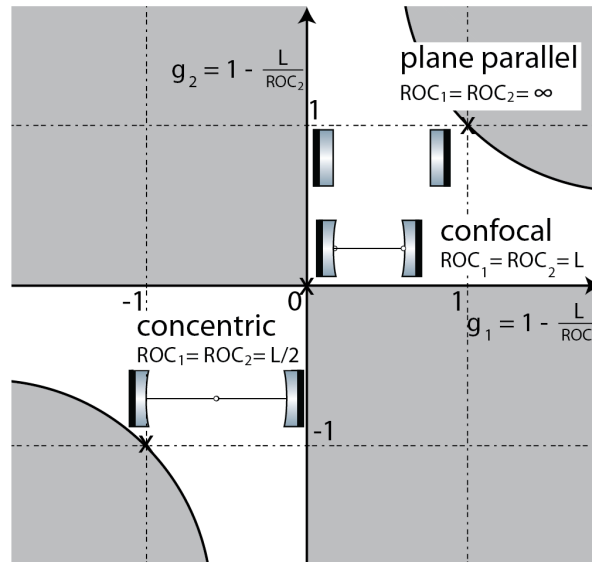


**Figure 4.2.:** Stability diagram for different resonator configurations (reproduced from [KL66]). The coordinate axes are  $g_1$  and  $g_2$ . The parameters  $L/ROC_1$  and  $L/ROC_2$  are drawn as additional coordinate axes with dashed lines. Resonators in the areas bound by the lines  $g_1 = 1$  and  $g_2 = 1$  and the coordinate axes are stable. Cavities on the border of the shaded areas are marginally stable.

## 4. Fundamentals of optical resonators

### 4.2. Cavity dynamics

The theoretical derivation of the cavity dynamics is essential for the description and interpretation of the experimental results in generating and using squeezed states (see Chap. 6). Therefore, let us consider a bow-tie resonator adapted to the experimental conditions. The theoretical derivation of the intracavity dynamics follows [WM07].

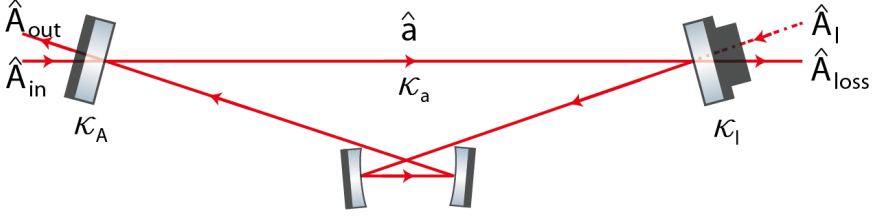


**Figure 4.3.:** Schematic of a bow-tie cavity for a detailed description of the different light fields. The intracavity field  $\hat{a}$  has a decay rate of  $\kappa_a$  and is coupled to the driving field  $A_{in}$  via the input coupler with reflectivity  $r_{in}$  (or decay rate  $\kappa_A$ ) and its reflected field which is simultaneously  $A_{out}$ . In addition, there is a mirror representing losses due to scattering or absorption ( $A_{loss}$ ) and intracavity loss  $A_l$  with the decay rate  $\kappa_l$ .

#### The single-ended cavity

The bow-tie resonator, shown in Fig. 4.3, consists of one input/output-coupling mirror, compared to which all other mirrors have a negligible transmittance, such that the reflected port is simultaneously the transmitted one. As a result, when resonance is achieved the entire power of the intracavity field  $\hat{a}$  is coupled out to the field  $\hat{A}_{out}$  with the decay rate  $\kappa_a$ . To describe every possible port for transmission, reflection and loss in a generalized form one can address the mirrors individually (see [McK08]). There is an input coupler with reflectivity  $r_{in}$  (or decay rate  $\kappa_A$ ) for the driving field  $A_{in}$  and its reflected field which is simultaneously  $A_{out}$ , and finally a mirror representing losses due to scattering or absorption ( $A_{loss}$ ) and intracavity loss  $A_l$  with the decay rate  $\kappa_l$  (see Eq. (4.17)).

#### 4.2.1. Equations of motion for light fields

For this system the equation of motion for the cavity mode  $\hat{a}$  is written

$$\dot{\hat{a}} = -(\kappa_a + i\omega_0)\hat{a} + \sqrt{2\kappa_A}\hat{A}_{in}e^{-i\omega At} + \sqrt{2\kappa_l}\hat{A}_l. \quad (4.15)$$

Writing Eq. (4.15) in the rotating frame reference  $\hat{a} \rightarrow \hat{a}e^{i\omega_A t}$  [GC85] with the cavity detuning  $\Delta_a = \omega_0 - \omega_A$  defined as the difference between the frequency of the driving field  $\omega_A$  and the resonant frequency of the cavity  $\omega_0$  leads to

$$\dot{\hat{a}} = -(\kappa_a + i\Delta)\hat{a} + \sqrt{2\kappa_A}\hat{A}_{\text{in}} + \sqrt{2\kappa_l}\hat{A}_l, \quad (4.16)$$

where  $\kappa_j$  (with  $j = a, \text{in}, \text{out}, l$ ) is the total resonator decay rate for each field, defined (in half width half maximum, HWHM) by  $2\kappa_a = -c/L \cdot \ln[R_1 \cdot R_2 \cdot R_3 \cdot R_4 \cdot (1-l)]$  (cf. [SH98]) where  $l$  is the intracavity loss,  $L$  the cavity length,  $c$  the speed of light and  $R_i$  is the power reflectivity of the mirrors forming the bow-tie cavity (see Sec. 6.3). The sum of all decay rates results in the total decay rate

$$\kappa_a = \kappa_A + \kappa_l. \quad (4.17)$$

Assuming that the cavity frequency is locked at the fundamental all detuning terms with  $\Delta$  can be neglected. Taking into account that Eq. (4.16) is complex the formulation must be expanded by its Hermitian conjugate:

$$\begin{aligned} \dot{\hat{a}} &= -\kappa_a \hat{a} + \sqrt{2\kappa_A}\hat{A}_{\text{in}} + \sqrt{2\kappa_l}\hat{A}_l, \\ \dot{\hat{a}}^\dagger &= -\kappa_a \hat{a}^\dagger + \sqrt{2\kappa_A}\hat{A}_{\text{in}}^\dagger + \sqrt{2\kappa_l}\hat{A}_l^\dagger. \end{aligned} \quad (4.18)$$

Approximation via linearization (see Sec. 2.3.2) of Eq. (4.16) leads to the equation of motion for the mean field amplitudes

$$\begin{aligned} \dot{\alpha} = 0 &= -\kappa_a \alpha + \sqrt{2\kappa_A}\alpha_{\text{in}} + \sqrt{2\kappa_l}\alpha_l, \\ \dot{\alpha}^* = 0 &= -\kappa_a \alpha^* + \sqrt{2\kappa_A}\alpha_{\text{in}}^* + \sqrt{2\kappa_l}\alpha_l^*, \end{aligned} \quad (4.19)$$

and to the fluctuating terms

$$\delta\dot{\hat{a}} = -\kappa_a \delta\hat{a} + \sqrt{2\kappa_A}\delta\hat{A}_{\text{in}} + \sqrt{2\kappa_l}\delta\hat{A}_l, \quad (4.20)$$

$$\delta\dot{\hat{a}}^\dagger = -\kappa_a \delta\hat{a}^\dagger + \sqrt{2\kappa_A}\delta\hat{A}_{\text{in}}^\dagger + \sqrt{2\kappa_l}\delta\hat{A}_l^\dagger. \quad (4.21)$$

### 4.2.2. Input-output formalism

So far, the mathematical consideration of complex light field amplitudes (see Sec. 4.1.1) explains the intracavity dynamics by treating the external fields as passive systems (a heat bath) with a coupling at equilibrium. However, considering that there is a variable input field interfering with the single input/output-coupling mirror and an additional loss field entering the cavity (see Fig. 4.3), these external fields

## 4. Fundamentals of optical resonators

---

actively influence the system [WM07]. Collet and Gardiner approach the interaction between the intracavity field  $\hat{a}$  and external operators  $\hat{A}_{\text{in}}$  and  $\hat{A}_{\text{l}}$  in terms of frequency components via the Heisenberg-Langevin equation [GC85] to formulate the “boundary conditions”:

$$\begin{aligned}\sqrt{2\kappa_A}\hat{a} &= \hat{A}_{\text{out}} + \hat{A}_{\text{in}}, \\ \sqrt{2\kappa_A}\hat{a}^\dagger &= \hat{A}_{\text{out}}^\dagger + \hat{A}_{\text{in}}^\dagger.\end{aligned}\tag{4.22}$$

It represents the relation of the fields outside the cavity to the intracavity field. Since we are interested in measuring the outcoupled field  $\hat{A}_{\text{out}}$  we observe a contribution of the interference between the driving field  $\hat{A}_{\text{in}}$  and the intracavity field  $\hat{a}$ . The resulting steady state field  $\alpha_{\text{out}}$  emerges as

$$\alpha_{\text{out}} = \sqrt{2\kappa_A}\alpha - \alpha_{\text{in}}\tag{4.23}$$

and the complex conjugate is

$$\alpha_{\text{out}}^* = \sqrt{2\kappa_A}\alpha^* - \alpha_{\text{in}}^*.\tag{4.24}$$

Inserting these boundary conditions into Eq. (4.19) leads to the mean field amplitudes at the output fields

$$\begin{aligned}\alpha_{\text{out}} &= \frac{(\sqrt{2\kappa_A} - \kappa_a)\alpha_{\text{in}} + \sqrt{2\kappa_l}\alpha_l}{\kappa_a}, \\ \alpha_{\text{out}}^* &= \frac{(\sqrt{2\kappa_A} - \kappa_a)\alpha_{\text{in}}^* + \sqrt{2\kappa_l}\alpha_l^*}{\kappa_a}.\end{aligned}\tag{4.25}$$

This describes the amplitude of the field that couples out of the cavity being frequency stabilized.

### Fourier transformation of the equations of motion

The result of the fluctuating part of the equation of motion (see Eq. (4.21)) can be found by moving to the Fourier frequency domain  $\text{FT}[\mathbf{a}(t)/dt] = -i\omega\text{FT}[\mathbf{a}](\omega)$ . The equations of motion (see Eq. (4.18)) for the frequency fluctuating part are transformed to

$$\begin{aligned}i\omega\delta\hat{a}(\omega) &= -\kappa_a\delta\hat{a}(\omega) + \sqrt{2\kappa_A}\delta\hat{A}_{\text{in}}(\omega) + \sqrt{2\kappa_l}\delta\hat{A}_l(\omega), \\ i\omega\delta\hat{a}^\dagger(\omega) &= -\kappa_a\delta\hat{a}^\dagger(\omega) + \sqrt{2\kappa_A}\delta\hat{A}_{\text{in}}^\dagger(\omega) + \sqrt{2\kappa_l}\delta\hat{A}_l^\dagger(\omega)\end{aligned}\tag{4.26}$$

By applying the boundary condition to Eq. (4.26), the fluctuating part of the output field can be expressed as

$$\begin{aligned}\delta\hat{A}_{\text{out}}(\omega) &= \frac{(2\kappa_A - \kappa_a - i\omega)\delta\hat{A}_{\text{in}}(\omega) + 2\sqrt{\kappa_A\kappa_l}\delta\hat{A}_l(\omega)}{\kappa_a + i\omega}, \\ \delta\hat{A}_{\text{out}}^\dagger(\omega) &= \frac{(2\kappa_A - \kappa_a - i\omega)\delta\hat{A}_{\text{in}}^\dagger(\omega) + 2\sqrt{\kappa_A\kappa_l}\delta\hat{A}_l^\dagger(\omega)}{\kappa_a + i\omega}.\end{aligned}\quad (4.27)$$

### Equations of motion in quadrature operators

The description of the equations of motion in the amplitude and phase quadrature operators is useful as the detection setup (see Chap. 3) with a spectrum analyzer directly measures the variances. The quadrature operators for the steady state and the fluctuating part of the driving field  $\hat{A}_{\text{in}}$ , the loss field  $\hat{A}_l$  and the outcoupled field  $\hat{A}_{\text{out}}$  are defined as

$$\begin{aligned}X_j^+ &= \alpha_j + \alpha_j^*, \\ X_j^- &= i(\alpha_j - \alpha_j^*),\end{aligned}\quad (4.28)$$

for  $j = \text{in}, \text{out}$  and  $l$ . The quadrature operators for the fluctuating components (see Eq. (2.12)) are

$$\begin{aligned}\delta\hat{X}_{A_j}^+(\omega) &= \delta\hat{A}_j(\omega) + \delta\hat{A}_j^\dagger(\omega), \\ \delta\hat{X}_{A_j}^-(\omega) &= i(\delta\hat{A}_j(\omega) - \delta\hat{A}_j^\dagger(\omega)),\end{aligned}\quad (4.29)$$

for  $j = \text{in}, \text{out}$  and  $l$ . This leads to the following amplitude and phase quadratures for  $\hat{a}_{\text{out}}$  in steady state  $\alpha_{\text{out}}$

$$X_{\alpha_{\text{out}}}^\pm = \frac{(\sqrt{2\kappa_A} - \kappa_a)X_{\alpha_{\text{in}}}^\pm + \sqrt{2\kappa_l}X_{\alpha_l}^\pm}{\kappa_a},\quad (4.30)$$

and for the fluctuating part of the output field  $\delta\hat{A}_{\text{out}}$

$$\delta\hat{X}_{A_{\text{out}}}^\pm(\omega) = \frac{(2\kappa_A - \kappa_a - i\omega)\delta\hat{X}_{A_{\text{in}}}^\pm(\omega) + 2\sqrt{\kappa_A\kappa_l}\delta\hat{X}_{A_l}^\pm(\omega)}{\kappa_a + i\omega}.\quad (4.31)$$

We use the following definition for the quadrature variance:

$$V^\pm \equiv \underbrace{\langle |\delta\hat{X}^\pm|^2 \rangle}_{=0} - \langle |\delta\hat{X}^\pm|^2 \rangle \equiv \langle |\delta\hat{X}^\pm|^2 \rangle,$$

## 4. Fundamentals of optical resonators

---

which leads to the corresponding variances

$$V_{A_{\text{out}}}^{\pm} = \frac{\left( (2\kappa_A - \kappa_a)^2 + \omega^2 \right) V_{A_{\text{in}}}^{\pm} + 4\kappa_l \kappa_A}{\kappa_a^2 + \omega^2}, \quad (4.32)$$

assuming that the incoupled loss field is the vacuum state ( $V_{A_l}^{\pm} = 1$ ). The phase and amplitude quadrature of the outcoupled steady state intracavity field  $\hat{a}$  in Eq. (4.30) represent the measurable light field that can be used for stabilizing the cavity. The variance of the fluctuating part of the output field in Eq. (4.32) represents the squeezing spectrum that is detected in the experiment (see Chap. 6 and 7).



# 5

## Chapter 5

# Cavity dynamics with $\chi^{(2)}$ nonlinearities

This chapter gives a theoretical overview of the nonlinear processes in dielectric media and how they can affect cavity dynamics when placed inside an optical resonator. In particular, this is used for the squeezed-state generation whose experimental realization is a central part of this work.

The nonlinear medium provides an exchange of photons between the interacting fields resulting in the processes of *parametric down-conversion* (PDC) and *second-harmonic generation* (SHG), described in the first part of this chapter. By extending the cavity dynamics presented in Sec. 4.2 with the nonlinear  $\chi^{(2)}$  interaction, it is possible to investigate the variance of the output quadratures of an OPO in terms of squeezing, described in the second part. The resulting equations are used to investigate a novel pump phase-locking technique in Chap. 7 and to realize high-precision metrology enhanced by a FP cavity with squeezed-light injection in Chap. 8.

## 5.1. Interaction with $\chi^{(2)}$ nonlinearities

When light passes through a medium the electromagnetic field induces a periodic displacement of the bound charges in that medium according to its polarizability [Boy03]. As a result of these oscillating electric charges a secondary electromagnetic field is emitted. If the incoming light field has low intensity the displacement is very small, the electric charge driven by the restoring force behaves like a harmonic oscillator far off resonance and the emitted light possesses solely the

## 5. Cavity dynamics with $\chi^{(2)}$ nonlinearities

---

primary excitation frequency which defines a linear process. A higher intensity causes a larger displacement such that the electric charge of neighboring atoms interact. There is no longer a strictly linear correlation between the excited displacement of the electric charge and the restoring force. This nonlinearity implies that the emitted light also possesses possible harmonic frequencies of varying magnitudes in addition to the primary excitation frequency. The strengths and frequencies depend on the structure and density of the transilluminated medium. The efficiency in generating harmonic frequencies decreases significantly with the order of the nonlinearity. The experimental components which are typically used in a squeezing experiment are nonlinear cavities for SHG and PDC. These devices are described in detail in Sec. 6.2 and Sec. 6.3.

To examine the second-order optical nonlinear interaction process we follow [Boy03] and calculate the forces resulting from the nonlinear interactions with a mathematical vector field expression, the *polarization density*.

### 5.1.1. Polarization density

The starting point for the derivation of nonlinear effects are Maxwell's equations (see Eq. (2.1)), where we restrict the analysis to the interaction of the electric field with the dielectric medium. Inside the medium the electric field must be replaced with the electric flux density  $\mathbf{D}$ , defined by the polarization density  $\mathbf{P}$

$$\mathbf{D} = \varepsilon_0 \mathbf{E} + \mathbf{P}, \quad (5.1)$$

where  $\varepsilon_0$  is the electric permittivity in vacuum and  $\mathbf{E}$  is the electric field of the light. For low intensities the polarization density  $\mathbf{P}$  is proportional to the electric field

$$\mathbf{P} = \varepsilon_0 \chi \mathbf{E}, \quad (5.2)$$

where  $\chi$  is the linear electric susceptibility. It is a measure of the induced polarization by a given electric field. For higher electric field intensities the linear relation from Eq. (5.2) is no longer a good approximation (because of  $I(t) \propto E(t)^2$ ) and additional terms with  $P(t)$  as a function of higher-order powers of  $E(t)$  are taken into account [SH98]. The polarization density can be described by a Taylor series expansion in terms of the electrical field with the coefficients being

the higher-order susceptibilities:

$$\mathbf{P} = \varepsilon_0 \sum_n \chi^{(n)} \mathbf{E}^n = \varepsilon_0 \left[ \chi^{(1)} \mathbf{E} + \chi^{(2)} \mathbf{E}^2 + \chi^{(3)} \mathbf{E}^3 + \dots \right], \quad (5.3)$$

where  $\chi^{(1)}$  is referred to as the linear susceptibility,  $\chi^{(2)}$  is the second-order susceptibility (responsible for PDC and SHG, see Fig. 5.1b), and  $\chi^{(3)}$  is the third-order susceptibility (responsible for Kerr effect and four-wave-mixing).

### 5.1.2. Parametric down-conversion and second harmonic generation

The squeezed-light generation presented in this work, is achieved with PDC, which is a quadratic nonlinear process. After establishing the theory in 1961 [LYS61] Wu et al. succeeded in the first experimental realization in 1986 [WKHW86]. In contrast to atomic (vapor) squeezing via four-wave-mixing [SHY<sup>+</sup>86] or the approach of Kerr-squeezing in a SiO<sub>2</sub> fiber [MLS<sup>+</sup>87] using the third-order susceptibility  $\chi^{(3)}$ , PDC is based on the stronger second-order susceptibility  $\chi^{(2)}$ .

The interaction of the photons of three fields (labeled as pump, signal and idler field) at frequencies  $\omega_{\text{pump}}$ ,  $\omega_s$  and  $\omega_i$  in the nonlinear medium (see Fig. 5.1) is subject to the conservation of energy:  $\hbar\omega_s + \hbar\omega_i = \hbar\omega_{\text{pump}}$ . The Hamiltonian for the mixing of three waves is [SRH<sup>+</sup>13]

$$\hat{\mathcal{H}} = \hbar\omega_i \hat{a}^\dagger \hat{a} + \hbar\omega_s \hat{b}^\dagger \hat{b} + \hbar\omega_{\text{pump}} \hat{c}^\dagger \hat{c} + i\hbar\chi^{(2)} \left( \hat{a}\hat{b}\hat{c}^\dagger + \hat{a}^\dagger\hat{b}^\dagger\hat{c} \right), \quad (5.4)$$

where  $\hat{a}$ ,  $\hat{b}$  and  $\hat{c}$  are the annihilation operators for the idler, signal and pump fields respectively and the Hermitian adjoint operators are the creation operators for the fields. The coupling strength for the nonlinear interaction is labeled with  $\chi^{(2)}$  and the interaction terms of operators describe the two processes of PDC and SHG. This leads to the effective Hamiltonian for the nonlinear interactions under consideration [SRH<sup>+</sup>13]:

$$\hat{\mathcal{H}}_{\text{eff}} = i\hbar\chi^{(2)} \left( \underbrace{\hat{c}^\dagger \hat{a}\hat{b}}_{\text{SHG}} + \underbrace{\hat{c}\hat{a}^\dagger \hat{b}^\dagger}_{\text{PDC}} \right). \quad (5.5)$$

In the PDC process a high energy photon is converted into two lower energy photons, whereas for SHG two lower energy photons are converted into a high energy photon (see Fig. 5.1b).

## 5. Cavity dynamics with $\chi^{(2)}$ nonlinearities

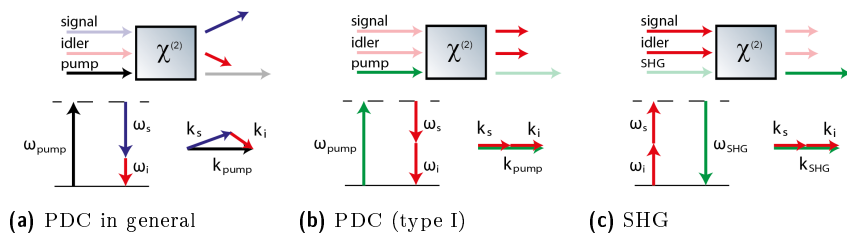


**Figure 5.1.:** PDC and SHG in the energy and momentum pictures. (a) General representation of parametric down-conversion in energy and momentum picture: the generated signal and idler fields are distinguishable in frequency and wave vector. (b) Parametric down-conversion (type I) is described in the energy and momentum picture. The generated signal and idler fields are degenerate in frequency and polarization. Their wave vectors have the same direction. (c) Second harmonic generation is described in the energy and momentum picture. It shows the complementary process to PDC (type I), shown in (b).

If the two lower-energy photons are degenerate in frequency and polarization the process is called type I PDC, for which  $2 \cdot \hbar\omega_s = 2 \cdot \hbar\omega_i = \hbar\omega_{\text{pump}}$ . The complementary process to PDC is the up-conversion (or SHG:  $\hat{c}^\dagger \hat{a} \hat{b}$ ) of two degenerate low-energy photons into one photon with twice the energy:  $\hbar\omega_s + \hbar\omega_i = 2\hbar \cdot \omega_s = 2\hbar \cdot \omega_i = \hbar\omega_{\text{SHG}}$ , commonly called *frequency doubling*. In fact, frequency doubling of an infrared solid state laser is commonly implemented in many commercial laser systems with a wavelength of 532 nm.

### 5.1.3. Phase matching

As illustrated in Fig. 5.1 the conservation of energy and momentum plays an important role for both PDC and SHG. The conservation of momentum is achieved by phase matching. Due to dispersion both the fundamental and pump field experience different refractive indices of the nonlinear medium and this causes a difference in the propagation velocity of the fields. The momentum  $p_i = \hbar k_i$  of a light field is given by its wave vector  $k$ , leading to a further restriction

$$k_s + k_i = k_{\text{pump}}. \quad (5.6)$$

The wave vectors themselves are defined as

$$k_i = \frac{\omega_i n(\omega_i)}{c_0}, \quad (5.7)$$

where  $c_0$  is the speed of light in vacuum and  $n(\omega_i)$  the frequency-dependent index of refraction. By inserting this equation into Eq. (5.6) and considering  $2 \cdot \hbar\omega_s = 2 \cdot \hbar\omega_i = \hbar\omega_{\text{pump}}$  it is obvious that

$$2n(\omega_i) = n(\omega_{\text{pump}}) \quad (5.8)$$

must be guaranteed for efficient conversion. Thus, the evolution of the interacting fields depends on how both fields propagate with the same velocity to ensure a constant phase relation for the optimal nonlinear coupling. This phase matching is a function of the coherence length of the interacting fields in the nonlinear medium [Boy03]:

$$l_{\text{coh}} = \frac{\pi}{k_{\text{pump}} - 2k_i}. \quad (5.9)$$

This coherence length is a measure of how far the pump light will travel into the medium and produce the fundamental, before the process is reversed and any power will couple back to the pump light. For perfect phase matching ( $k_{\text{pump}} = 2k_i$ ), the coherence length becomes arbitrarily large. A phase mismatch can decrease the efficiency of the process of PDC by partly reversing the process and producing a second-harmonic field over the length of the nonlinear medium. The influence of phase matching and phase mismatch is illustrated in Fig. 5.2 by the phasor representation, dividing the generated light field into incremental components (with the vector sum constituting an effective phasor). A phase mismatch after the length of  $l_{\text{coh}}$  (see Fig. 5.2a) leads to a cancellation of the added incremental components. However, given perfect phase matching all field components sum up perfectly (see Fig. 5.2b). Due to dispersion being inherent in most of the dielectric nonlinear media perfect phase matching is usually not possible. Therefore, some methods were excogitated to facilitate this.

In this thesis two types of phase matching are used. The first is birefringent phase matching (BPM) (see [Gio62] for more details) for a magnesium doped lithium niobate (Mg:LiNbO<sub>3</sub>) crystal in a linear cavity for SHG. The second is quasi-phase-matching (QPM) (see [ABDP62] for more details) for the periodically-poled crystal of potassium titanyl phosphate (PPKTP) in a sub-threshold bow-tie cavity for OPO. As the frequency-dependent index of refraction is temperature sensitive tuning of the phase matching conditions via temperature change is possible.

## 5. Cavity dynamics with $\chi^{(2)}$ nonlinearities

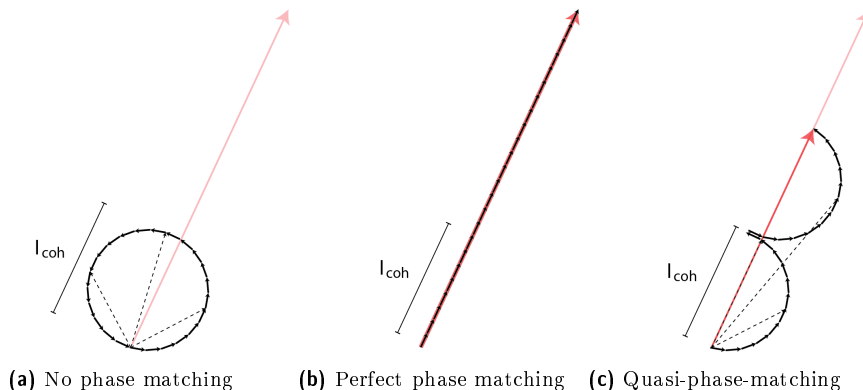


**Figure 5.2.:** Phase-matching conditions in phasor representation (remodeled from [McK08]). In the case of a phase mismatch the incremental components of the generated light field (black arrows) are not phase matched to the incoming field (red arrow). The effective phase of the generated field is depicted as dashed arrows. (a) After the coherence length  $l_{\text{coh}}$  any power of the generated light field is coupled back. (b) In the phase-matched case all incremental components sum up perfectly and the power remains in the generated field. (c) In a quasi-phase-matched case the incremental component of the generated light field is reversed after each coherence length  $l_{\text{coh}}$  to compensate the phase mismatch.

### Birefringent phase matching

The birefringence of the nonlinear medium gives rise to phase matching by using one polarization for the pump field and the perpendicular one for the signal and idler field. This is called type I birefringent phase matching. In contrast, for type II birefringent phase matching the fundamental fields (signal and idler) are orthogonally polarized. Both types of birefringent phase matching must be tuned to maintain the match of the indices of refraction with their temperature and wavelength dependencies described by the Sellmeier equations [ENKB91].

### Quasi-phase-matching by periodic poling

The periodic poling of the crystal for QPM compensates for not operating under phase-matched conditions. The successive reversion of the sign of the second-order nonlinearity at periodic intervals (the coherence length  $l_{\text{coh}}$ ) inside the crystal, leads to a matching of the interacting wave phase velocities even if they are not phase-matched in a classical sense (see Fig. 5.2c). Compared to other phase matching

## 5.1. Interaction with $\chi^{(2)}$ nonlinearities

---

techniques QPM allows for crystal directions with very high nonlinearity factors to be utilized. Even if there are imperfections in the domain widths QPM is still increasing the second-order nonlinear effect [FMJB92]. Therefore, a periodically-poled crystal (PPKTP) was used for the sub-threshold OPO, described in Chap. 6.

### 5.2. Intracavity dynamics with interacting $\chi^{(2)}$ nonlinearities

By adding a nonlinear medium to the cavity dynamics derived in Sec. 4.2 additional field and interaction terms between the fundamental (seed field)  $\hat{A}_{\text{in}}$  and the second-harmonic (pump field)  $\hat{B}_{\text{in}}$  are introduced. Here, the extended formalism is introduced and derived to calculate the variance of the output field that corresponds to the behavior of the OPO (see Sec. 6.3). In Chap. 7 we will use these equations to investigate a novel pump phase-locking scheme. Again we consider the experimental setup by describing the cavity.

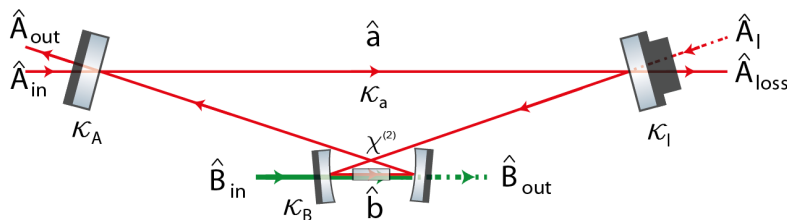


**Figure 5.3.:** Schematic of a bow-tie cavity for a detailed description of the nonlinear interactions. In addition to the empty cavity (see Fig. 4.3) there is the nonlinear crystal placed between the curved mirrors and the driving pump field  $B_{\text{in}}$  is sent through in a single pass configuration, since the cavity is not resonant for the pump field. However, due to the nonlinear interactions in the crystal the pump field contributes to the intracavity dynamics as well.

The cavity described in Fig. 5.3 is only resonant for the seed field and a single pass configuration for the pump field. However, due to the nonlinear interactions in the crystal the pump field contributes to the intracavity dynamics as well. Considering that there is (weak) depletion in the pump field population a phase-sensitive readout for the pump field can be obtained. Exploiting this *weak pump depletion* (WPD) effect for generating a phase-sensitive error signal is the basis of our WPD locking technique [DSW<sup>+</sup>15], a locking scheme to stabilize the phase difference between the seed and pump fields (see Chap. 7).

#### 5.2.1. Hamiltonian and equations of motion

We investigate the case of a nonlinear crystal placed in a folded four-mirror bow-tie cavity. The Hamiltonian describing this second-order



## 5.2. Intracavity dynamics with interacting $\chi^{(2)}$ nonlinearities

nonlinear interaction of the cavity modes at fundamental (displayed by the annihilation and creation operators  $\hat{a}$  and  $\hat{a}^\dagger$ ) and second-harmonic frequency ( $\hat{b}$  and  $\hat{b}^\dagger$ , respectively) is given by [WM07]

$$\hat{\mathcal{H}} = i\hbar\chi_c \left( \hat{b}^\dagger \hat{a}^2 - \hat{a}^\dagger \hat{b} \right), \quad (5.10)$$

where the coupling constant  $\chi_c$  is proportional to the second-order nonlinear susceptibility  $\chi^{(2)}$  and the amplitude of the pump field. In combination with the cavity equations of motion this leads to the following equations [CG84]

$$\begin{aligned} \dot{\hat{a}} &= -2\chi_c \hat{a}^\dagger \hat{b} - (\kappa_a + i\Delta_a) \hat{a} + \sqrt{2\kappa_A} \hat{A}_{\text{in}} + \sqrt{2\kappa_l} \hat{A}_l, \\ \dot{\hat{b}} &= \chi_c \hat{a}^2 - (\kappa_b + i\Delta_b) \hat{b} + \sqrt{2\kappa_B} \hat{B}_{\text{in}} + \sqrt{2\kappa_l^b} \hat{B}_l, \end{aligned} \quad (5.11)$$

where  $\kappa_a$  and  $\kappa_b$  are the total resonator decay rates for each field (see Eq. (4.16)). Further cavity dynamics, especially for the pump field, are described in detail in Chap. 7 to derive the effect of WPD.

### Undepleted pump field

It is an established simplification in the theory of squeezed-light generation to ignore the depletion of the pump field as it generates secondary photons. In this case, applying the mean field approximation and substituting  $\hat{q} = 2\chi_c \cdot \hat{b} e^{i\theta_b}$  (and  $\hat{q}^\dagger = 2\chi_c \cdot \hat{b}^\dagger e^{-i\theta_b}$ ), the cavity fields of interest (at a wavelength of 1064 nm) are calculated (see for comparison Eq. (4.21)):

$$\begin{aligned} \dot{\hat{a}} &= -(\kappa_a + i\Delta_a) \hat{a} - \hat{q} \cdot \hat{a}^\dagger + \sqrt{2\kappa_A} \hat{A}_{\text{in}} + \sqrt{2\kappa_l} \hat{A}_l, \\ \dot{\hat{a}^\dagger} &= -(\kappa_a + i\Delta_a) \hat{a}^\dagger - \hat{q}^\dagger \cdot \hat{a} + \sqrt{2\kappa_A} \hat{A}_{\text{in}}^\dagger + \sqrt{2\kappa_l} \hat{A}_l^\dagger. \end{aligned} \quad (5.12)$$

The phase angle  $\theta_b$  in the substituted forms of  $\hat{q}$  and  $\hat{q}^\dagger$  represents the phase difference between the pump field and the cavity field. Investigating the intracavity field amplitude in steady state of Eq. (5.12), where  $\dot{\hat{a}} = 0$  and  $\dot{\hat{a}^\dagger} = 0$ , leads to

$$\alpha = \frac{\sqrt{2\kappa_A} \alpha_{\text{in}} (\kappa_a + i\Delta_a - q)}{(\kappa_a + i\Delta_a)^2 - |q|^2}. \quad (5.13)$$

This equation will be important for closer examination of the calculated squeezing spectrum  $V_{A_{\text{out}}}^\pm$  as a function of the frequency and the FSR [DHHR06] (see Sec. 8.1).

## 5. Cavity dynamics with $\chi^{(2)}$ nonlinearities

---

### 5.2.2. Noise variances in quadrature operators

Analogous to the case of an empty cavity (see Eq. (4.31)) the amplitude and phase quadrature for the fluctuating part of the output field  $\delta\hat{A}_{\text{out}}$  are described by:

$$\delta\hat{X}_{A_{\text{out}}}^{\pm} = \frac{(2\kappa_A - \kappa_a - i\omega \pm |q|) \delta\hat{X}_{A_{\text{in}}}^{\pm} + 2\sqrt{\kappa_A\kappa_1} \delta\hat{X}_{A_1}^{\pm}}{\kappa_a + i\omega \mp |q|}, \quad (5.14)$$

which leads to the following variances:

$$V_{A_{\text{out}}}^{\pm} = \frac{\left((2\kappa_A - \kappa_a \pm |q|)^2 + \omega^2\right) V_{A_{\text{in}}}^{\pm} + 4\kappa_1\kappa_A V_{A_1}^{\pm}}{\kappa_a^2 + \omega^2 \mp |q|^2}. \quad (5.15)$$

### Frequency dependence off resonance

To investigate a detuning of the cavity the change in the circulating mode amplitude during a round-trip time  $\tau$  must be taken into account. Starting with the equation of motion for the mean field of a nonlinear cavity assuming no pump depletion (see Eq. (5.13)) the detuning term of the fundamental and cavity resonant frequency (following [DHHR06]) can be formulated as:

$$\alpha = \frac{\sqrt{2\kappa_A} \alpha_{\text{in}} \left( \kappa_a - \frac{1-e^{i\Delta_a\tau}}{\tau} - q \right)}{\left( \kappa_a - \frac{1-e^{i\Delta_a\tau}}{\tau} \right) \left( \kappa_a - \frac{1-e^{i\Delta_a\tau}}{\tau} \right) - |q|^2}. \quad (5.16)$$

Deriving the variance from Eq. (5.16) we can calculate the resonant behavior of the generated squeezing and antisqueezing variances (see Fig. 5.4) over several FSRs for a given set of experimental parameters, see Table 7.1. We use these parameters to show a simulation<sup>1</sup> of the generated squeezing of the sub-threshold OPO (see Sec. 6.3), which is used for squeezed-state generation with a novel locking scheme (see Chap. 7) and for high-precision metrology (see Chap. 8).

---

<sup>1</sup>For computing and simulating the equations we used the computer algebra program *Mathematica* developed by **Wolfram Research**.

## 5.2. Intracavity dynamics with interacting $\chi^{(2)}$ nonlinearities

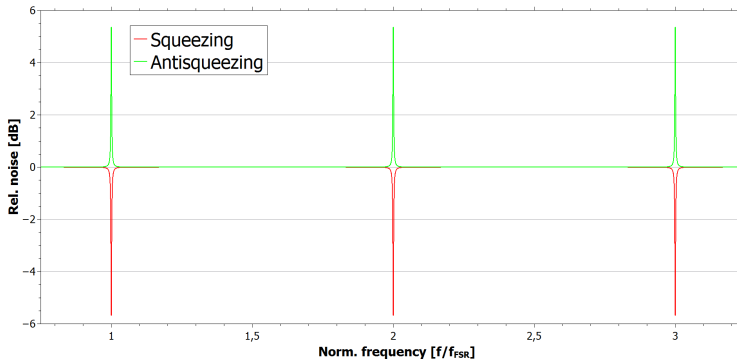


**Figure 5.4.:** Simulation of squeezed noise variances over several FSRs. With Eq. (5.15) it is possible to simulate the resonant behavior of generated squeezing and antisqueezing. These resonances show up on every FSR so that a comb of squeezing-dips and antisqueezing-peaks is generated.

As this process and its detection is subject to losses (compare Sec. 3.5, and see Fig. 3.3), they are included by Eq. (3.24) in a more realistic simulation, shown in Fig. 5.5.

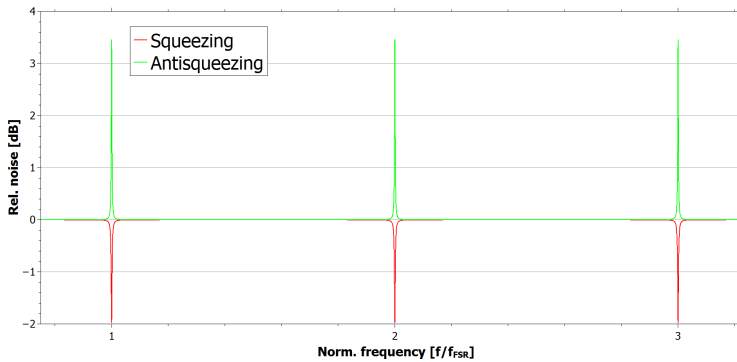


**Figure 5.5.:** Simulation of squeezed noise variances over several FSRs with introduced losses. According to Eq. (3.24) the squeezed and antisqueezed variances from Fig. 5.4 experience losses of  $\eta = 0.5$  (see Table 7.1 for all parameters).

## 5. Cavity dynamics with $\chi^{(2)}$ nonlinearities

---

With the consideration of Eq. (5.16) the cavity dynamics can be described at Fourier frequencies far beyond the resonance [DHHR06] to investigate the variance of the output field  $V_{A_{\text{out}}}^{\pm}$  of the OPO at several FSRs.

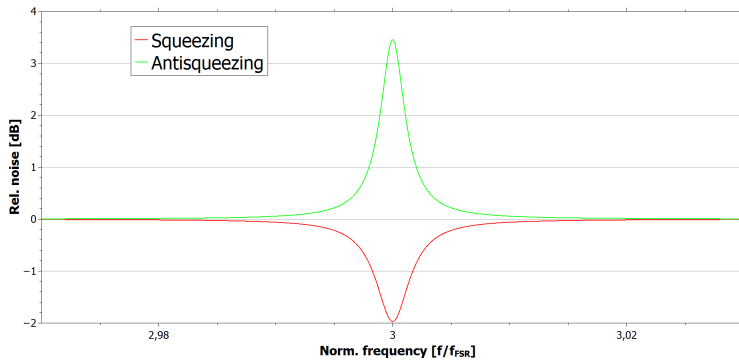


**Figure 5.6.:** Simulation of the squeezing and antisqueezing variances of the third FSR. The simulated plot corresponds with the measurements of the sub-threshold OPO (see Chap. 6.3).

Its remarkable characteristic is the continuous generation of squeezed and antisqueezed states at every FSR, solely decreased only by the introduced losses. For example, the third FSR has a squeezing level of  $-1.96$  dB, which is similar to the first FSR (see Chap. 7), shown in Fig. 5.6 [HWD<sup>+</sup>10].

# 6

## Chapter 6

# Generation of squeezed states

The existence of squeezed vacuum states was first considered in the 1920s by Schrödinger [Sch26], Kennard [Ken27] and Darwin [Dar27]. Discussions about the use of squeezed light led to possible applications in high-precision measurements, quantum computing and quantum communication in the 1980s [Deu85]. Around that time the first experiments with vacuum squeezed states were realized [SHY<sup>+</sup>86]. It was suggested that the sensitivity of laser interferometric gravitational wave detectors (GWDs) could be improved by injecting squeezed vacuum states into the dark port [Cav81]. The first permanent implementation of this method was recently realized in the GWD GEO600 in Hannover [VKL<sup>+</sup>10]. As existing GWDs use massive mirrors as macroscopic test masses and are sensitive at Fourier frequencies of kilohertz down to hertz, the injected squeezed states need to be stabilized on long timescales [VCDS07]. Besides the application in the field of gravitational physics, squeezed states of light are of importance in other major research areas such as continuous variable quantum communication and quantum key distribution [Eke91]. Quantum key distribution protocols, entangled states and quantum teleportation have been demonstrated and improved over the past twenty years [BBC<sup>+</sup>93, DLCZ01, ESB<sup>+</sup>10]. In highly complex large-scale experiments such as GWDs every subsystem (e.g. mode cleaning cavities, SHG or OPO cavities) must be stabilized individually to enable measurements. Every locking task requires a suitable error signal, and various techniques have been demonstrated where such an error signal is provided via either modulation sidebands

## 6. Generation of squeezed states

---

(dither locking, Pound-Drever-Hall technique) [HKEB06, DHK<sup>+</sup>83] or modulation-free via slight misalignment of beams (tilt locking) [RSS<sup>+</sup>02] or polarization (Hänsch-Couillaud locking, homodyne locking) [HC80, HPJH09]. Modulation sidebands provide large error signals, but emerging higher-order modulation frequencies and resulting beat notes can disturb measurements in that frequency range.

This chapter is divided into three parts. First, locking techniques to stabilize the cavity length to the laser frequency of an incident laser are introduced. The need for a pump field to generate squeezed light requires that the cavity for SHG must also be stabilized. The second part describes the implementation of the polarization-based homodyne locking technique to both a linear and a bow-tie cavity with two different types of nonlinear crystals (MgO:LiNbO<sub>3</sub> and PPKTP) and concludes with a comparison. The third part describes the stabilization of the OPO with the simultaneous detection of the squeezed light by the polarization-based homodyne detection of its phase quadrature variance. This setup is compared to a rear-coupled Pound-Drever-Hall (PDH)-locking scheme to investigate the OPO performance.

### 6.1. Frequency locking techniques

Resonators must in general be stabilized to perform on resonance to have the best possible intracavity gain (see Sec. 4.1.2). There are different techniques to obtain a dispersion-shaped error signal that can be used to drive an actuator for cavity length stabilization, e.g. a mirror mounted to a piezoelectric transducer (PZT) crystal for matching the resonator length. Different resonator geometries offer several ports for a dispersion-dependent signal.

#### 6.1.1. Cavity length control mechanisms

To stabilize the cavity length the error signal is fed into a controller (in the further course of this thesis named *servo*) that compares its value with a desired setpoint. A servo accepts parameters that scale proportional (P), integral (I) and derivative (D) terms, for this reason it is often called a PID controller. Depending on the parameters of the system, the combinations and their relative gains must be chosen carefully to ensure an adequate performance and stability. The control signal created by the servo is fed into a high voltage amplifier (HV amplifier) to drive the actuator for cavity length stabilization.

## 6.1.2. Pound-Drever-Hall locking

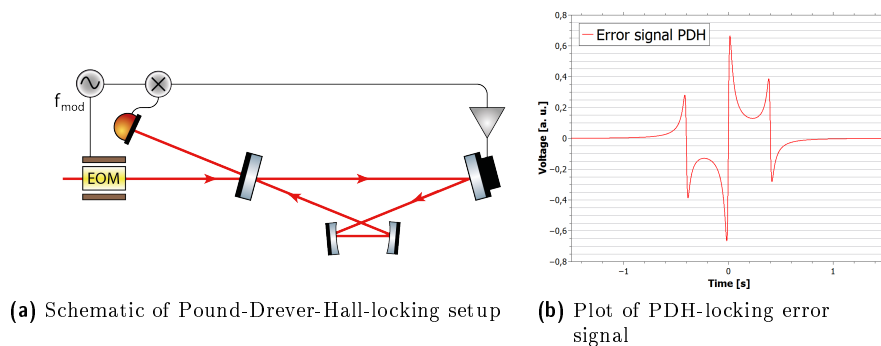


**Figure 6.1.:** Schematical setup and error signal plot of Pound-Drever-Hall locking. the light field passes through an electro-optical modulator (EOM) imprinting a phase modulation at frequency  $f_{\text{mod}}$ . This modulation frequency is not allowed to coincide with a multiple of the FSR and needs to be far above the cavity linewidth, such that the sidebands are reflected, while the carrier is transmitted. The carrier light field couples into the cavity, gets enhanced and the field leaking out of the cavity is recombined with the directly reflected sidebands. A photodiode measures the light in reflection and detects the optical beat between the carrier field and the modulation sidebands.

There is a plausible principle behind the Pound-Drever-Hall (PDH) locking technique [DHK<sup>+</sup>83]: light at a frequency that fluctuates faster than the cavity response can be used to generate an error signal that is not perturbed by the slower cavity length stabilization itself. As Fig. 6.1a shows, the light field passes through an electro-optical modulator (EOM) imprinting a phase modulation at the modulation frequency  $f_{\text{mod}}$ . In the sideband picture representation (see Sec. 2.4.5) two counter-rotating “phasor-arrows” are appended at  $\pm f_{\text{mod}}$  from the carrier. This modulation frequency is not allowed to coincide with a multiple of the FSR and needs to be far above the cavity linewidth, such that the sidebands are reflected, while the carrier is transmitted. The carrier light field couples into the cavity, gets enhanced and the field leaking out of the cavity is recombined with the directly reflected sidebands. A photodiode measures the light in reflection and detects the optical beat between the carrier field and the modulation sidebands. Due to the cavity a phase difference between the carrier and sideband fields occurs that discriminates relative fluctuations of carrier frequency and resonance. The detected signal is multiplied

## 6. Generation of squeezed states

---

with an electronic LO at the same frequency  $f_{\text{mod}}$ . After this demodulation<sup>1</sup> the signal is low-pass filtered to remove beat notes between higher-order mode sidebands and harmonic frequencies to obtain a suitable error signal (see Fig. 6.1b).

### 6.1.3. Dither locking

Comparable to the PDH locking technique is the dither locking stabilization scheme [HKEB06]. In a similar way a small phase modulation signal is imprinted on the light field. The modulation frequency must be within the cavity linewidth to ensure cavity enhancement so that the sidebands are transmitted. Any fluctuations in the cavity lead to a phase shift of the carrier relative to the modulation sidebands. On resonance, this small phase disturbance produces an amplitude modulation that is synchronously detected and demodulated by the photodetector to generate the desired error signal.

### 6.1.4. Polarization-based homodyne locking

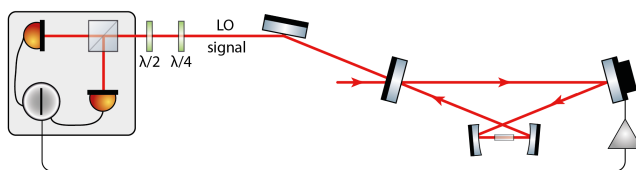


**Figure 6.2.:** Schematic of polarization based homodyne locking setup. For a non-polarization-degenerate cavity the different changes for the linear polarizations (in terms of being perpendicular (s-polarization) and parallel (p-polarization)) due to the cavity plane provide a dispersion-shaped error signal. To detect the resulting ellipticity the polarization-based homodyne detection setup with a QWP and a PBS, described in Sec. 3.4, is used.

An approach without external modulation is to employ polarization spectroscopy of the reflected light field from an anisotropic cavity [HC80]. For a non-polarization-degenerate cavity the different changes for the linear polarizations (in terms of being perpendicular

---

<sup>1</sup>In our experimental setups we used a RIGOL DG 1022 for the modulation and demodulation of the sidebands.



(s-polarization) and parallel (p-polarization)) due to the cavity plane provide a dispersion-shaped error signal. To detect the resulting ellipticity the polarization-based homodyne detection setup with a QWP and a PBS, described in Sec. 3.4, is used. Having a ratio of 50:50 for both intensities of signal and LO the measured differential current generates provide a signal with a steep resonant slope that can be used for stabilization purposes. Changing the ratio of signal to LO to 1:99 leads to a cavity locking technique with the simultaneous detection of the phase quadrature of the signal field fluctuations  $\delta X_{\text{sig}}^-$ .

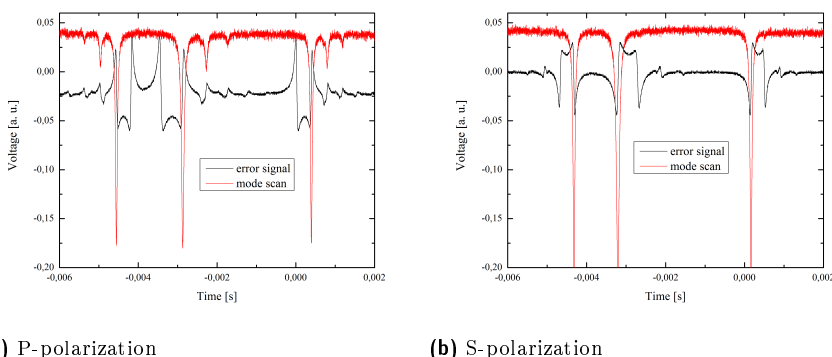


**Figure 6.3.:** Measurement of error signal and cavity mode scan for polarization-based homodyne locking.

The non-degenerate resonance behavior of the cavity gives rise to an intracavity phase shift  $\Delta\phi$  for one polarization component<sup>2</sup>. Considering the restriction of the polarization-based detection for  $\theta = \pi/2$  leads to the already derived Eq. (3.20):

$$i_- = 2\alpha_{\text{sig}}\beta_{\text{LO}} \cos(\theta + \Delta\phi) + \beta_{\text{LO}}\delta X_{\text{sig}}^{-\theta}, \quad (6.1)$$

where the first term is used to stabilize the cavity. The second term describes the possibility of detecting fluctuations of the phase quadrature scaled with the large amplitude of the LO mean value:

$$V_{i_-} = \beta_{\text{LO}}^2 V \delta X_{\text{sig}}^-. \quad (6.2)$$

This leads to a restriction in detecting the phase quadrature of the signal field fluctuations with the benefit of simultaneously locking an

<sup>2</sup>This is the case for a cavity with an odd number of mirrors. In a four-mirror cavity the phase shift is canceled out. A nonlinear medium inside the cavity creates another phase shift due to its birefringence.

## 6. Generation of squeezed states

---

OPO for squeezed-light generation [HPJH09] (see Sec. 6.3). The error signals with the corresponding mode scans for both polarization are shown in Fig. 6.3. The polarization-based homodyne locking technique is used to stabilize almost every subsystem of the experimental setup described in this thesis. To compare two different resonator geometries with two different nonlinear crystals for frequency doubling in the next section this technique is applied to both of them.

## 6.2. Frequency stabilizing a cavity for frequency doubling

To increase the strength of nonlinear interaction provided by a crystal (see Sec. 5.1) a cavity can be assembled around it to increase the interacting seed field. The existence of such a nonlinear medium inside a cavity gives rise to non-degeneracy of the two polarizations so that a well separated and defined error signal is generated (see [HC80, HPJH09]). For this reason the polarization-based homodyne locking technique is applied to two different resonator geometries with two different nonlinear crystals for frequency doubling. The linear and bow-tie cavity for pump field preparation are illustrated in Fig. 6.4.

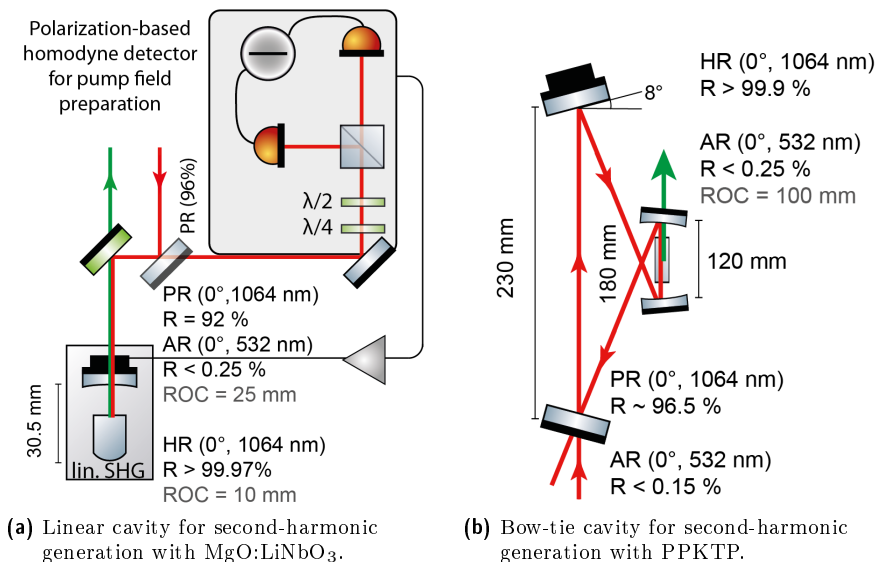


**Figure 6.4.:** Schematic of the linear and the bow-tie cavity for frequency doubling with cavity parameters.

### 6.2.1. Frequency doubling in a linear cavity

To obtain the frequency conversion from 1064 nm to 532 nm a hemilithic standing-wave resonator<sup>3</sup> with a MgO:LiNbO<sub>3</sub>-crystal is used for type I phase-matched SHG [Vah08]. The resonator (see Fig. 6.4a) consists

<sup>3</sup>This linear cavity for SHG was developed by the Quantum Interferometry group led by Prof. Dr. Schnabel. In collaboration with Dr. Mehmet the cavity was implemented and tested for the experiments described in this work.

## 6. Generation of squeezed states

---

of a coupling mirror and the polished and coated rear surface of the nonlinear medium itself. The crystal has dimensions  $2 \times 2.5 \times 7.5 \text{ mm}^3$  and is 7% magnesium oxide doped, which leads to a phase matching temperature of  $\approx 67^\circ\text{C}$ . The rear surface of the crystal has a radius of curvature (ROC) of 10 mm and a high reflection coating ( $R \geq 99.97\%$ ) for the fundamental and second-harmonic wavelength, whereas the flat front surface is anti-reflection coated ( $T > 99.99\%$ ) for both wavelengths. The cavity waist size is  $\omega_{0,532} = 29 \mu\text{m}$ . The partially reflective coupling mirror with ROC = 25 mm has a reflectivity of  $R_{\text{in}} = 92\%$  for the fundamental wavelength. The corresponding finesse of the cavity is  $\mathfrak{F} = 75$  and its FSR is  $\approx 4.9 \text{ GHz}$  based on the distance of 30.5 mm between the coupling mirror and the rear surface of the crystal, leading to a stability parameter of  $g_1g_2 = 0.451$ . The oven design is an in-house production where the crystal is enclosed by copper plates attached to a Peltier element providing constant temperature. In combination with a negative temperature coefficient thermistor (NTC) inside the lower copper plate, it is used to regulate the crystal temperature. By comparing the actual value of the NTC-resistance with the value of an operating point set by the user an electronic controller provides a feedback current to drive the Peltier element.

The generated pump light field is separated from the reflected fundamental field by a dichroic mirror. In transmission of the cavity a photodetector is placed to monitor the cavity performance: by sweeping the PZT-driven incoupling mirror a mode scan of the cavity is possible; by locking the cavity on resonance the constant amplitude of the transmitted light field serves as a confirmation for the successful lock.

The polarization-based homodyne locking scheme is used to stabilize the linear cavity, although it is more common for bow-tie resonators where the incoming and reflected fields are already separated. However, by using a partially transmissive mirror ( $R = 96\%$ ) for steering the fundamental field into the cavity, the outcoupled light field in the reflection path contains the polarization-dependent phase information to generate an error-signal by homodyne detection.

### 6.2.2. Frequency doubling in a bow-tie cavity

For comparison purposes a second cavity for SHG was built as a bow-tie resonator and investigated. This folded resonator (see Fig. 6.4b) consists of two curved mirrors (ROC 100 mm) and two flat mirrors

## 6.2. Frequency stabilizing a cavity for frequency doubling

with an inclination angle of  $8^\circ$ . One flat mirror acts as an in/out-coupler to the cavity (power reflectivity  $R_{\text{in}} = 96.5\%$ ), whereas the remaining mirrors are highly reflective ( $R > 99.9\%$ ) for the fundamental light field. The opposite flat mirror is mounted on a PZT to adjust the cavity length to the laser frequency. In addition, the two curved mirrors are anti-reflective coated for the second-harmonic wavelength at  $532\text{ nm}$  ( $R < 0.25\%$ ) to provide the most efficient single-pass out-coupling for the second-harmonic field. These mirror reflectivities correspond to a cavity finesse of  $\mathfrak{F} = 85$  for  $1064\text{ nm}$ . The length of this folded cavity is  $710\text{ mm}$  which leads to a FSR of  $\approx 422\text{ MHz}$ , and its stability parameter is  $g_1g_2 = 0.98$ . While the second-harmonic field exits the cavity at the second curved mirror, the fundamental intracavity field couples out of the cavity at the in/out-coupler. It is overlapped with the directly reflected field creating the polarization-dependent phase-information for stabilizing the cavity similar to the linear one. The PPKTP-crystal as the nonlinear  $\chi^{(2)}$ -medium for SHG has dimensions  $2 \times 2 \times 10\text{ mm}^3$  and is placed between the two curved mirrors. The custom-designed oven provides the QPM temperature for second-harmonic generation of  $\approx 30^\circ\text{C}$ . The beam waist inside the crystal is  $\omega_{0,1064} \approx 24\ \mu\text{m}$  ( $1/e^2$ ).

### Comparison of frequency doubling in a linear and a bow-tie cavity

Compared to  $\text{MgO}:\text{LiNbO}_3$ , which was used for the hemilitic linear SHG cavity, PPKTP has a larger nonlinear coefficient and shows less absorption at  $1064\text{ nm}$ . While we observe similar conversion efficiencies, the difference in resonator geometry leads to the question if there is a difference in the SHG performance<sup>4</sup> of the two cavities.

<sup>4</sup>The comparison of  $\text{MgO}:\text{LiNbO}_3$  and PPKTP in an optical parametric oscillator was performed by McClelland et al. in a doubly resonant OPO [McK08].

## 6. Generation of squeezed states

**Table 6.1.:** Comparison of frequency doubling in a linear and a bow-tie cavity.

Parameter		linear SHG	bow-tie SHG
Crystal	$\chi^{(2)}$	MgO:LiNbO <sub>3</sub>	PPKTP
Length	$l$	40 mm	710 mm
Free spectral range	FSR	4.9 GHz	422 MHz
Finesse	$\mathfrak{F}$	76	85
Linewidth (FWHM)	$\Delta\nu$	65 MHz	4.9 MHz
Incoupling mirror	$R_{\text{in}}$	92.0 %	96.5 %

As Fig. 6.5 reveals, the performance of both cavities in generating the second-harmonic field as a function of the fundamental field are comparable. The decision to use the linear cavity for the pump field preparation for squeezing experiments, presented in this work, is based on its compact construction. Additionally, the free mounted bow-tie cavity with widely separated components is bound to be more sensitive to air fluctuations than the hemilithic resonator.

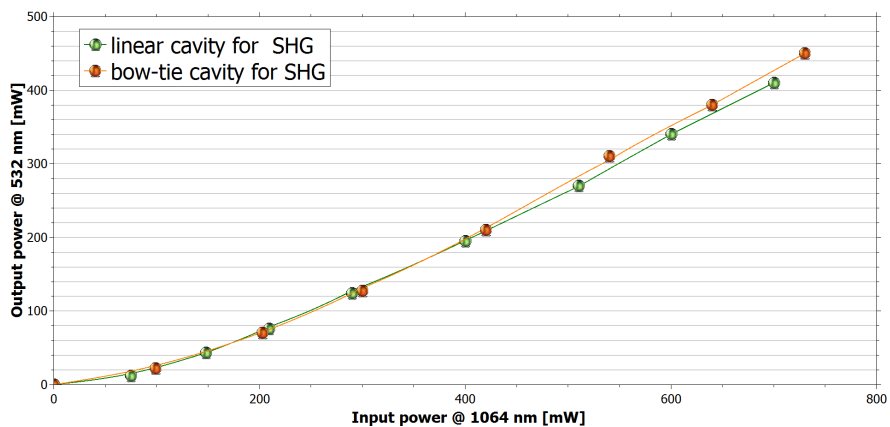


**Figure 6.5.:** Comparison of the performance of linear and bow-tie cavities for second-harmonic generation.

### 6.3. Frequency stabilizing a cavity for parametric down conversion

The OPO is the source of the squeezed light and therefore the core part of the experiments described in this thesis. Firstly it is needed to demonstrate a novel pump phase locking scheme (see Chap. 7) and secondly to enhance signal spectroscopy in a high finesse FP cavity by utilizing the squeezed noise floor (see Chap. 8). The frequency stabilization is accomplished by the polarization-based homodyne locking technique that offers simultaneous detection of the phase amplitude variance. Having the same device for stabilizing the cavity and detecting the squeezed light field makes its use for downstream experiments impossible. It is therefore necessary to consider an alternative locking scheme from the cavity's rear side, leaving the squeezed light field that couples out of the front cavity mirror undisturbed.

Changing the setup enables the comparison of the front locking scheme with the rear locking setup. The implied ratio of signal in s-polarization and LO in p-polarization could be a drawback, since there is no possibility of separately controlling the LO. One cannot measure the homodyne visibility by sweeping the LO with respect to the signal, for example. To discover possible visibility imperfections a comparative PDH locking scheme from the rear mirror was built up.

#### 6.3.1. The OPO cavity design consideration

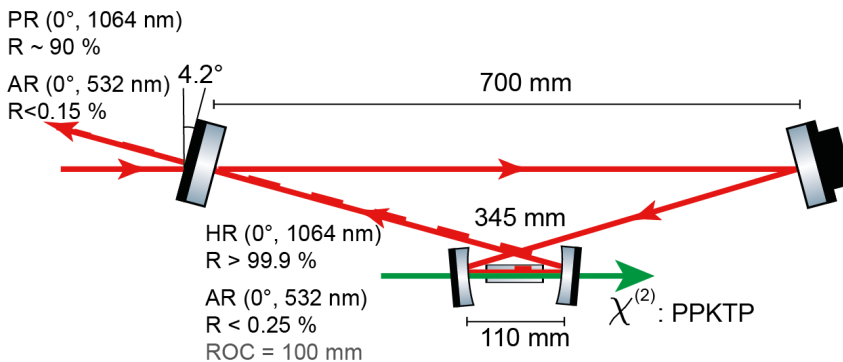


Figure 6.6.: Schematic of the bow-tie cavity for optical parametric oscillation with cavity parameters.

## 6. Generation of squeezed states

---

The sub-threshold bow-tie OPO in Fig. 6.6 consists of two curved mirrors (ROC 100 mm) and two flat mirrors with an inclination angle of  $4.2^\circ$ . One flat mirror acts as an in/out-coupler to the cavity (power reflectivity  $R_{\text{in}} = 90\%$ ) whereas the remaining mirrors are highly reflective ( $R > 99.9\%$  for the fundamental light field). One mirror is mounted on a PZT to adjust the cavity length to the laser frequency (see Fig. 6.6). The two curved mirrors are also anti-reflective coated for the second-harmonic wavelength at 532 nm ( $R < 0.25\%$ ) to provide the most efficient single-pass for the pump field. These mirror reflectivities correspond to a cavity finesse of  $\mathfrak{F} = 58$ . The length of this folded cavity is 1520 mm which leads to a FSR of  $\approx 197.4$  MHz. Regarding the length and radii of curvature the empty cavity is unstable ( $g_1 g_2 = 1.05$ ) but inserting the crystal brings the desired stability ( $g_1 g_2 = 0.95$ ). The  $2 \times 2 \times 10$  mm<sup>3</sup> dimensioned PPKTP crystal is placed between the two curved mirrors to generate squeezing. The temperature for type I PDC with QPM between seed and pump light of  $\approx 30^\circ\text{C}$  is provided by a custom oven design. The beam waist inside the crystal is  $\omega_{0,1064} \approx 24 \mu\text{m}$  ( $1/e^2$ ).



## 6.3. Frequency stabilizing a cavity for parametric down conversion

### 6.3.2. Front lock of the OPO by polarization-based homodyne locking

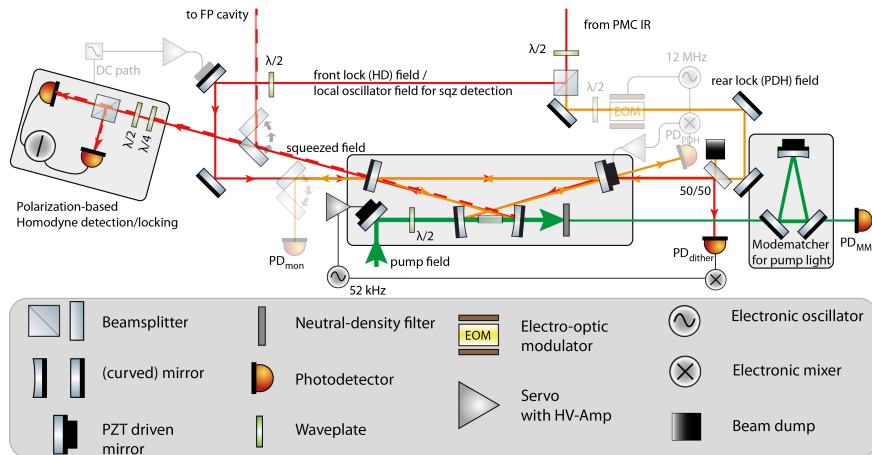


**Figure 6.7.:** Experimental setup of OPO frequency stabilization via front lock and rear lock to utilize the generated squeezed light field. The infrared light field is split into the front lock (HD) field (for frequency stabilization via homodyne detection, see Sec. 6.1.4) and the rear lock (PDH) field (providing a frequency stabilization via PDH locking scheme, see Sec. 6.1.2). The front lock field couples into the cavity by a plane incident angle at the first mirror so that the resulting intracavity field is copropagating with the pump field that couples in at the first curved mirror. The generated squeezed field therefore propagates in the same direction. Likewise, the rear lock field couples at the rear mirror into the cavity resulting in a counterpropagating intracavity field.

In order to exploit all promising options for stabilizing and operating the OPO the infrared light field is split into the front lock (HD) field (for frequency stabilization via homodyne detection, see Sec. 6.1.4) and the rear lock (PDH) field (providing a frequency stabilization via PDH locking scheme, see Sec. 6.1.2) as shown in Fig. 6.7. The front lock field couples into the cavity straight at the input/output-coupling mirror and the resulting intracavity field is copropagating with the pump field at a wavelength of 532 nm that couples in at the first curved mirror. The generated squeezed field therefore propagates in the same direction. To get the most precise spatial overlap, the waist for the pump beam inside the crystal must be  $\omega_{0,532} \approx 18 \mu\text{m}$  ( $1/e^2$ ). A 532 nm mode matching cavity in transmission of the second curved mirror diagnoses the overlap of the green pump field and the seed field

## 6. Generation of squeezed states

---

when the bow-tie cavity acts as a frequency converter for the 1064 nm seed field. The frequency upconverted seed field at a wavelength of 532 nm is directed into the mode matching cavity and detected via  $\text{PD}_{\text{MM}}$  in the same way as the pump field. If the detected mode scan is exactly the same (with all intensity in the fundamental mode at best) for both the upconverted seed field and the pump field, the best possible mode overlap is guaranteed.

A photodetector  $\text{PD}_{\text{dither}}$  is placed in transmission of the OPO to monitor the transmitted light field or detect a mode scan of the cavity by sweeping the PZT of the cavity mirror to change the cavity length. If the pump phase is affecting the intracavity field via the nonlinear interaction of the PPKTP crystal the fluctuations of the transmitted cavity field are detected by  $\text{PD}_{\text{dither}}$  as well. Using the dither locking technique (see Sec. 6.1.3) with a modulation frequency of  $f_{\text{dither}} = 52 \text{ kHz}$  the pump phase for squeezed light generation in the OPO is stabilized. The novel pump phase stabilization technique using WPD is presented and compared to the more common dither locking technique in Chap. 7.

### 6.3.3. Rear lock of the OPO with conventional PDH-lock

Stabilizing the OPO with the generated squeezed light field via polarization-balanced homodyne locking makes it impossible to use the squeezed light field for downstream experiments. It is therefore necessary to implement an alternative locking scheme from the rear side of the OPO, leaving the outcoupled squeezed light field undisturbed. Since the cavity mirrors remained in place (the flat front mirror is still the in-/out-coupler with  $R_{\text{in}} = 90\%$  and the flat rear mirror is highly reflective with  $R > 99.9\%$ ) a possible locking light field from the rear perceives the cavity as undercoupled [FS10] (in this case  $R_{\text{rear}} > 99.9\% > 90\% = R_{\text{in}}$ , see also 4.1.2). The resulting phase shift of the intracavity field is too small for an appropriate error signal to apply polarization-based homodyne locking from the rear side of the OPO. For this reason a conventional PDH-stabilization scheme was implemented.

### 6.3. Frequency stabilizing a cavity for parametric down conversion

#### OPO rear PDH locking with counterpropagating intracavity field

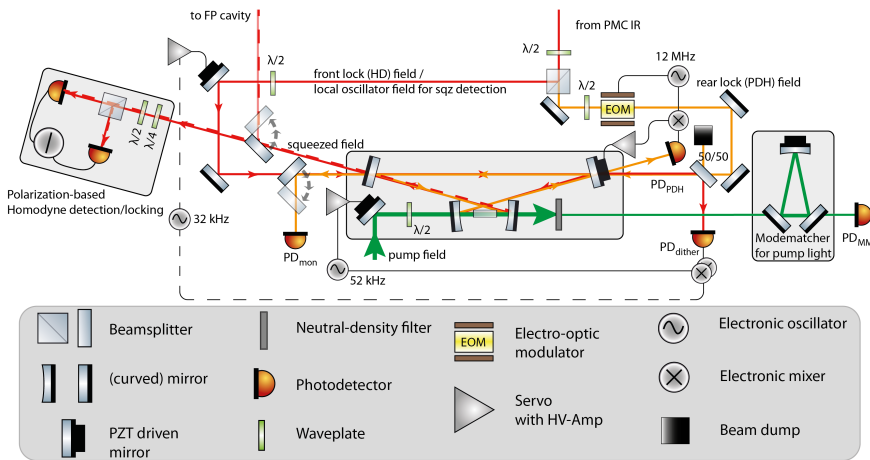


**Figure 6.8.:** The experimental setup of the OPO rear locking scheme to utilize the generated squeezed light field. The infrared light field is split into the front lock field (with homodyne detection, see Sec. 6.1.4) and the rear lock field (with PDH, see Sec. 6.1.2). The rear lock field couples with a plane incident angle at the rear mirror into the cavity resulting in a counterpropagating intracavity field with respect to the generated squeezed light field. The former front lock light field acts in this case as the LO for the homodyne detection of the resulting squeezed light.

In the first setup (see Fig. 6.8) the locking beam is coupled straight into the rear mirror of the OPO at a plane incident angle and is counterpropagating to the pump field to prevent any impact of the generated squeezing by a copropagating light field inside the nonlinear crystal. To investigate the influence of the direction of the intracavity field it is compared to a second rear locking setup with a copropagating intracavity beam (see Fig. 6.9). However, the copropagating field is necessary in order to generate an error signal to lock the pump field phase to the cavity due to its interaction with the pump field. Furthermore, the copropagating control field is needed to lock the squeezed light field to the downstream setup for squeezed-light enhanced metrology (see Chap. 8). By omission of the front lock its light field could still act as a copropagating control field. The pump phase is stabilized via dither lock by detection of the transmitted intracavity field on  $PD_{dither}$  with demodulation<sup>5</sup> at the dither frequency

<sup>5</sup>For the demodulation a coaxial frequency mixer *ZAD-3+* from Mini-Circuits was used.

## 6. Generation of squeezed states

---

$f_{\text{dither}} = 52 \text{ kHz}$ . The frequency stabilization of the OPO cavity is accomplished by the PDH-locking scheme. This includes the detection of the beat between the directly reflected sidebands imprinted by the EOM<sup>6</sup> and the cavity field on  $\text{PD}_{\text{PDH}}$  that is demodulated with the sideband frequency  $f_{\text{PDH}} = 12 \text{ MHz}$  by the mixer of the photodetector<sup>7</sup>. If the front lock field is entirely in p-polarization, it is completely reflected at the cavity which is resonant for s-polarization. Thus, the field acts as a LO for a measurement of the reduced variance in the phase quadrature of the OPO cavity via homodyne detection. Though this LO field is perfectly overlapped with the desired squeezed field there is no defined phase relation between them. This is why an additional stabilization scheme must be applied to ensure a fixed phase relation. Either a further dither lock (we chose a modulation frequency of  $f_{\text{LO}} = 32 \text{ kHz}$ ) or the utilization of the interference signal at the polarization-based homodyne detector is suitable. For the sake of convenience the given setup for polarization-based homodyne detection was used.

---

<sup>6</sup>A broadband phase modulator 4004 from Newport was used.

<sup>7</sup>The photodetector was an onboard combination of photodetector and plug-in frequency mixer (*TUF-3+* from Mini-Circuits), made by Dr. Vahlbruch.

### 6.3. Frequency stabilizing a cavity for parametric down conversion

#### OPO rear PDH locking with copropagating intracavity field

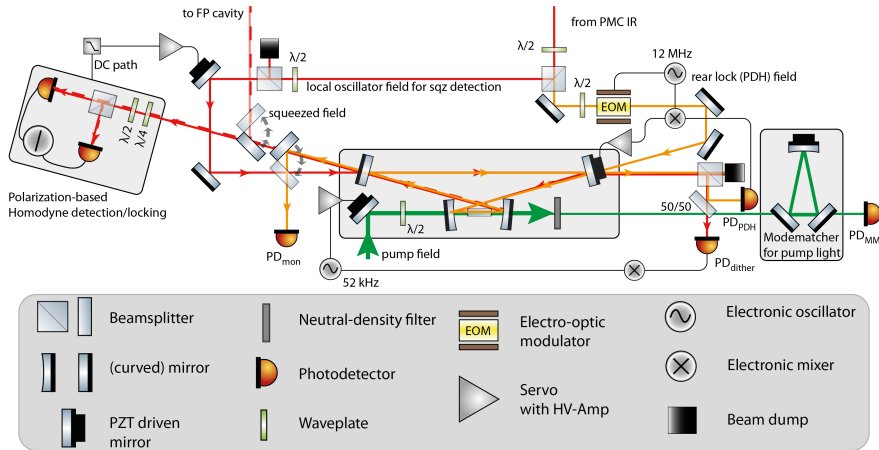


**Figure 6.9.:** Experimental setup of OPO frequency stabilization with changed incident angle of the incoupling rear field. This leads to a copropagating intracavity field that is necessary in order to generate an error signal for locking the pump field phase to the cavity due to its interaction with the pump field. Furthermore, the copropagating control field is needed to lock the squeezed light field to the downstream setup for squeezed-light enhanced metrology (see Chap. 8).

Changing the incident angle of the seed field for the PDH rear lock scheme results in a copropagating intracavity field (see Fig. 6.9). This field interacts with the pump light field and creates a suitable error signal for pump phase stabilization. For this purpose the light field is split up on a power beamsplitter into beams to  $PD_{PDH}$  for the cavity stabilization via PDH locking and to  $PD_{dither}$  for the pump phase stabilization via dither locking.

There is no degradation of the generated squeezed field by the copropagating intracavity field (see Sec. 2.4.6), as long as the final homodyne detection is able to separate the coherent and squeezed fields with a strong LO. Since the p-polarized front field acts as the LO a PBS is integrated for filtering purposes to prevent leakage of s-polarization in this LO field from entering the cavity and disturbing the s-polarized error signals for stabilizing the cavity and the pump phase.

### 6.4. Comparison of OPO frequency stabilization techniques

The advantage of the polarization-based homodyne locking scheme is that there is no spatial separation of signal and LO due to the fact that they are orthogonal linear polarizations in one light field. The homodyne detector is used to measure the squeezed output variance in the phase quadrature, while due to the fixed phase between s- and p-polarization the cavity is frequency locked simultaneously. On the other hand there is a drawback due to the restriction to only measuring the phase quadrature variance, and the fact that one has no exclusive access to the LO. Having signal and LO (respectively s-polarization and p-polarization) in a certain ratio to lock the OPO and allow for simultaneous readout of the squeezed output, the homodyne visibility can be degraded by mode mismatch in the cavity or point defects on the mirrors and beamsplitters for the polarization distribution.

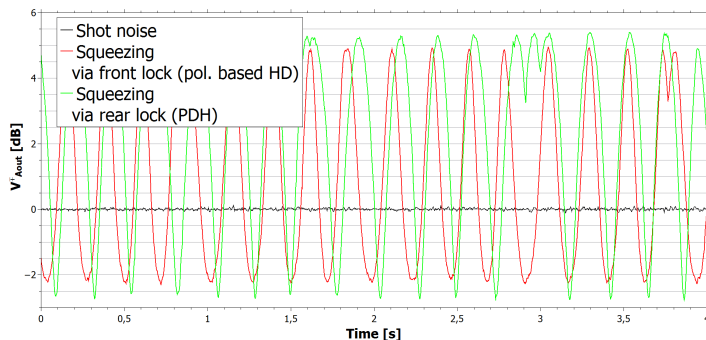


**Figure 6.10.:** Comparison between front and rear lock in our experimental setup (see Fig. 6.8). Due to the copropagating beams the variance of the squeezed light field has 6–10% of additional losses in the front locking setup as opposed to the rear locking setup with plane incident angle.

Fig. 6.10 shows a zero span measurement of the squeezing generated by the OPO cavity which was stabilized with the two locking schemes. Since it was a zero span measurement at 197.4 MHz (corresponding to the first FSR), the swept pump phase generates a sinusoidal signal for both locking schemes oscillating between the maximum of squeezing and antisqueezing by sweeping the phase of the pump field with respect to the OPO cavity phase. Without the pump field the detected shot noise level determines the 0 dB base level which is reduced by the squeezed field and increased by the antisqueezed field depending on

## 6.4. Comparison of OPO frequency stabilization techniques

the corresponding phase of the pump field.

**Table 6.2.:** Comparison of squeezing values.

Lock	Squeezing	Antisqueezing
Front	-2.35 dB	5.02 dB
	Initial squeezing	$\pm 7.37$ dB
Rear	-2.80 dB	5.52 dB
	Initial squeezing	$\pm 8.32$ dB

Compared to the rear lock with a counterpropagating light field the polarization-based homodyne lock with the copropagating field causes 6–10% more losses. Nevertheless, a copropagating beam is necessary in order to lock the pump phase for squeezed-state generation and to phase lock it for further experiments as well (see Sec. 8.1).





# 7

## Chapter 7

# Demonstration of weak pump depletion phase locking

The generated squeezed states of light demonstrated in this work could offer quantum noise reduction in interferometric measurements or squeezed-light enhanced high-precision metrology. For these applications the squeeze angle must be controlled by stabilizing the pump phase to the intracavity phase. If the pump field is in phase with the intracavity field, it permits the highest efficiency for generating squeezed states. Accordingly, an additional stabilization scheme for the pump phase has to be considered. Commonly used stabilization schemes (see Sec. 6.1) are using either modulation sidebands (dither locking, PDH technique) [HKEB06, DHK<sup>+</sup>83], modulation-free slight misalignment of beams (tilt locking) [RSS<sup>+</sup>02] and polarization (Hänsch-Couillaud locking, homodyne locking) [HC80, HPJH09]. The necessary slight misalignments of some modulation-free schemes are direct loss channels for squeezed light. So there is a trade-off between additional losses and the capacity to stabilize a system.

In this chapter an effect called *weak pump depletion* (WPD) is investigated regarding its usefulness for locking the pump field phase to the intracavity field of a nonclassical light source. WPD is an omnipresent but generally neglected side effect of the interaction between the seed and pump fields in the nonlinear medium and automatically contains information about the phase difference between the two beams (see Sec. 5.2). The effect of *full pump depletion* can be used for arbitrarily strong entanglement between the two light fields [GBML06].

## 7. Demonstration of weak pump depletion phase locking

---

We show here that exploiting this unavoidable interaction it is possible to produce and detect a fully stabilized squeezed vacuum state without degrading the squeezed output field, merely by phase-sensitive detection of the transmitted pump field. We term this novel phase-locking scheme *weak pump depletion locking* (WPD locking). As shown in our corresponding publication [DSW<sup>+</sup>15] the phase difference between the seed and pump fields is imprinted on the pump and seed light by the nonlinear interaction in the crystal and can be read out without disturbing the squeezed output. A comparable approach to lock the phase of a squeezed vacuum state with an omnipresent effect is using the asymmetry in the quadrature variances due to quantum noise [MMG<sup>+</sup>05].

In the first part of this chapter the theory of WPD is derived by extending the cavity dynamics presented in Sec. 5.2 with the interacting weak depleted pump field  $\hat{b}_{\text{in}}$ , and investigating the influence of WPD on the output of the fundamental and the pump field with regard to locking the pump phase. There are two different schemes of pump phase locking used in the experimental setup and presented in this thesis: WPD locking using the green pump field and dither locking utilizing the fundamental field. In the second part of this chapter a detailed description is given and the two locking techniques are compared in terms of efficiency.

In the experimental setup, shown in Fig. 7.2, the input of the OPO is 0.55 mW of 1064 nm and it is pumped with 67.8 mW of 532 nm laser light to observe squeezing levels of 1.96 dB, with an antisqueezing level of 3.78 dB. This new locking technique allows the first experimental realization of a pump-phase lock by read-out of the phase information pre-existing in the pump field. As a result there is no degradation of the detected squeezed states.

### 7.1. Theory of weak pump depletion

As the nonlinear interaction in an OPO cavity is comparatively weak the pump field is typically assumed to be undepleted and hence constant. In this section, the ever-present existence of pump field fluctuations due to WPD is shown and the influence of WPD – both on the error signal and on the variance of the (anti)squeezed output – is calculated. The intracavity dynamics for this OPO, described in Sec. 5.2, are extended to examine the influence of the WPD.

## 7.1.1. Cavity dynamics

The Hamiltonian describing the second-order nonlinear interaction of the cavity modes of the OPO (see Fig. 5.3) at the fundamental frequency (represented by the annihilation and creation operators  $\hat{a}$  and  $\hat{a}^\dagger$ , respectively) and the second-harmonic frequency ( $\hat{b}$  and  $\hat{b}^\dagger$ ) is given by [WM07]:

$$\hat{H} = i\hbar\chi_c \left( \hat{b}^\dagger \hat{a}^2 - \hat{a}^\dagger \hat{b} \right), \quad (7.1)$$

where  $\chi_c$  is the nonlinear coupling parameter being proportional to the second-order susceptibility term  $\chi^{(2)}$  and the amplitude of the pump field. Having a weakly depleted pump field the substitution of  $\hat{q} = 2\chi_c \cdot \hat{b}$  (see Eq. (5.12)) is not valid. Using the Liouville-von Neumann equation [Sch13] and taking losses into account the resulting equations of motion for the intracavity fields are (according to [BR04]):

$$\dot{\hat{a}} = -2\chi_c \hat{a}^\dagger \hat{b} - (\kappa_a + i\Delta_a) \hat{a} + \sqrt{2\kappa_A} \hat{A}_{\text{in}} + \sqrt{2\kappa_{1,A}} \hat{A}_1, \quad (7.2a)$$

$$\dot{\hat{b}} = \chi_c \hat{a}^2 - (\kappa_b + i\Delta_b) \hat{b} + \sqrt{2\kappa_B} \hat{B}_{\text{in}} + \sqrt{2\kappa_{1,B}} \hat{B}_1. \quad (7.2b)$$

All parameters are described in Sec. 5.2.

The phase angle  $\theta_b$  represents the phase difference between the input pump field ( $\beta_{\text{in}}$ ) and the input cavity field ( $2\alpha_{\text{in}}$ ). Without loss of generality we define the input cavity field  $\alpha_{\text{in}}$  as the reference such that  $\beta_{\text{in}} = |\beta_{\text{in}}| \exp(i\theta_b)$ . For simplicity we will drop the ‘hat formalism’ indicating operators for the following calculations.

As the cavity is only resonant for 1064 nm (and not for 532 nm) we can assume  $\kappa_a \ll \kappa_b$ , so the pump field interacts with the cavity on a much shorter time scale than the fundamental field. This adiabatic elimination of the pump field allows the consideration that  $\hat{b}$  is in steady state. Further we only keep terms to first order in  $\delta$  and to second order in  $\chi_c$ , and we consider without loss of generality that  $\alpha_{\text{in}}$  is real ( $\alpha_{\text{in}}^* = \alpha_{\text{in}}$ ). The steady state intracavity field amplitudes can then be written as:

$$\alpha = \frac{\sqrt{2\kappa_A} \alpha_{\text{in}} (\kappa_a - \chi e^{i\theta_b})}{\kappa_a^2 - |\chi|^2}, \quad (7.3a)$$

$$\beta = \frac{\sqrt{2\kappa_B} |\beta_{\text{in}}|}{\kappa_B} + \frac{\kappa_A \alpha_{\text{in}}^2 |\chi|}{\sqrt{2\kappa_B} |\beta_{\text{in}}| (\kappa_a^2 + |\chi|^2)} e^{-i\theta_b}. \quad (7.3b)$$

In Eqs. (7.3a) and (7.3b) we have introduced the nonlinearity factor  $\chi$  by the substitution  $\chi(\theta_b) = 2\chi_c \sqrt{\frac{2}{\kappa_b}} \beta_{\text{in}} \exp(i\theta_b)$ .  $|\chi|$  can be calculated

## 7. Demonstration of weak pump depletion phase locking

---

from the value of maximum gain (initial squeezing), which in turn can be calculated from a pair of measured squeezing and antisqueezing values (see Sec. A.1).

The outcoupled light fields  $\alpha_{\text{out}}$  and  $\beta_{\text{out}}$  can be calculated using the boundary conditions  $\alpha_{\text{out}} = \sqrt{2\kappa_A}\alpha - \alpha_{\text{in}}$  and  $\beta_{\text{out}} = \sqrt{2\kappa_B}\beta - \beta_{\text{in}}$  (and writing the field quadratures as  $X_q^+ = (q+q^*)$  and  $X_q^- = i(q-q^*)$  for  $q = \alpha_{\text{out}}, \beta_{\text{out}}$ ) [BR04]:

$$X_{\alpha_{\text{out}}}^+ = \frac{2\alpha_{\text{in}}(2\kappa_a\kappa_A - \kappa_a^2 + |\chi|^2)}{\kappa_a^2 - |\chi|^2} - \boxed{\frac{4\alpha_{\text{in}}\kappa_A|\chi|}{\kappa_a^2 - |\chi|^2} \cos(\theta_b)}, \quad (7.4a)$$

$$X_{\alpha_{\text{out}}}^- = \frac{4\kappa_A\alpha_{\text{in}}|\chi|}{\kappa_a^2 - |\chi|^2} \sin(\theta_b). \quad (7.4b)$$

Eqs. (7.4a) and (7.4b) show that  $X_{\alpha_{\text{out}}}^\pm$  is a function of both  $\alpha_{\text{in}}$  and  $|\chi|$ , which in turn is a function of  $|\beta_{\text{in}}|$ . The influence of the pump field and the relative phase  $\theta_b$  between the pump and seed beams appears in the second term of the expression for  $X_{\alpha_{\text{out}}}^+$ , indicated by the box. This signal can be used as an error signal for locking purposes (see Sec. 7.2.1). Therefore, the variance of the amplitude quadrature of the fundamental  $X_{\alpha_{\text{out}}}^+$  is processed in a dither modulation scheme to lock the pump-seed phase angle to the maximum of the transmitted fundamental field (see Sec. 6.1.3). This angle determines the quadrature of squeezing: locking it will additionally lock the quadrature angle of squeezing illustrated in the quadrature variance in Sec. 7.1.2. In contrast, the effect of the nonlinear interaction between pump and seed on the output pump field is typically ignored (in the so-called “no pump depletion” limit). The effect is indeed very small, however, it does not vanish and can be seen in the output field quadratures of the pump field:

$$X_{\beta_{\text{out}}}^+ = X_{\beta_{\text{in}}}^+ + \frac{2\alpha_{\text{in}}^2\kappa_A|\chi|}{|\beta_{\text{in}}|\kappa_a^2} \cos(\theta_b), \quad (7.5a)$$

$$X_{\beta_{\text{out}}}^- = X_{\beta_{\text{in}}}^- \boxed{\frac{2\alpha_{\text{in}}^2|\chi|\kappa_A}{|\beta_{\text{in}}|\kappa_a^2} \sin(\theta_b)}. \quad (7.5b)$$

Eqs. (7.5a) and (7.5b) are also functions of  $\alpha_{\text{in}}$ ,  $\beta_{\text{in}}$ , and their phase relationship. Therefore there will be small fluctuations around the average pump field amplitude caused by the nonlinear interaction with the seed field. Usually neglected, this term shows a sinusoidal dependence on the pump-seed phase relationship  $\theta_b$ . Under certain conditions (to be examined below) the boxed term of Eq. (7.5b) can be

used as an alternative error signal to lock the pump-seed phase angle as well.

Polarization-based homodyne detection (see Sec. 6.1.4) of the signal in Eq. (7.5b) will result in a large DC field that varies as a function of the pump-seed phase angle  $\theta_b$ . In the case of a singly-resonant cavity the s-polarized pump field (see Eq. (7.5b)) containing the WPD signal is mixed by a quarter-wave-plate and a PBS with the amount of the pump field in p-polarization that does not interact with the crystal. This can be treated as a general balanced homodyne detection with signal  $\beta_{\text{out}}$  and LO  $\beta_{\text{LO}} = |\beta_{\text{p,in}}| \exp(i(\theta_b + \gamma))$ . The difference in the two detected intensities is

$$I_{\text{lock}} = \frac{2\alpha_{\text{in}}^2 |\chi| \kappa_A}{|\beta_{\text{in}}| \kappa_a^2} |\beta_{\text{p,in}}| \sin(\theta_b + \gamma), \quad (7.6)$$

where  $\gamma$  is the homodyne measurement angle. It has a fixed value of  $\gamma = \pi/2$  due to the polarization-based homodyne detection scheme which is described in Sec. 3.4.

### 7.1.2. The effect of WPD on squeezing and antisqueezing

The results for the fluctuating terms (see Sec. 4.2.2 for an empty cavity) are found by moving to the Fourier frequency domain

$$\text{FT}[d\delta a(t)/dt] = -i\omega \text{FT}[\delta a](\omega).$$

The variance of  $\delta \hat{X}_{A_{\text{out}}}^{\pm}$  gives the values for squeezing and antisqueezing in the amplitude or phase quadrature, respectively. We use the common definition for quadrature variance:

$$V^{\pm} \equiv \langle |\delta \hat{X}^{\pm}|^2 \rangle - \langle |\delta \hat{X}^{\pm}| \rangle^2,$$

where  $\delta \hat{X}_A^+ = \delta \hat{A} + \delta \hat{A}^\dagger$  and  $\delta \hat{X}^- = i(\delta \hat{A} - \delta \hat{A}^\dagger)$ . As we are only interested in the variance of the (squeezed) output at the fundamental frequency we look for the phase and amplitude quadrature expressions for the driving seed field operator ( $\delta \hat{A}_{\text{in}}$ ) at different pump-seed phase angles  $\theta_b$ :

$$V_{A_{\text{out}}}^+(\theta_b = 0) = V_{A_{\text{in}}}^+ \frac{(|\chi| + \kappa_a - 2\kappa_A)^2}{(\kappa_a + |\chi|)^2} + \boxed{V_{B_{\text{in}}}^+ \frac{4\alpha_{\text{in}}^2 \kappa_A^2 |\chi|^2}{|\beta_{\text{in}}|^2 \kappa_a^2 (\kappa_a + |\chi|)^2}} + V_{A_1}^+ \frac{4\kappa_{1,A} \kappa_A}{(\kappa_a + |\chi|)^2}, \quad (7.7)$$

## 7. Demonstration of weak pump depletion phase locking

---

$$\begin{aligned}
 V_{A_{\text{out}}}^- (\theta_b = 0) &= V_{A_{\text{in}}}^- \frac{(|\chi| - \kappa_a + 2\kappa_A)^2}{(\kappa_a - |\chi|)^2} + \boxed{V_{B_{\text{in}}}^- \frac{4\alpha_{\text{in}}^2 \kappa_A^2 |\chi|^2}{|\beta_{\text{in}}|^2 \kappa_a^2 (\kappa_a - |\chi|)^2}} \\
 &+ V_{A_1}^- \frac{4\kappa_{1,A} \kappa_A}{(\kappa_a - |\chi|)^2}.
 \end{aligned} \tag{7.8}$$

The boxed terms show the miniscule influence of the pump field phase on the fundamental field ( $\alpha_{\text{in}} \ll |\beta_{\text{in}}|$ ). Calculations show that there should be no degradation of the detected quadrature variances if we use the highlighted expression in Eq. (7.5b) as an error signal for pump phase locking.

By neglecting intracavity losses ( $\kappa_{1,A} = 0$  and  $\kappa_A = \kappa_a$ ) and the influence of the pump field, Eqs. (7.7) and (7.8) turn into the variance of the initial squeezing:

$$V_{\text{init}}^\pm = V_{A_{\text{in}}}^\pm \frac{(|\chi| \mp \kappa_a)^2}{(\kappa_a \pm |\chi|)^2}. \tag{7.9}$$

### 7.1.3. Gain and losses

We are interested in the nonlinearity factor  $\chi$  related to the maximum amount of (anti)squeezing. To calculate the initial (anti)squeezing values  $V_{\text{init}}^\pm$  we assume that the measured values  $V_{\text{det}}^\pm$  experience identical optical loss  $\eta_{\text{tot}}$ . The incoupling loss can be treated like an open beam-splitter port. In this case the variance, including losses, becomes (see Eq. (3.23)):

$$V_{\text{det}}^\pm = \eta_{\text{tot}} V_{\text{init}}^\pm + (1 - \eta_{\text{tot}}). \tag{7.10}$$

For this reason we equate Eq. (7.10) for  $V_{\text{det}}^+$  with  $V_{\text{init}}^+$  and  $V_{\text{det}}^-$  with  $-V_{\text{init}}^-$  for the same loss value  $\eta_{\text{tot}}$  and obtain

$$V_{\text{init}}^- = -V_{\text{init}}^+ = \frac{V_{\text{det}}^- - 1}{V_{\text{det}}^+ - 1}. \tag{7.11}$$

With this result the total optical loss factor  $\eta_{\text{tot}} = 0.5$  and the value for initial squeezing  $V_{\text{init}}^\pm = \pm 5.82$  dB are calculated. Fig. 7.1 shows a plot of Eq. (7.10) for  $V_{\text{init}}^\pm = \pm 5.82$  dB over the loss factor  $\eta_{\text{tot}}$ .

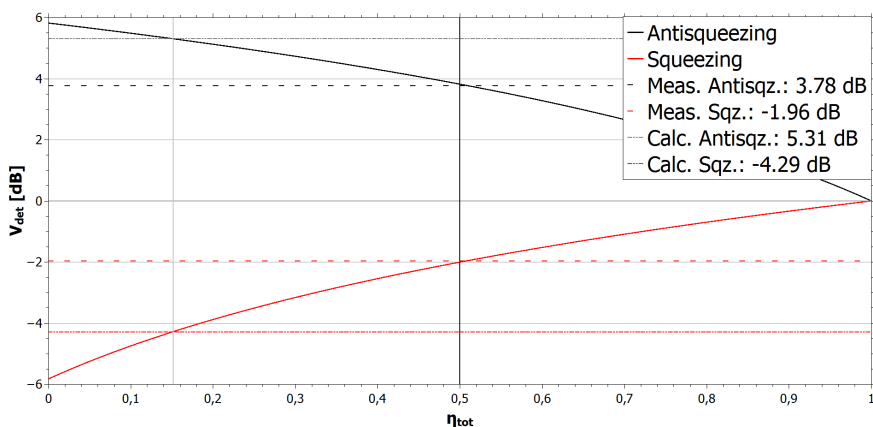


**Figure 7.1.:** Plot of detected variance in the phase quadrature (Eq. (7.10)) as a function of total loss  $\eta_{tot}$  with the initial squeezing value  $V_{init}^{\pm} = \pm 5.82$  dB.

The theoretical characterization of the OPO behavior in Eqs. (7.7) and (7.8) includes intracavity losses via the decay rate of the intracavity field  $\kappa_a$  or  $\kappa_A$  for the input field, given by the escape efficiency  $\eta_{esc}$ . Different loss factors degrade the initial squeezing to arrive at the outcoupled squeezing and finally the measured squeezing at the homodyne detector:

$$V_{init}^{\pm} \xrightarrow{\eta_{esc}} V_{A_{out}}^{\pm} \xrightarrow{\eta_{prop}\eta_h\eta_{qe}} V_{det}^{\pm}.$$

This chain of reasoning shows the connection between all loss terms and the different quadrature variances. With the knowledge of each loss term (see Sec. 7.3.1) of  $\eta_{tot} = \eta_{esc}\eta_{prop}\eta_h\eta_{qe}$  and the relation of  $V_{det}^{\pm}$  and  $V_{A_{out}}^{\pm}$  (see Eqs. (7.10) and (7.11)) the theoretical output  $V_{A_{out}}^{\pm}$  can be compared with the experimental data  $V_{det}^{\pm}$  in Sec. 7.3.1 (see Fig. 7.7).

## 7.2. Experimental realization

Fig. 7.2 shows a simplified schematic of the experimental setup. Mode matching optics are omitted for clarity. The laser source was a  $\lambda = 1064$  nm Nd:YAG non-planar ring oscillator (NPRO) (Innolight Mephisto). To generate the pump light at  $\lambda = 532$  nm a linear hemilithic SHG with a 6.5 mm LiNbO<sub>3</sub>-crystal (see Sec. 6.2) was used and was frequency stabilized by polarization-based homodyne locking [HPJH09]. The OPO cavity (described in Sec. 6.3) was also frequency

## 7. Demonstration of weak pump depletion phase locking

locked with the polarization-based homodyne locking scheme which allows detection of (anti)squeezing in the phase quadrature variance at the same time (via the fixed homodyne measurement angle  $\gamma = \pi/2$ , see Eq. (7.6)). The characteristic parameters of the cavity are listed in Table 7.1.

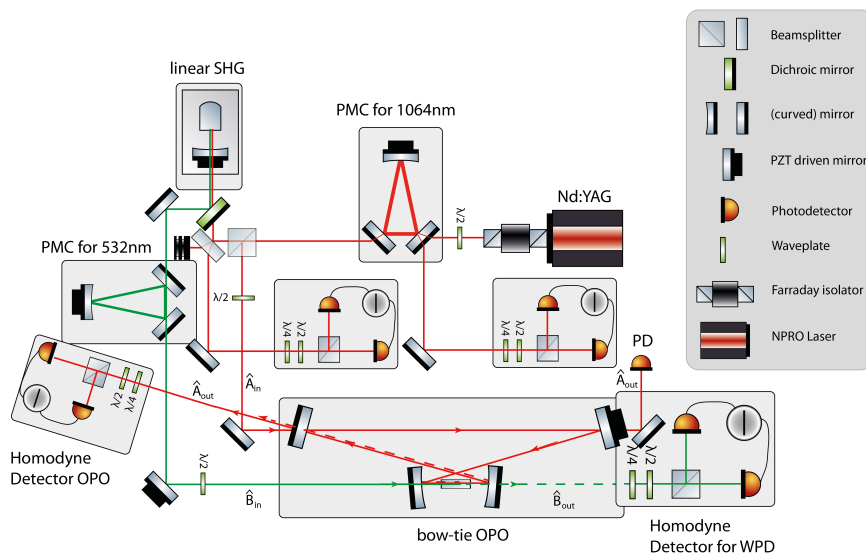


**Figure 7.2.:** Schematic overview of the experimental setup. The infrared light is sent through a mode cleaner (PMC) for spatial mode filtering and power stabilization and then frequency doubled in a linear SHG cavity. The generated green pump light is prepared with a similar mode cleaning cavity and sent to the bow-tie OPO cavity. For locking purposes the infrared light is coupled into the OPO cavity as well. The *homodyne detector OPO* is responsible for locking the OPO cavity and simultaneously detecting the phase quadrature variance whereas the *homodyne detector WPD* generates the error signal for locking the green pump phase to the OPO cavity using WPD locking.

The OPO locking beam had a power of 9.66 mW with a ratio of 3:100 between the signal (s-polarization) and LO (p-polarization). This slight deviation from the experimental “rule of thumb” of 1:100 for homodyne detection was chosen to guarantee adequate experimental performance. The power of the green pump light was 67.8 mW with s/p-polarization ratio of 100:5 for the interferometric readout. The spectroscopic signal provided a sufficiently stable lock of the pump phase while the amount of effective pump power was as high as possible. Due to the highly sensitive measurement of the WPD locking



signal (Eq. (7.5b)) there is a trade-off between the amount of pump power and attenuation with several neutral density filters to keep the photodiodes operational. By detecting the transmitted green pump light with a homodyne detector its phase could be locked to the cavity. The PZT mirror in the pump beam could be used as a phase actuator and also provided the option of inducing a kHz-modulation for dither-locking [HKEB06] of the pump phase for comparison between the two locking schemes (WPD and dither).

**Table 7.1.:** Overview of the parameters characterizing the OPO.  
The calculation of the parameter  $\chi$  is described in Sec. 7.1.3.

Parameter	Symbol	Value	Unit
Length	$l$	1.52	m
Free spectral range	$f_{\text{FSR}}$	197.4	MHz
Finesse	$\mathfrak{F}$	58	
Linewidth (FWHM)	$\Delta\nu = f_{\text{FSR}}/\mathfrak{F}$	3.9575	MHz
Cavity decay rates (HWHM)	$\kappa_a$	$1.2434 \cdot 10^7$	rad/s
	$\kappa_A$	$1.0686 \cdot 10^7$	rad/s
	$\kappa_{1,A}$	$0.1749 \cdot 10^7$	rad/s
Input power (seed)	$\alpha_{\text{in}}^2$	0.55	mW
		$2.946 \cdot 10^{15}$	Hz
Input power (pump)	$\beta_{\text{in}}^2$	64	mW
		$2.143 \cdot 10^{17}$	Hz
Nonlinearity factor (HWHM)	$ \chi $	$3.45 \cdot 10^6$	rad/s
Initial (anti)squeezing	$V_{\text{init}}^{\pm}$	$\pm 5.82$	dB
Calculated squeezing	$V_{A_{\text{out}}}^-$	-4.29	dB
Calculated antisqueezing	$V_{A_{\text{out}}}^+$	5.31	dB
Detected squeezing	$V_{\text{det}}^-$	-1.96	dB
Detected antisqueezing	$V_{\text{det}}^+$	3.78	dB

### 7.2.1. Error signals

Fig. 7.3 shows the error signal for the WPD lock from Eq. (7.6), and in comparison  $X_{\alpha_{\text{out}}}^+$  from Eq. (7.4a) (the transmitted infrared signal of the OPO which is indicative of the behavior of the green pump light). The intensity of the infrared light ( $X_{\alpha_{\text{out}}}^+$ ) was detected with a single photodetector (red curve in Fig. 7.3) whereas the homodyne detector acted as an interferometer to read out the phase quadrature of the green pump light ( $X_{\beta_{\text{out}}}^-$ ) (black curve in Fig. 7.3).  $X_{\beta_{\text{out}}}^-$  could

## 7. Demonstration of weak pump depletion phase locking

be used as a locking signal to stabilize the pump phase  $\theta_b$ , as its gradient is maximal close to the extrema of the infrared light field exiting the cavity  $X_{\alpha_{out}}^+$  (deviations are due to delays in the phase detection). Compared to the strong mean pump field the fluctuating part is strong enough to yield an adequate *signal-to-noise ratio* (SNR) of  $\approx 12.2$  dB.

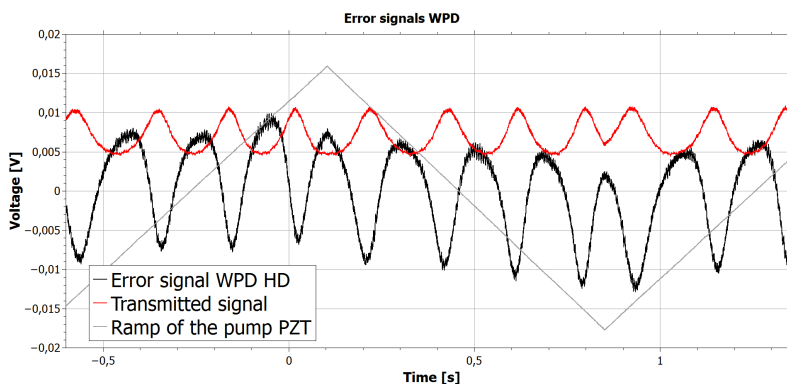


**Figure 7.3.:** Error signal of the transmitted pump light for WPD (black) and transmitted cavity field (red) with swept pump phase (grey) versus time. The slight phase offset gives a strong signal for pump phase stabilization. For purposes of presentation the scaling of the two signals differs. The scaling on the y-axis belongs to the error signal WPD HD. The tiny effect of WPD on the pump phase is low-pass filtered and amplified by the homodyne photodetector electronics.

The asymmetry in the sine-form of the signals can be explained by the theory of homodyne locking the OPO to the infrared light. Due to the sinusoidal sweep of the green pump phase there is (de-)amplification of the infrared intracavity light. For this reason the ratio of directly reflected p-polarization and outcoupled (de-)amplified s-polarization varies, and this sinusoidal signal for locking the OPO is fed back. This feedback in combination with the swept pump phase leads to the deformed sinusoidal error signal with a fitted modulation of  $y = a \cdot \sin^2(\theta) + b \cdot \sin(\theta)$ , see Fig. 7.4.

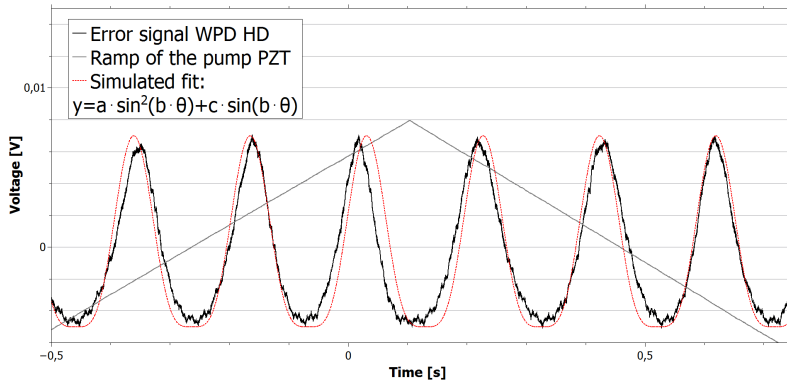


**Figure 7.4.:** Simulation of the error signal of the transmitted pump light for WPD (red) and the measured error signal (black) with swept pump phase (grey) versus time.

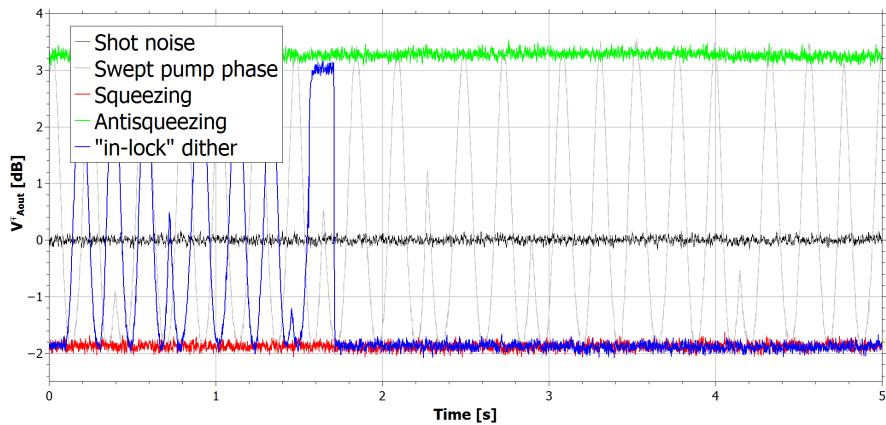
## 7.3. Results

A multichannel oscilloscope<sup>1</sup> is used to display the error signal detected by the homodyne photodetector and for the transmitted light detected by a single photodetector. The variance of the squeezed output at the fundamental frequency is recorded on a signal analyzer<sup>2</sup> while the system is locked. Fig. 7.5 shows the zero span measurements at 197.4 MHz (first FSR) of the variances of the (anti)squeezed output (see Eqs. (7.7) and (7.8)) as a comparison between (a) a conventional dither-locking scheme and (b) homodyne locking using weak pump depletion. The swept variance due to the swept pump phase is stabilized at its minimum by switching on the lock. Both stabilization techniques are sufficient to lock the OPO and what is more the generated levels of squeezing and antisqueezing are the same.

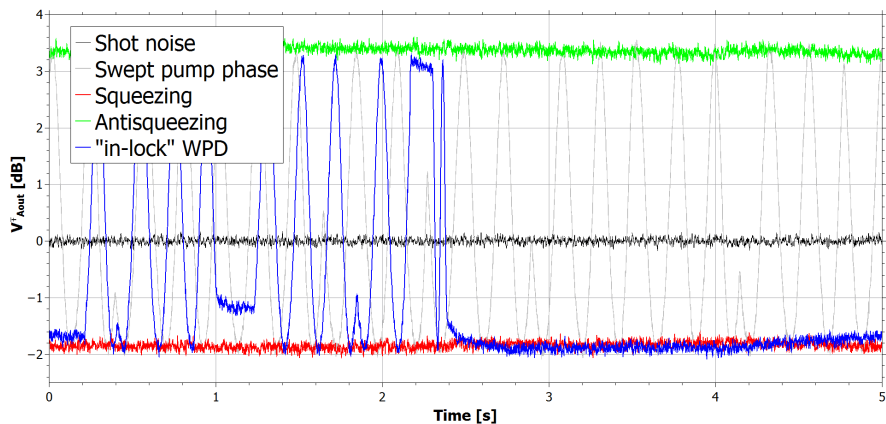
<sup>1</sup>In this setup we used the *MSO X 2014A* oscilloscope from Agilent.

<sup>2</sup>In this setup we used the *MXA N9020A* signal analyzer from Agilent.

## 7. Demonstration of weak pump depletion phase locking



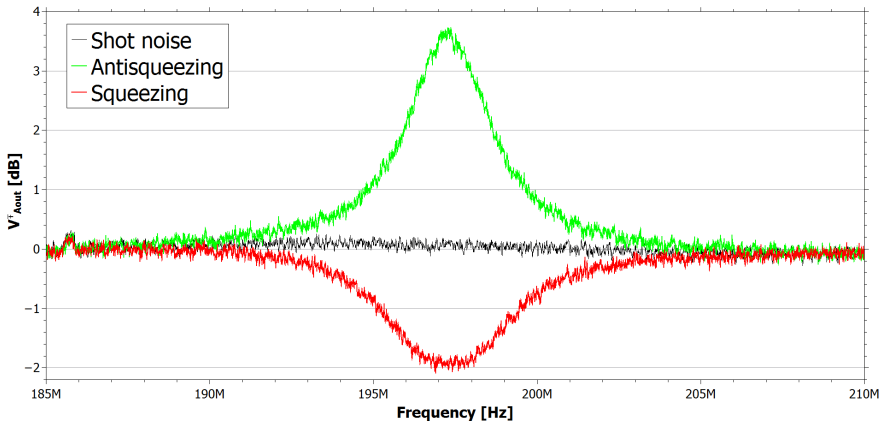
(a) OPO stabilization via dither locking



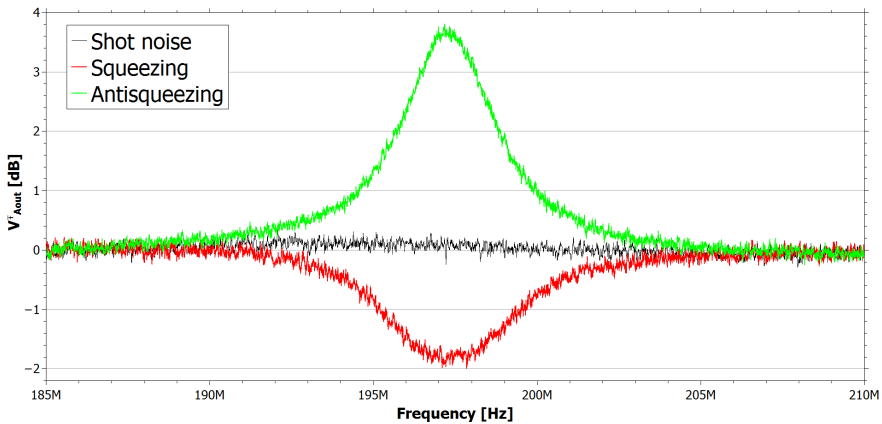
(b) OPO stabilization via WPD locking

**Figure 7.5.:** Zero span measurements of the shot noise levels for the two different locking schemes. (a) shows the dither lock and (b) the WPD lock. The shot noise level without pump is shown in black (with scanned pump phase grey), pump phase locked to antisqueezed phase quadrature in green, pump phase locked to squeezed phase quadrature in red. The blue line illustrates the behavior of switching the scanned pump phase to in-lock.

Fig. 7.6 shows the (anti)squeezing spectra while the pump phase was locked with both techniques, respectively. The observed squeezing levels are 1.96 dB, with an antisqueezing level of 3.78 dB for both stabilization schemes. So there is no degradation of the detected squeezed states by using the effect of WPD for locking purposes.



(a) OPO stabilization via dither locking



(b) OPO stabilization via WPD locking

**Figure 7.6.:** Squeezing spectrum around 197.4 MHz (first FSR) with squeezing level (red) and antisqueezing level (green) versus scanned frequency. (a) shows the dither lock and (b) the WPD lock. The spectrum analyzer settings are: 1.5 MHz resolution bandwidth and 91 Hz video bandwidth with a sweep time of 1.8 s and an internal attenuation of 6 dB. The averaging factor is 10. The noise levels are normalized to the shot noise (black).

The comparison between the measurements shows that the WPD and dither locks result in the same squeezing levels for the identical setup. This experimental result is in excellent agreement with the predicted parameters (shown in Fig. 7.7), derived by Eqs. (7.7) and (7.8).

## 7. Demonstration of weak pump depletion phase locking

### 7.3.1. Comparison between theory and experiment

To demonstrate the validity of the developed theoretical model the calculated parameters are compared to the measurements. All necessary parameters for the setup are given in Table 7.1.

Fig. 7.7 makes use of Eq. (7.10) to relate the calculated values for squeezing and antisqueezing from Eqs. (7.7) and (7.8) with the measured values and shows a plot of the detected variance  $V_{\text{det}}^{\pm}$  over the pump power. It is obvious that our novel WPD-lock technique does not degrade the values for squeezing and antisqueezing.

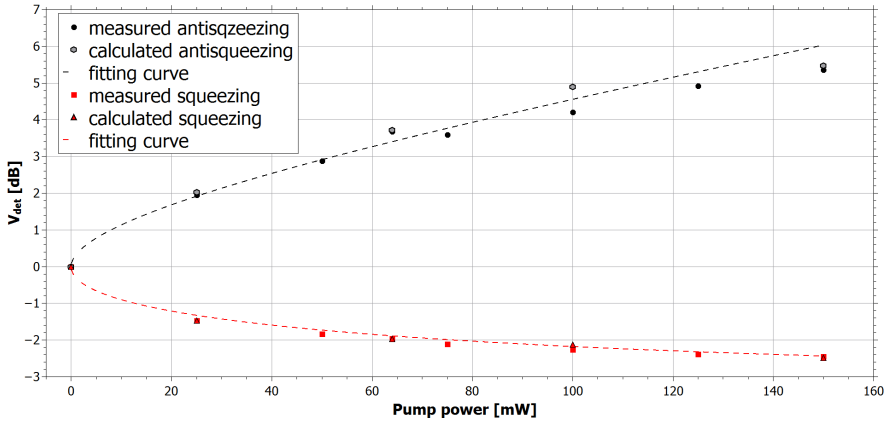


**Figure 7.7.:** Plot of the pump power over the detected (anti)squeezing levels which are also calculated by the formula for outcoupled (anti)squeezing  $V_{A_{\text{out}}}^{\pm}$  (see Eqs. (7.7) and (7.8)). The loss factor of  $\eta_{\text{prop}}\eta_{\text{h}}\eta_{\text{qe}}$  is taken into account (Eq. (7.10)).

Considering the losses (see Sec. 3.5), these results determine that the propagation efficiency is  $\eta_{\text{prop}} = 0.92$ , the homodyne visibility (or mismatch efficiency due to mismatches of the TEM00-modes in orthogonal polarizations)  $\eta_{\text{h}} = \text{VIS}^2 = ((1 - 0.11)/(1 + 0.11))^2 = 0.64$ , and the quantum efficiency of the photodiodes  $\eta_{\text{qe}} = 0.98$ . The OPO escape efficiency  $\eta_{\text{esc}}$  is the ratio of the transmittance  $T$  of the input/output coupler and the total decay of the intracavity field due to intracavity losses  $L$  and the mirror transmittance  $T$ :  $\eta_{\text{esc}} = T_{\text{mirror}}/(T_{\text{mirror}} + L) = 0.1/(0.1 + 0.018) = 0.85$ , where the intracavity losses  $L$  are recalculated with [SH98] of  $\kappa_a$  inferred from the measurement of the linewidth of the lossy cavity. The initial squeezing level in the OPO with 64 mW pump power can be calculated as  $V_{\pm} = \pm 5.82$  dB and the total losses are  $\eta_{\text{tot}} = 0.5$  (see Fig. 7.1).

## **7.4. Conclusion**

With the experimental setup described in this chapter a squeezed light source was fully stabilized using a new pump phase stabilization technique (WPD locking) without degradation of the outcoupled squeezed light field. To lock the pump phase to the OPO cavity the usually neglected effect of the interaction of the seed and pump beams in the nonlinear medium for squeezing generation called weak pump depletion was used. The theoretical investigation shows that the effect of this interaction can be detected in every possible outcoupling port of the cavity. By using WPD for generating an error signal for locking the detected squeezed states experience no degradation. This gives a new option for a modulation-free stabilization of the phase angle between the pump field and the seed field.





# 8

## Chapter 8

# High-precision metrology enhanced with squeezed light

The sensitivity in phase spectroscopy is in general limited by the ratio of the power of the detected signal of interest to the power of the noise (the signal-to-noise-ratio, or SNR). One can increase the SNR either by increasing the signal or by decreasing the noise. If the desired signal (e.g. the interference signal in a GWD due to the fractional length change induced by a gravitational wave) is very small and cannot be enhanced the noise floor must be reduced. At frequencies in the kHz regime the signal detection is dominated by unsuppressed technical noise originating mainly in the electronics for the stabilization schemes and laser noise (e.g. phase noise and intensity noise) and therefore, a (cascaded) phase modulation can shift the signal of interest to a higher frequency regime [FSMA08], resulting in an improved SNR. In a shot-noise limited detection the injection of nonclassical (squeezed) light can increase the instrument's sensitivity [MSM<sup>+</sup>02, AAA<sup>+</sup>13]. The enhancement of high-precision measurements by nonclassical light is not only used in GWDs. For example, high-precision phase measurements via cavity ring-down spectroscopy (CRDS) can benefit from the reduced noise floor by injected squeezed light, as well. Therefore, we propose the idea of an extension of the squeezed-light generation with an OPO (see Chap. 6 and 7) with a cascaded phase modulation for signal up-shifting with additional squeezed-light injection in a FP cavity. Based on the calculated parameters the experimental setup was assembled.

## 8. High-precision metrology enhanced with squeezed light

---

The first part of this chapter presents the theoretical derivation of squeezed states and signals at microwave sideband frequencies (according to higher FSRs of the FP cavity). The FSR (see Eq. 4.10) of the OPO and FP cavity in both cases is  $\sim 200$  MHz. Based on the cavity dynamics described in Chap. 5 the theory of the transmitted cavity field is described at Fourier frequencies far beyond those normally considered [DHHR06] to investigate the signal and cavity dynamics at several FSRs.

The second part of this chapter presents the complete extended experiment to realize a cascaded phase modulation for signal up-shifting with additional squeezed-light injection in a FP cavity. The main task is the implementation and stabilization of the linear FP cavity to show the same FSR as the OPO cavity for squeezed-light generation, and to guarantee that the cascaded phase-modulated signal field and the squeezed light field remain in phase. To provide the detection of the generated squeezed light by the OPO and the enhanced phase detection of the transmitted FP cavity field in the same setup a second high-frequency homodyne detector is needed. Therefore a novel homodyne detector design was developed in collaboration with Dr. Mehmet, adapted from the Australian detector provided by the work group of Prof. Huntington.

By utilizing a homodyne detector with a high-detection bandwidth the high-precision phase measurements are feasible even at higher FSRs of the FP cavity. The detection of such a squeezing comb, shown in App. A.3.1, gives rise to a source of quantum states that can be useful in quantum optics experiments, e.g. in the field of quantum communication.

### 8.1. Squeezed states and signals at sideband frequencies

Unsuppressed technical noise originating in the electronics for the stabilization schemes and laser noise (e.g. phase noise and intensity noise) are dominant at frequencies in the kHz regime and can therefore corrupt possible phase measurements. In order to increase the sensitivity of phase spectroscopy we propose the use of the reduced noise distribution of squeezed states provided by the sub-threshold bow-tie OPO (see Chap. 5). Additionally, a cascaded phase modulation shifts the low-noise signal of interest to higher frequencies (at the modulation frequency), so that it is no longer dominated by technical noise. Ideally, the modulation frequency is equivalent to the FSR of the OPO. Using cavity-enhanced squeezed light at higher FSRs superimposed with the up-shifted signal the SNR can be increased significantly.

#### 8.1.1. Signal modulation in the linear Fabry-Pérot cavity

To realize the detection of the up-shifted signal on the reduced noise floor the squeezed light from the OPO is combined on a beamsplitter with the signal field to couple the combined field into the FP cavity. In our case the signal of interest is a phase modulation at  $\pm\omega_d = 80$  kHz on the signal field corresponding to a cavity length change. To shift this small phase modulation to higher frequencies the signal field is additionally phase-modulated at  $\pm\omega_m = 197.4$  MHz to be simultaneously coincident with the FSRs of the FP cavity and the OPO.

## 8. High-precision metrology enhanced with squeezed light

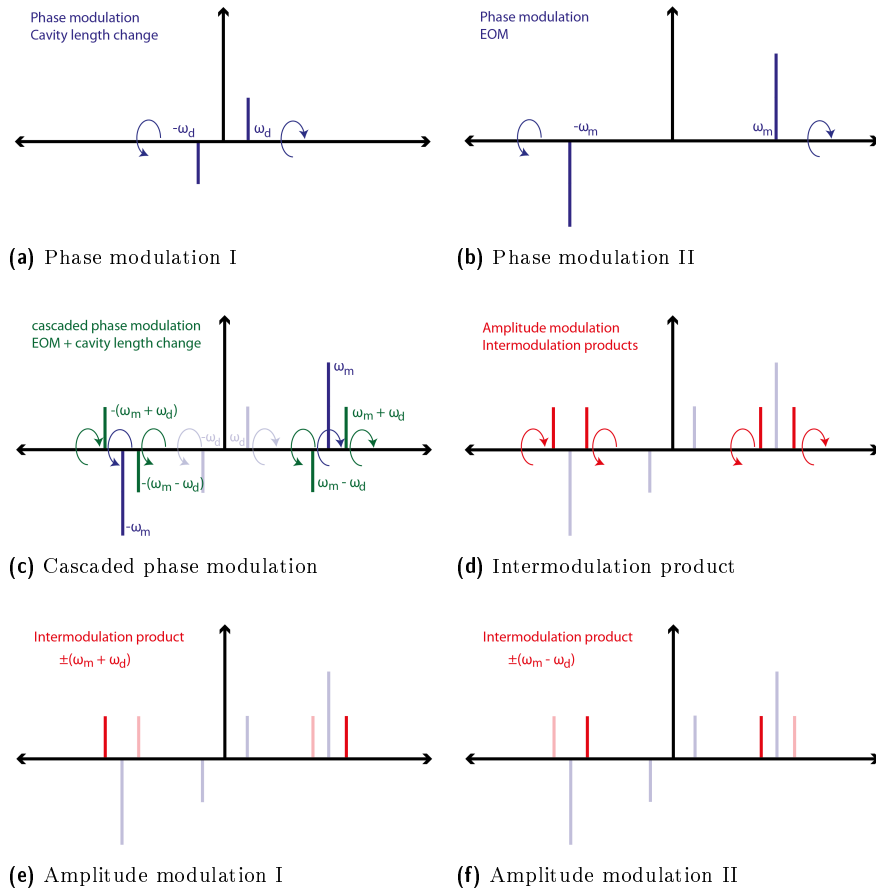


**Figure 8.1.:** Sideband pictures of the process of cascaded signal modulations in the linear Fabry-Pérot cavity. The intermodulation products of two different phase modulations  $\omega_d$  and  $\omega_m$  results in an effective amplitude modulation at  $(\omega_m \pm \omega_d)$ .

As already described in Sec. 2.4.5 the sidebands of a phase-modulated signal are out-of-phase relative to the carrier, such that in the rotating wave picture they face opposite directions when in the plane of the carrier. This leads to an intermodulation product of the cavity length modulation and the incoming phase-modulated field. Fig. 8.1 shows the visualization of this intermodulation product in the sideband picture where the two phase modulations are performed successively. The sideband picture in Fig. 8.1a represents the phase-modulated sidebands corresponding to a small change in the cavity length ( $\pm\omega_d$ ) near the carrier frequency, whereas the phase modulation via the EOM

## 8.1. Squeezed states and signals at sideband frequencies

---

( $\pm\omega_m$ ), shown in Fig. 8.1b, is one FSR away from the carrier. By superimposing these cascaded modulations (see Fig. 8.1c) the sidebands of the cavity length change show up in addition as a new phase modulation (in green) at the former sideband frequencies of the EOM phase modulation (in blue). Considering the sidebands at the first FSR at  $\pm\omega_m$  as a new carrier, its new sidebands due to that intermodulation product can be represented as an amplitude modulation (see Fig. 8.1d) with respect to the original carrier. Upon closer examination of the sidebands it appears to be two separate amplitude modulations at  $\pm(\omega_m + \omega_d)$  and  $\pm(\omega_m - \omega_d)$  appearing in the span around the first FSR (due to the EOM modulation  $\pm\omega_m$ ) to the carrier (bottom row).

In the following we give a mathematical derivation of the amplitude modulation character of a double phase modulation. Starting with a phase modulation from Eq. (2.45) and calculating the sidebands of sidebands [CWBF13], a cascaded phase modulation is explicitly written as

$$E = E_0 e^{i\omega t} e^{im_1 \cos(\omega_d t)} e^{im_2 \cos(\omega_m t)}, \quad (8.1)$$

with the modulation indices  $m_i$ , the carrier frequency  $\omega$  and the two phase modulation frequencies  $\omega_m$  for the EOM and  $\omega_d$  for the cavity length change. With the same derivation as already seen in Sec. 2.5 the cascaded phase modulation may be written as:

$$\begin{aligned} E &= E_0 e^{i(\omega t + m_1 \cos(\omega_d t) + m_2 \cos(\omega_m t))} \\ &= E_0 \left[ e^{i\omega t} + \frac{im_1}{2} e^{i(\omega \pm \omega_d)t} + \frac{im_2}{2} e^{i(\omega \pm \omega_m)t} \right. \\ &\quad \left. - \frac{m_1 m_2}{4} \left( e^{i(\omega + \omega_d \pm \omega_m)t} + e^{i(\omega - \omega_d \pm \omega_m)t} \right) \right]. \end{aligned} \quad (8.2)$$

This form clearly shows the two phase modulations with the modulation indices  $im_1/2$  and  $im_2/2$  and the modulation frequencies  $\omega_d$  and  $\omega_m$ . In addition the intermodulation product is the amplitude modulation (with the factor  $-(m_1 m_2)/4$ ):

$$\begin{aligned} e^{i(\omega \pm (\omega_m \pm \omega_d))t} &= e^{i(\omega + \omega_d + \omega_m)t} + e^{i(\omega + \omega_d - \omega_m)t} \\ &\quad e^{i(\omega - \omega_d + \omega_m)t} + e^{i(\omega - \omega_d - \omega_m)t}, \end{aligned} \quad (8.3)$$

which can be seen in Fig. 8.1 in the lower row.

## 8. High-precision metrology enhanced with squeezed light

### 8.1.2. Theory of squeezing and signals in Fourier space

Considering the variance of the amplitude quadrature (see Sec. 5.2), the fluctuating terms of the intracavity field can be described at Fourier frequencies far beyond those normally considered [DHHR06] to investigate the cavity dynamics at several FSRs. By decomposing Eq. (5.12) and solving  $\delta a(t)$  in the frequency domain we get:

$$\delta\alpha(\omega) = \frac{-q\delta\alpha^\dagger(-\omega) + \sqrt{2\kappa_A}\delta A_{\text{in}}(\omega)}{\kappa_a - \frac{1-e^{i(\omega-\Delta_a)\tau}}{\tau}}, \quad (8.4)$$

given that  $\delta a^\dagger(\omega) = \delta a^\dagger(-\omega)$ . The fluctuations from the outcoupled field results from the boundary conditions (see Sec.4.2.2) and can be expressed as

$$\delta A_{\text{out}}(\omega) = \frac{\left[ \left( \kappa_a - \frac{1-e^{i(\omega-\Delta_a)\tau}}{\tau} \right) \left( \kappa_a + \frac{1-e^{i(\omega-\Delta_a)\tau}}{\tau} \right) + q^2 \right] \delta A_{\text{in}}(\omega)}{\left( \kappa_a - \frac{1-e^{i(\omega-\Delta_a)\tau}}{\tau} \right) \left( \kappa_a - \frac{1-e^{i(\omega-\Delta_a)\tau}}{\tau} \right) - |q|^2} - \frac{2\kappa_A q \delta A_{\text{in}}^\dagger(-\omega)}{\left( \kappa_a - \frac{1-e^{i(\omega-\Delta_a)\tau}}{\tau} \right) \left( \kappa_a - \frac{1-e^{i(\omega-\Delta_a)\tau}}{\tau} \right) - |q|^2}. \quad (8.5)$$

The output squeezing spectra for the amplitude and phase quadratures are, according to  $V^\pm \equiv \langle |\delta X^\pm|^2 \rangle^2 - \langle |\delta X^\pm|^2 \rangle \equiv \langle |\delta X^\pm|^2 \rangle$ , calculated to be

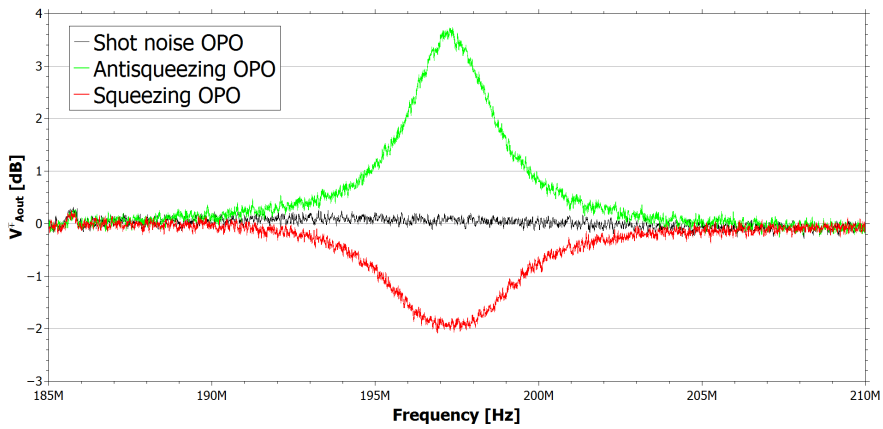
$$V_{\text{out}}^\pm(\omega) = \left| \frac{(\kappa_a \pm q)^2 - \left( \frac{1-e^{i\omega\tau}}{\tau} \right)^2}{\left( \kappa_a - \frac{1-e^{i\omega\tau}}{\tau} \right)^2 - |q|^2} \right|^2 V_{\text{in}}^\pm(\omega), \quad (8.6)$$

where  $\omega = n\omega_{\text{FSR}} = n2\pi/\tau$  is an integer multiple of the FSR.

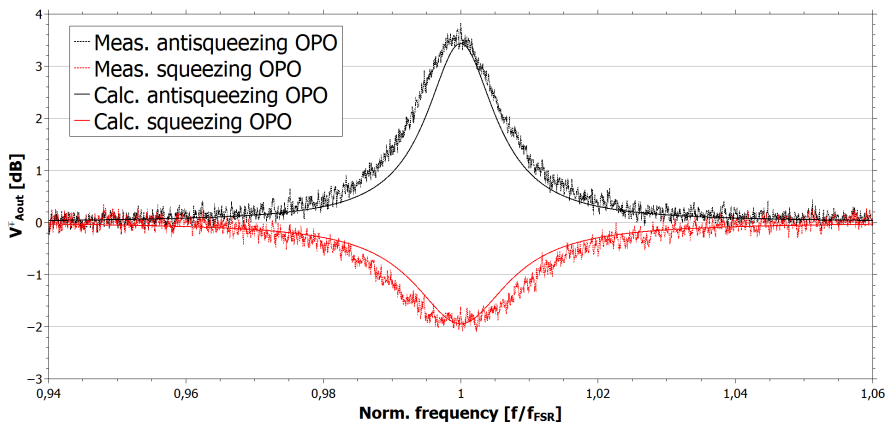
### Generated squeezed states by the OPO

Eq. (8.6) was used to calculate the performance of the sub-threshold bow-tie OPO that generates the squeezed states. The cavity is stabilized via PDH lock and the pump phase is locked with a dither lock on the copropagating back-seeded locking field (see Sec. 6.3). Using the cavity parameters from Table. 8.1 the simulated plot is confirmed by the measurements (see Fig. 8.2).

## 8.1. Squeezed states and signals at sideband frequencies



(a) OPO performance measurement (see Sec. 7.3).



(b) OPO performance simulation plot from Eq. (8.6).

**Figure 8.2.:** Comparison between theory and measurement of OPO performance. (a) Measurement of the OPO generated squeezing spectrum around 197.4 MHz with squeezing level (red) and antisqueezing level (green) versus scanned frequency (see Sec. 6.3). (b) Calculation of the (anti)squeezing level over the normalized frequency according to  $f_{\text{FSR}}$  from Eq. (8.6). In the background the measurements are displayed dotted for comparison.

### Resulting intensity noise spectrum

The squeezed light from the OPO is combined on a partially reflecting mirror (reflectivity of  $\eta = 0.99$ ) with the signal field being phase modulated at a frequency at  $\omega_m$  and with modulation depth  $\beta_m$ . That modulation frequency must be simultaneously coincident with an inte-

## 8. High-precision metrology enhanced with squeezed light

ger multiple of each of the FSRs of the OPO and the FP cavity under investigation so that the combined light passes through the cavity and is measured using a homodyne detection scheme. In the resulting intensity noise spectrum a lossless, impedance matched cavity is assumed for simplicity. A phase modulation of  $\omega_d=80$  kHz with modulation depth  $\beta_d$  represents a cavity length modulation as the signal of interest:

$$\begin{aligned}
 V_{\text{tot}}^+(\omega) &= \frac{\kappa_c^2 [\eta V_{\text{out}}^- + (1 - \eta)] + \left| \frac{1 - e^{i\omega\tau_c}}{\tau_c} \right|^2}{\left| \kappa_c \left( \frac{1 - e^{i\omega\tau_c}}{\tau_c} \right) \right|^2} + \frac{(1 - \eta)\beta_d^2\beta_m^2 A^2 \langle \delta_1(\omega) \rangle^2}{4 \left| \kappa_c \left( \frac{1 - e^{i\omega\tau_c}}{\tau_c} \right) \right|^2} \\
 &= \frac{\kappa_c^2 [\eta V_{\text{out}}^- + (1 - \eta)] + \left| \frac{1 - e^{i\omega\tau_c}}{\tau_c} \right|^2}{\left| \kappa_c \left( \frac{1 - e^{i\omega\tau_c}}{\tau_c} \right) \right|^2} \\
 &\quad + \frac{(1 - \eta)\beta_d^2\beta_m^2 A^2}{4 \left| \kappa_c \left( \frac{1 - e^{i\omega\tau_c}}{\tau_c} \right) \right|^2} \times [\pi\delta(\omega - \omega_m - \omega_d) + \pi\delta(\omega - \omega_m + \omega_d)],
 \end{aligned} \tag{8.7}$$

where  $(\beta_d\beta_m A/2)^2 = n_{\text{sb}}$  is the number of photons in each of the cascaded modulation sidebands [WRH06] and  $\langle \delta_1(\omega) \rangle^2$  is the normalized Fourier noise spectrum due to cavity length fluctuations [DHHR06]:

$$\langle \delta_1(\omega) \rangle^2 = \pi\delta(\omega - \omega_m - \omega_d) + \pi\delta(\omega - \omega_m + \omega_d), \tag{8.8}$$

where  $\delta(x)$  is the unit impulse function.

### Unit impulse function, modulation theorem and frequency shift property

The intermodulation product of the cascaded phase modulations can be considered as an amplitude modulation of  $\omega_d$  around the carrier at the first FSR with  $\omega_m$ . The modulation theorem for the Fourier transform [Bra99] states that, given a frequency modulation of  $f(t) = \cos(2\pi f_d t)$ ,  $F(\omega)$  can be expressed as

$$\begin{aligned}
 F(\omega) &= \int_{-\infty}^{\infty} \left( e^{i2\pi f_d t} + e^{-i2\pi f_d t} \right) e^{-i2\pi\omega t} dt \\
 &= \frac{1}{2} \int_{-\infty}^{\infty} e^{-i2\pi(\omega - \omega_d)t} dt + \frac{1}{2} \int_{-\infty}^{\infty} e^{-i2\pi(\omega + \omega_d)t} dt \\
 &= \pi\delta(\omega - \omega_d) + \pi\delta(\omega + \omega_d),
 \end{aligned} \tag{8.9}$$



## 8.1. Squeezed states and signals at sideband frequencies

---

where  $\delta(\omega)$  is the frequency domain unit impulse function (see App. A.4). Since we are interested in the amplitude modulation around the carrier at the first FSR we apply a frequency shift to the signal:  $f(t)e^{i2\pi f_m t}$ . The result in the Fourier space with  $\text{FT}[f(t)] = F(\omega)$  is an angular frequency shift of  $\omega_m$ :

$$\begin{aligned}\text{FT}[f(t)e^{i2\pi f_m t}](\omega) &= F(\omega - \omega_m) \\ &= \pi\delta(\omega - \omega_m - \omega_d) + \pi\delta(\omega - \omega_m + \omega_d).\end{aligned}\tag{8.10}$$

This result shows the behavior of the signal peaks frequency shifted by the cascaded phase modulation in the Fourier space. It describes its variance in the fluctuating part of the outcoupled field of the FP cavity in Eq. (8.7).

## 8. High-precision metrology enhanced with squeezed light

### 8.1.3. Simulations of combined signal peaks and squeezed light in the linear Fabry-Pérot cavity

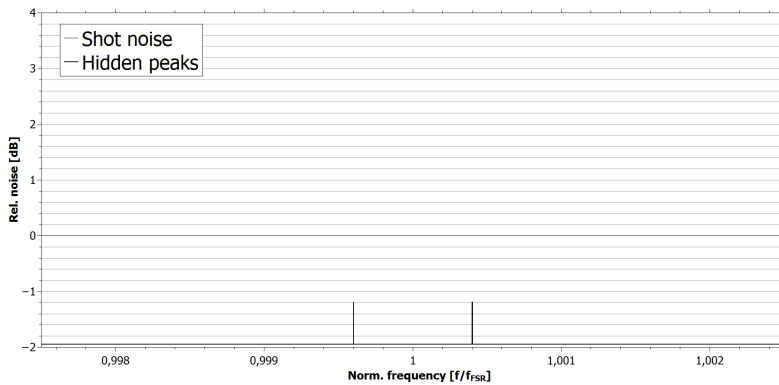
To simulate the total variance of the output field by Eq. (8.7), with the signal peaks frequency shifted by the cascaded phase modulation (see Eq. (8.10)) and the superimposed squeezed variance generated by the OPO (see Eq. (8.6)), the parameters for the FP cavity and cascaded phase modulation must be derived. All the parameters for the setup are given in Table 8.1.

**Table 8.1.** Overview of the parameters characterizing the OPO and the frequency-shifted signal detection in the Fabry-Pérot cavity.

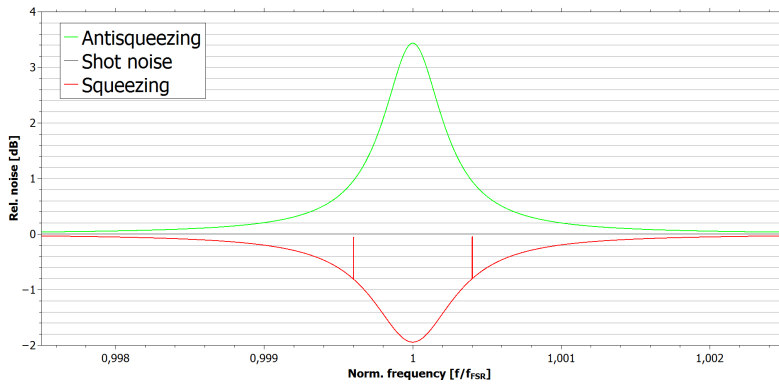
Parameter	Symbol	Value	Unit
<b>OPO parameters</b>			
Length	$l$	1.52	m
Free spectral range	$f_{\text{FSR}}$	197.4	MHz
Finesse	$\mathfrak{F}$	58	
Linewidth (FWHM)	$\Delta\nu = f_{\text{FSR}}/\mathfrak{F}$	3.96	MHz
Cavity decay rates (HWHM)	$\kappa_a = \pi \cdot \Delta\nu$	$1.24 \cdot 10^7$	rad/s
	$\kappa_A$	$1.07 \cdot 10^7$	rad/s
	$\kappa_{l,A}$	$0.18 \cdot 10^7$	rad/s
Nonlinearity factor (HWHM)	$ \chi $	$0.323 \cdot \kappa_a$	rad/s
Initial (anti)squeezing	$V_{\text{init}}^{\pm}$	$\pm 5.82$	dB
Detected squeezing	$V_{\text{det}}^-$	-1.96	dB
Detected antisqueezing	$V_{\text{det}}^+$	+3.78	dB
<b>Parameters for simulations</b>			
OPO cavity decay rate	$\kappa_a$	$1 \cdot 10^{-2} \cdot f_{\text{FSR}}$	Hz
FP cavity decay rate	$\kappa_c$	$1 \cdot 10^{-3} \cdot f_{\text{FSR}}$	Hz
FP cavity finesse	$\mathfrak{F}_c$	580	
Beamsplitter reflectivity	$\eta$	0.99	
Modulation depth	$\beta_m$	0.04	
	$\beta_d$	0.25	
Sideband amplitude	$A^2$	0.01	W
		$5.35 \cdot 10^{16}$	ph./s
Signal phase modulation (FSR)	$f_m = f_{\text{FSR}}$	197.4	MHz
Cavity length modulation	$f_d$	$2 \cdot 10^{-4} \cdot f_{\text{FSR}}$	Hz

With these parameters and Eq. (8.7) we simulate the variances of the outcoupled FP cavity field with the signal peaks on the squeezing-reduced noise floor.

## 8.1. Squeezed states and signals at sideband frequencies



(a) Single signal peaks



(b) Observable signal peaks on the squeezing-reduced noise floor

**Figure 8.3.:** Simulations of signal peaks with a squeezed light field in a linear Fabry-Pérot cavity. (a) The variance of the single signal peaks without the noise reduction of the squeezed light field from the OPO are below the 0 dB level and therefore covered by the shot noise. (b) The same signals can be uncovered by superimposing them with the squeezed light field from the OPO so that the signals of interest can be observed by balanced homodyne detection in transmission of the FP cavity.

Fig. 8.3a shows the variance of the single signal peaks without the noise reduction of the squeezed light field from the OPO. The peaks are below the 0 dB level and therefore hidden by the shot noise. The same signals can be uncovered by superimposing them with the squeezed light field from the OPO so that the signals of interest can be observed by balanced homodyne detection in transmission of the FP cavity (see Fig. 8.3b).

### 8.2. The experimental setup

The major part of the subsystems in Fig. 8.4 has already been described in this thesis, including the pump field preparation via the linear SHG (see Sec. 6.2) and the sub-threshold bow-tie OPO (see Sec. 6.3) for generating squeezed light. Within the scope of enhanced spectroscopy the signal of interest, masked by technical baseband noise, is up-shifted via phase modulation (see Sec. 8.1.1). Ideally, the modulation frequency is equivalent to higher FSRs of the FP cavity and the OPO to exploit the squeezed noise floor to uncover the signal of interest. Therefore, the additions to the experimental setup consist of a phase modulator for the signal field, a beamsplitter for superimposing the signal field with the squeezed light field and the FP cavity, and the implementation of the individual locking loops (see Fig. 8.4). To ensure a spatially and temporally filtered light field for highly sensitive laser optics experiments the initial light field is filtered by a fixed-spacer ring cavity, called a mode cleaner (MC) [WUG<sup>+</sup>98]. The half-waveplate was used to regulate the ratio of s- to p-polarization for generating a suitable error signal for the polarization-based homodyne detection (see Sec. 6.1.4) to stabilize the MC.

After this stage of preparation the laser light is split up by combinations of a half-waveplate and a PBS into three paths: pump field preparation, OPO stabilization/control field and FP cavity stabilization/signal field. The path for pump field preparation (see Sec. 6.2) is directed to the linear cavity for SHG. Similar to the light field at 1064 nm the pump field is filtered by a MC for 532 nm to be finally coupled into the sub-threshold OPO bow-tie cavity at the first curved mirror for squeezing generation (for a detailed description of the OPO bow-tie cavity see Sec. 6.3). All detection schemes for stabilization purposes so far are based on modulation-free polarization-based homodyne detection [HPJH09].

The squeezed light field is directed via a “flipping mirror” either to a detector (labeled *sqz detection*) to verify squeezing levels or to the linear FP cavity for the high-sensitivity phase spectroscopy. The squeezed light from the OPO is combined in phase on a beamsplitter with the signal light field. The signal field is phase modulated at 197.4 MHz, that is simultaneously coincident with the FSRs of the OPO and the linear FP cavity being stabilized by PDH-locking (see Sec. 6.1.2).

## 8.2. The experimental setup

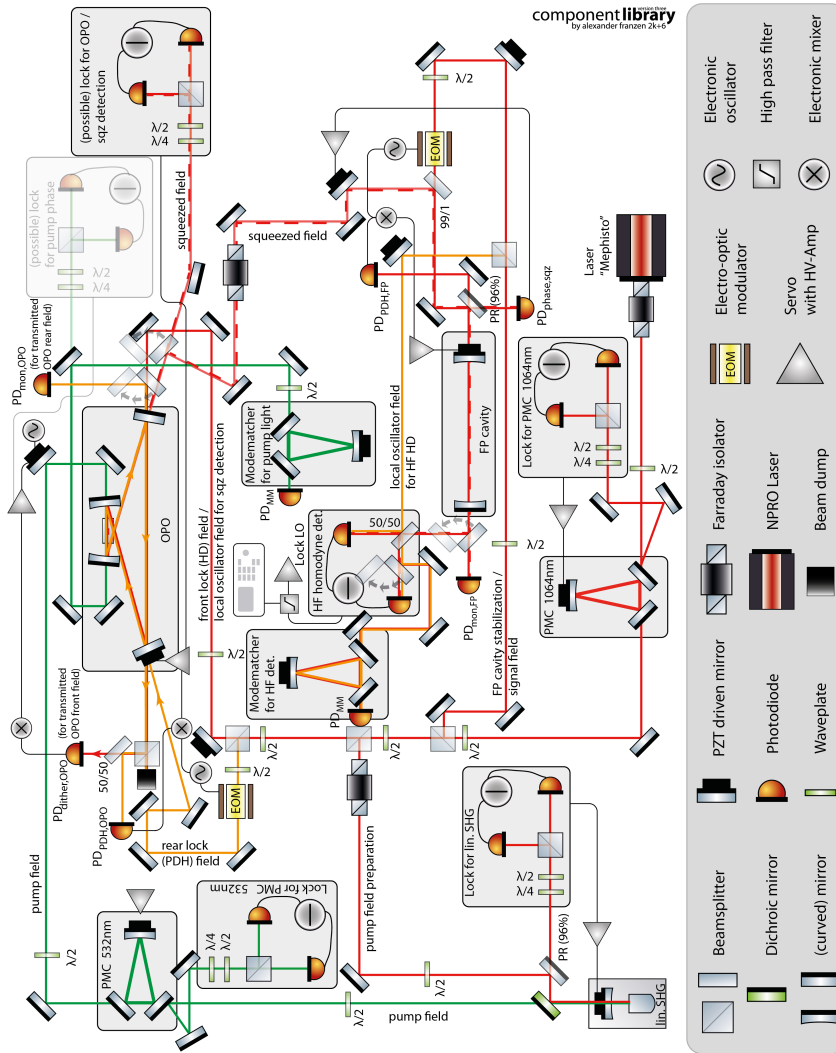


**Figure 8.4.:** Schematic of the complete experimental setup. The subsystems (linear SHG cavity, OPO for squeezing generation, individual locking loops) of the initial experimental part are individually described in the preceding chapters. The additions to the experimental setup consist of a phase modulator for the signal field, a beamsplitter for superimposing the signal field with the squeezed light field and the FP cavity, the implementation of the individual locking loops, and the balanced homodyne detection scheme for measuring squeezed states and signals at microwave sideband frequencies.

The transmitted light is detected by a high-frequency homodyne detector that measures the squeezed shot noise and the signal peaks in

## **8. High-precision metrology enhanced with squeezed light**

---

the amplitude quadrature. To ensure that the LO field for the homodyne detection is perfectly overlapped with the transmitted field from the FP cavity a mode matcher for the HF detection is implemented in transmission of the 50/50 beamsplitter. In the following the individual subsystems are described in more detail.

## 8.2.1. Linear Fabry-Pérot cavity

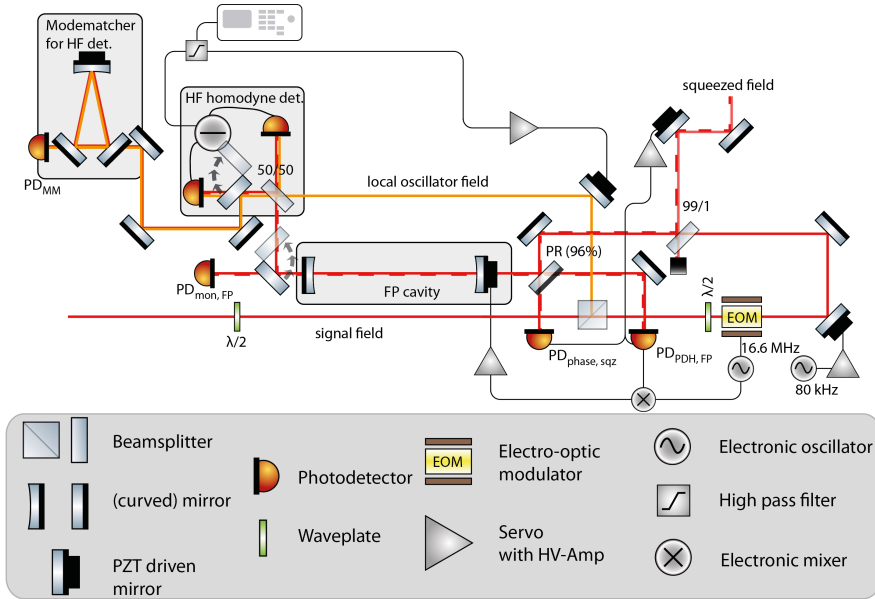


**Figure 8.5.:** Experimental setup of the FP cavity for sensitive optical phase shift measurements. To frequency stabilize the cavity a PDH locking scheme is used (see Sec. 6.1.2). Therefore, the signal field is additionally phase modulated with  $f_{\text{PDH}} = 16.6 \text{ MHz}$  by the same EOM. The error signal is derived by detecting the reflected light of the cavity transmitted through a partially transmissive ( $R = 96\%$ ) mirror for mode matching with a similar photodetector ( $\text{PD}_{\text{PDH, FP}}$ ) we use for stabilizing the OPO. The directly transmitted light field at the partially transmissive mirror is detected by  $\text{PD}_{\text{phase, sqz}}$  to stabilize the phase of the squeezed light field with respect to the signal field. The signals of interest superimposed with the squeezed light field from the OPO can be observed by a balanced homodyne detection in transmission of the FP cavity.

The linear FP cavity (see Fig. 8.5) consists of two identical curved mirrors (with  $\text{ROC} = 500 \text{ mm}$ ) with an optical path length of  $L = 757 \text{ mm}$  which leads to a theoretical FSR of  $198.01 \text{ MHz}$ . This is in good agreement with the measured FSR by scanning imprinted sidebands of an EOM<sup>1</sup> (see Sec. 8.2.3) with a broadband photodetector (see Sec. A.2.2). With the same measurement setup the linewidth of the resonator is determined to be  $\Delta\nu \approx 400 \text{ kHz}$ . Its stability pa-

<sup>1</sup>In this setup a high damage threshold phase modulator 4064 from Newport was used.

## 8. High-precision metrology enhanced with squeezed light

parameter is  $g_1 g_2 = 0.25$ . Both mirrors have a design reflectivity of ( $98.5\% < R < 99.5\%$ ) which corresponds to a cavity finesse of  $\mathfrak{F} = 580$ . The incoupling mirror is mounted on a PZT-crystal to adjust the cavity length to the laser frequency. To frequency stabilize the cavity a PDH locking scheme is used (see Sec. 6.1.2). Therefore, the signal field is phase modulated with  $f_{\text{PDH}} = 16.6$  MHz by the same EOM. The error signal is derived by detecting the reflected light of the cavity transmitted through a partially transmissive ( $R = 96\%$ ) mirror for mode matching with a similar photodetector ( $\text{PD}_{\text{PDH, FP}}$ ) we use for stabilizing the OPO (see Sec. 6.3). The output is multiplied with an electronic LO from the same function generator<sup>2</sup> driving also the EOM that imprints the sidebands at 16.6 MHz. A low-pass filter extracts the DC-term from the demodulated signal to get the desired error signal. The directly transmitted light field at the partially transmissive mirror is detected by  $\text{PD}_{\text{phase, sqz}}$  to stabilize the phase of the squeezed light field with respect to the signal field. To ensure the overlap of the signal of interest and the lowered noise floor provided by the squeezed light field both fields should be in phase. Therefore, a dither locking scheme (see Sec. 6.1.3) is required.

### 8.2.2. Polarization-based homodyne locking of a linear Fabry-Pérot cavity

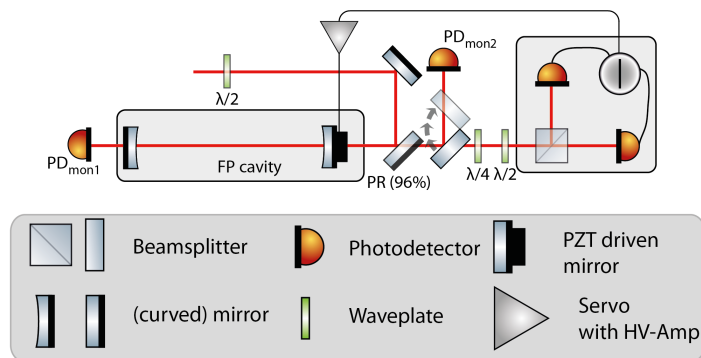


**Figure 8.6.:** Schematic of a linear Fabry-Pérot cavity stabilized via polarization based homodyne locking.

In all of the experimental setups described in this work the laser light that couples into the cavities is linearly polarized (either in s- or p-

<sup>2</sup>We used a RIGOL DG 1022 for the modulation and demodulation of the sidebands.



polarization, or in a composition of both). Usually degenerate in a linear cavity, both polarizations can be separated by differences in the refractive index of a nonlinear medium or the penetration depth in the mirror coating at a given angle of incidence. Having an empty FP cavity (no nonlinear medium inside) and two mirrors where the light impacts under zero degree, no splitting in the polarizations is expected. However, two potential sources that cause the splitting of the polarization eigenmodes in a FP cavity can be distinguished. The first one is the birefringence of the mirror materials, usually attributed to mechanical stress by clamping the mirror on the mount. Combined with a finite penetration depth, this leads to a polarization-dependent phase shift upon reflection. The second source is directly related to the cavity geometry. Its existence is not evident from the usual paraxial resonator theory, in which the cavity field and its resonances are described by a scalar mode function that is independent of the polarization [UBRR15].

The polarization-dependent differences in the reflected fields give rise to a possible locking scheme by polarization-based homodyne detection (see Sec. 6.1.4). By using the resonator equations (see Sec. 4.1.1) for the reflected fields for the different polarizations one can obtain the desired error signal.

### Mathematica calculations for polarization-dependent mirror parameters

For investigations into the polarization-dependent differences in the reflected fields the power reflectivities of the mirrors for s- and p-polarizations (representative of mirror curvature or penetration depth) are taken into account. Even slight differences in the power reflectivities provide an error signal. The reflected field (Eq. (4.5) with the angular (frequency) relation  $\theta = 2\omega L/c$ ) can be expressed as a function of the mirror parameters  $r$  and  $t$  for s- and p-polarizations [Fri91]:

$$a_{\text{ref}}(r, t) = a_{\text{in}} \frac{r_1 - r_2 (r_1^2 + t_1^2) e^{-i\theta}}{1 - r_1 r_2 e^{-i\theta}}, \quad (8.11)$$

The reflected fields for both polarizations ( $a_s$  and  $a_p$ ) are slightly different, as can be seen in Fig. 8.7.

## 8. High-precision metrology enhanced with squeezed light

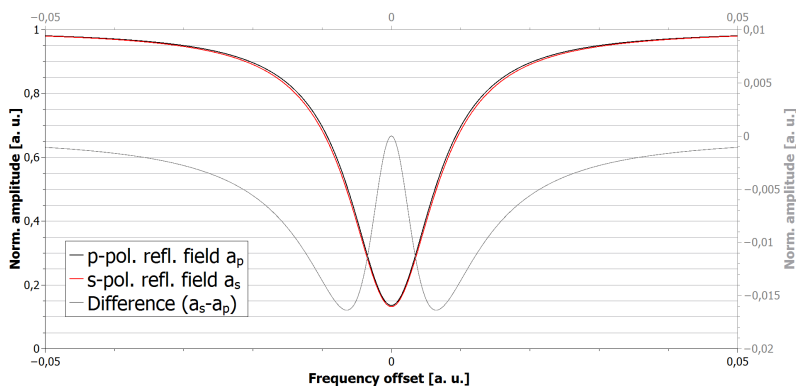


**Figure 8.7.:** Plot of reflected fields of s- and p-polarization.

The subtle distinction in the field intensities for s- and p-polarization creates a dispersion-shaped intensity gradient by subtraction of the two intensities  $I_{\text{res}} = I_a - I_b$  in a homodyne detection setup [HC80].

$$\begin{aligned}
 I_a &= y \left| \frac{1}{2} a_{\text{ref}}(r_p, t_p) + i a_{\text{ref}}(r_s, t_s) \right|^2, \\
 I_b &= y \left| \frac{1}{2} a_{\text{ref}}(r_p, t_p) - i a_{\text{ref}}(r_s, t_s) \right|^2,
 \end{aligned}
 \tag{8.12}$$

where  $y$  is a normalization coefficient.

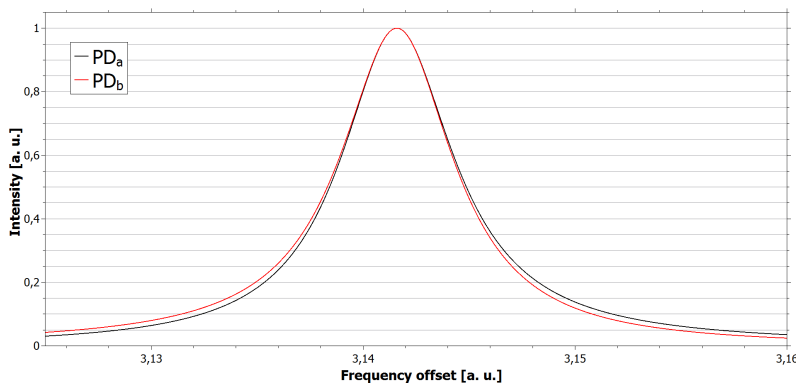


**Figure 8.8.:** Simulation of the intensities on both photodiodes in a homodyne detection setup from Eq. (8.12).

The subtraction of these two intensities  $I_{\text{res}} = I_a - I_b$  (see Fig. 8.8) leads to a dispersion-shaped error signal (see Fig. 8.9) which can be used for polarization-based homodyne locking.

## 8.2. The experimental setup

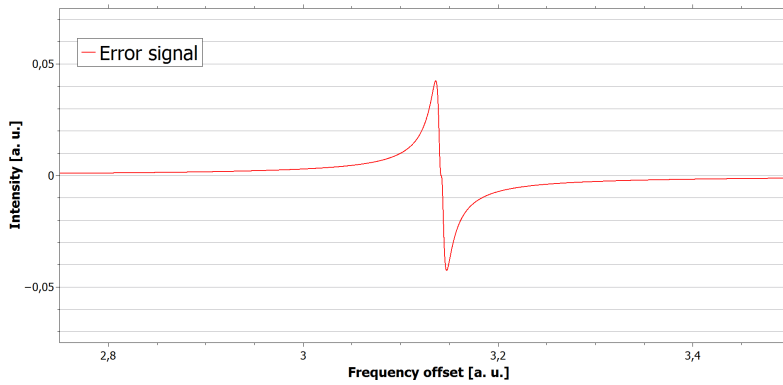


**Figure 8.9.:** Simulation of the resulting error signal in a homodyne detection setup by  $I_{\text{res}} = I_a - I_b$ .

## 8. High-precision metrology enhanced with squeezed light

### 8.2.3. Tuning the free spectral range of the Fabry-Pérot cavity

To ensure perfect overlap of the squeezed noise floor and the intermodulated sidebands around frequencies corresponding to higher FSRs of the OPO cavity (generating the squeezed field) the FSR of the FP cavity must be exactly the same; for the experimental setup described in this work the FSR is at 197.4 MHz. The accurate value of the FSR for the OPO cavity was obtained by span measurements over a certain frequency range. The frequency where the antisqueezed noise is maximal and the squeezed noise is minimal corresponds to the FSR. A comparable measurement with this precision is not possible for the FP cavity due to the absence of a frequency reference. Therefore modulation sidebands must be imprinted on the light field via the EOM and detected with a broadband photodetector (see App. A.2.2). By changing the modulation frequency, the detected sidebands move on the frequency axis with respect to the constant carrier until finally a cancellation of the positive sideband and the negative one of one higher FSR occurs. This happens when the frequency is exactly half of the FSR.

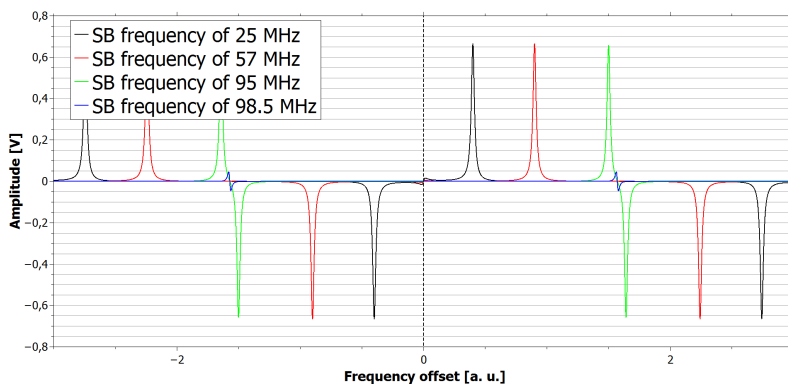


**Figure 8.10.:** Simulation of scanned sideband frequencies to find FSR of the Fabry-Pérot cavity. There is almost a cancellation of the sidebands at a frequency of 98.5 MHz (blue line). The modulation frequency of 99 MHz would lead to a complete cancellation of the sidebands.

As shown in the simulation plots in Fig. 8.10 the sidebands are detected by a photodetector with high bandwidth, since the modulation frequency is varied for tuning purposes. A photodetector with high bandwidth (see Sec. A.2.2) offers the resolution of different modulation sidebands to measure their dynamic behavior by tuning the

modulation frequency.

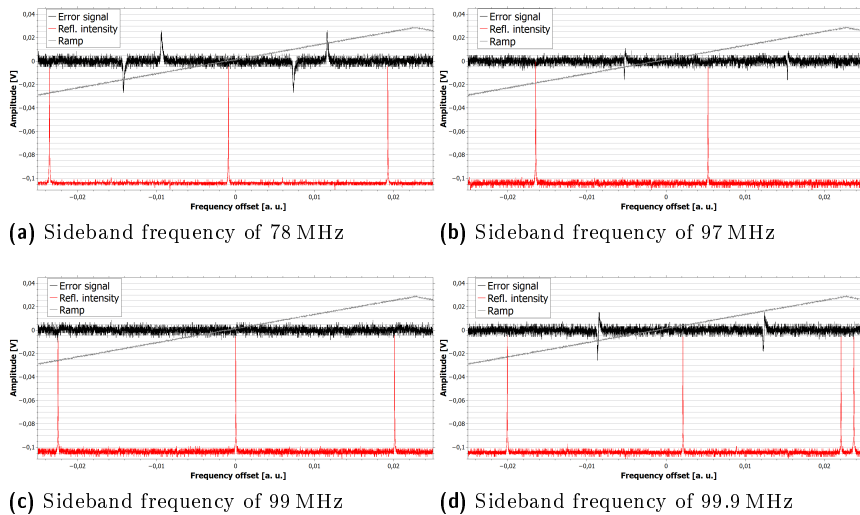


**Figure 8.11.:** Measurements of tuned sideband frequencies to determine the FSR of the linear Fabry-Pérot cavity. The error signal containing the sidebands is depicted as a black line, whereas the red line is the transmitted cavity field. (a) The modulation frequency is 78 MHz, far below 99 MHz where the sidebands cancel each other out. The left and right sideband are still separated from the corresponding neighboring sidebands of the adjacent FSRs. (c) With the matching modulation frequency of 99 MHz, the sidebands cancel each other out completely. There are two other cases plotted, where the modulation frequency is slightly below (b) and slightly above the half of the FSR (d).

The measurements of this sideband dynamic by tuning the sideband frequency are shown in Fig. 8.11. The error signal containing the sidebands is depicted as a black line, whereas the red line is the transmitted cavity field. The modulation frequency in Fig. 8.11a is 78 MHz, far below 99 MHz where the sidebands cancel each other out. According to the simulation there is a cancellation of the sidebands (Fig. 8.11c) at the modulation frequency of 99 MHz, whereas the FSR peaks in the transmitted field of the FP cavity remain constant. With this result the FSR of the FP cavity is determined to be 198 MHz. There are two other cases plotted, where the modulation frequency is slightly below (Fig. 8.11b) and slightly above the half of the FSR (Fig. 8.11d).

## 8. High-precision metrology enhanced with squeezed light

---

### Further steps

At the time of writing, the final detection of the combined signal superimposed on the squeezed noise floor had not yet been achieved due to problems with the stabilization of the OPO cavity for squeezed-light generation. Drifts in room temperature led to the need for successive re-alignment of the OPO cavity (crucial for all of the locking tasks). The complete setup was characterized and assembled to assure a measurement in the near future.

The next steps are re-aligning the OPO cavity to be sufficient to stabilize it on timescales suitable for spectroscopic measurements and to produce a suitable level of squeezing. Potentially, the optical surfaces and the crystal have to be cleaned to reduce additional losses. Since the experimental setup consists of different modulations (e.g. for locking purposes and for up-shifting the signal) and stabilization schemes for the different subsystems a hierarchy of subsystem stabilizations must be established. Once this is achieved the transmitted light field of the FP cavity can be detected in a balanced homodyne detection scheme. As a first step the amplitude-modulated signals by the cascaded phase modulation can be detected without being superimposed by the squeezed light to confirm the theoretical derivation of squeezed states and signals at microwave sideband frequencies. Then the squeezed light field can be detected in transmission of the FP cavity to verify that the phase lock of the squeezed light field and the signal field in combination with the cascaded phase modulation and the FP cavity stabilization works. This will lead to the experimental verification of the theoretical results presented in Sec. 8.1.

# 9

## Chapter 9

# Summary & Outlook

The focus of my experimental work was the development and implementation of a nonlinear light source for fundamental research in the fields of frequency stabilization and high-precision spectroscopy. A sub-threshold optical parametric oscillator (OPO) was constructed using a bow-tie cavity for the generation of squeezed states at a wavelength of 1064 nm at free spectral ranges (FSRs) in the MHz regime. For the preparation stage of the pump light field at a wavelength of 532 nm I assembled two different cavity geometries and crystals for second-harmonic generation (SHG) and compared their efficiency. A modulation-free locking technique, based on polarization spectroscopy of the reflected light field from an anisotropic cavity, was used to stabilize both cavities. The linear cavity using a MgO:LiNbO<sub>3</sub>-crystal and the bow-tie cavity using a PPKTP-crystal achieved comparable results in the conversion from 1064 nm to 532 nm with an efficiency of  $\sim 60\%$ . The decision to use the linear cavity for the pump field preparation for squeezing experiments, presented in this work, was based on its compactness. Additionally, the free-mounted bow-tie cavity with widely separated components was bound to be more sensitive to air fluctuations than the hemilithic resonator of the linear SHG.

In order to design the setup for the OPO and its stabilization scheme I performed a theoretical investigation into the cavity dynamics with the optical parametric down-conversion process while taking into account the weak depletion of the pump field and of frequencies far beyond cavity resonance. This investigation resulted in several insights: firstly, the small fluctuations around the average pump field amplitude caused by the nonlinear interaction with the seed field, named weak pump depletion (WPD), can be used to lock the phase angle

## 9. Summary & Outlook

---

between the pump field and the seed field. This thesis reports on the theoretical and experimental work leading to the novel WPD locking technique. The comparison of this new scheme to a common dither locking scheme showed that both stabilization techniques were suitable for locking the OPO. I achieved a pump phase stabilization of the OPO via WPD locking while generating squeezed light at levels up to 2.5 dB. In order to utilize the squeezed light for downstream experiments I investigated different stabilization setups to control the OPO and its pump phase in this work. Since the WPD locking technique utilizes a very small nonlinear effect it is technically extremely challenging to generate a suitable error signal by detecting the pump field. Nevertheless I demonstrated that locking the pump phase by means of the WPD locking technique is possible.

Deriving the cavity dynamics at frequencies far beyond cavity resonance show that the OPO generates squeezed light in every FSR, which is detectable with a high-bandwidth homodyne detector. We proposed the idea of an enhanced spectroscopy setup consisting of up-shifted signals via a cascaded phase modulation and a Fabry-Pérot cavity with squeezed-light injection. I simulated the cavity dynamics for squeezed states and signals at sideband frequencies at higher FSRs to show the possibility of detecting a small signal, which is masked by technical baseband noise. If the signal is up-shifted to sideband frequencies at the first FSR of the OPO and the FP cavity it will re-appear due to the absence of technical noise and by virtue of the reduced noise floor, which is lowered by the introduced squeezed light. In this soon-to-follow experimental realization this will result in improved high-precision phase measurements in cavity spectroscopy, with possible applications for cavity ring-down spectroscopy (CRDS) in the fields of optical frequency metrology or studies of light-matter interactions.





## Appendix A

# Appendix

### A.1. Calculation of the nonlinearity factor with measurement values

As we are interested in the nonlinearity factor  $|\chi|$  (see Sec. 7.1.1) related to the linear gain and the decay rate  $\kappa_A$  we calculate the amount of gain with the detected outcoupled field  $|\alpha_{\text{out}}|^2$  divided by the incoupling field  $|\alpha_{\text{in}}|^2$ :

$$\text{Gain}_{\text{max}} = \frac{|\alpha_{\text{out}}|^2}{|\alpha_{\text{in}}|^2} = \frac{(\kappa_A - |\chi|)^2}{(\kappa_A + |\chi|)^2} \quad (\text{A.1})$$

$\text{Gain}_{\text{max}}$  is the gain introduced by the maximum amount of (anti-)squeezing (in dB). To calculate the initial (anti)squeezing values  $V_{\text{dB}}^{\pm}$  we assume that the measured values  $V_{\eta,\text{dB}}^{\pm}$  experienced an optical loss  $\eta_{\text{total}}$ :

$$V_{\eta,\text{dB}}^{\pm} = 10 \log_{10} \left( \eta_{\text{total}} 10^{\frac{V_{\text{dB}}^{\pm}}{10}} + (1 - \eta_{\text{total}}) \right) \quad (\text{A.2})$$

For this reason we solve Eq. (A.2) for  $V_{\eta,\text{dB}}^+$  and  $V_{\eta,\text{dB}}^-$  with  $V_{\text{dB}}^+ = -V_{\text{dB}}^-$  for the same loss value  $\eta_{\text{total}}$  and equalize it, so we get

$$V_{\text{dB}}^{\pm} = \log_{10} \left( \frac{-1 + 10^{V_{\eta,\text{dB}}^-/10}}{-1 + 10^{V_{\eta,\text{dB}}^+/10}} \right) \quad (\text{A.3})$$

With the result the total optical loss factor  $\eta_{\text{total}} = 0.5$  is calculated. Taking this into account by calculating the theoretical lossless values with Eq. (7.9) we end up with the measured values.

### A.2. High frequency (homodyne) detectors

Beside the common detection devices some special detectors were needed in this experiment. A homodyne detector with a high frequency bandwidth for the detection of squeezed states at higher FSRs was used.

To detect and demodulate tunable modulation frequencies in order to investigate the FSR of the FP cavity a photodetector with a broad frequency bandwidth was used.

#### High frequency homodyne detector from Australia

The high frequency homodyne detector that was used in this work was a loan of the Quantum Electronics group at the University of New South Wales led by Prof. Huntington. Based on its characteristics we developed a comparable homodyne detector to gain the experience in high frequency electronics and detection. The research on improvements are still in progress.

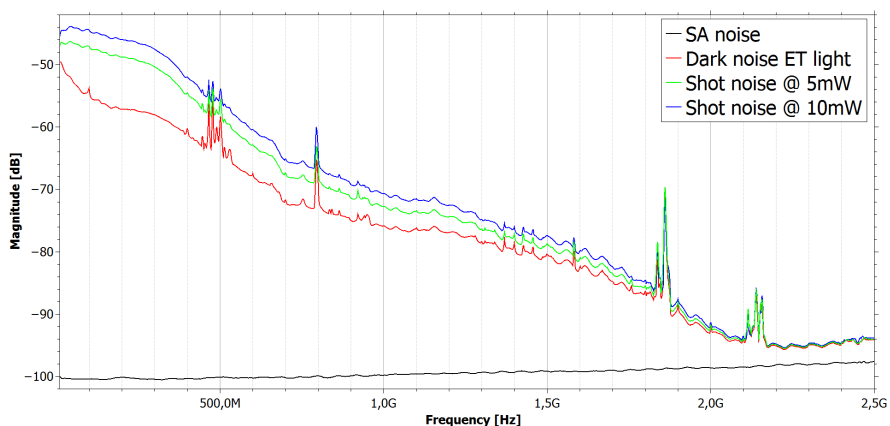


**Figure A.1.:** Plot of the shot noise levels of the Australian high frequency homodyne detector over the full range of 2.5 GHz. For the incident powers of 5 mW and 10 mW the shot-noise levels are detected. It is constantly 10 dB above the dark noise level over the frequency range up to 1.2 GHz.

## A.2. High frequency (homodyne) detectors

### High frequency homodyne detector V2

Adapted from the Australian detector provided by the work group of Prof. Huntington a novel homodyne detector design was developed in collaboration with Dr. Mehmet. It aims at having a large bandwidth and a low noise contribution similar to the Australian detector (see Fig. A.1). The circuit board (see Fig. A.3) and housing was built in house by the electronic and mechanical workshop. The two photodiodes were mounted back-to-back for a direct subtraction of the current and this current was split up into a high frequency and a low frequency part. At the (low frequency) DC-port the subtracted current is converted into a voltage via transimpedance amplifiers to generate a suitable error signal for locking purposes. The (high frequency) AC path consists of microwave amplification transistors<sup>1</sup> to generate a voltage signal with higher frequencies providing measurements of the signal variance (see Eq. (3.15) and Eq. (4.32)) at higher FSRs of the cavity under investigation. This preamplifier features high gain, low noise, a regulated power supply for good isolation from external noises on the supply side and a good bandwidth. Several tests of microwave shielding and impedance matching of different components have been done; work is still in progress.

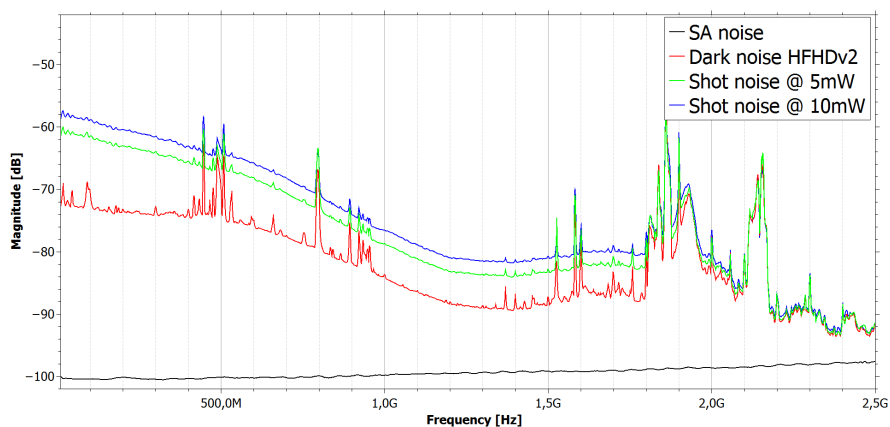


**Figure A.2.:** Plot of the shot noise levels of HFHD(v2) over the full range of 2.5 GHz. For the incident powers of 5 mW and 10 mW the shot-noise levels are detected. It is constantly 10 dB above the dark noise level over the frequency range up to 1.8 GHz, neglecting single peak disturbances.

<sup>1</sup>We used the monolithic amplifier *Mar-6+* from Mini Circuits, see Sec. A.2.1.

## A. Appendix

---

The integrated photodiodes are high speed InGaAs photodiodes<sup>2</sup> with an active area of  $70\ \mu\text{m}$ . The length of the pin contacts of the photodiodes and the circuit path layout cause that the photodetector forms an antenna that contaminates a few frequency bands of the measurement over the range of 2.5 GHz by electromagnetic interspersions (see Fig. A.2). To characterize this in house built homodyne detector the dark noise (red curve) is measured and compared to the detected vacuum noise levels by using local oscillator powers of 5 mW and 10 mW (green and blue curve). Neglecting single peak disturbances the vacuum noise level above dark noise is constantly above 10 dB over the full frequency range. Above 1.8 GHz the dark noise and the shot noise experience several electronic pick-up peaks that will spoil measurements. Nevertheless, the high frequency homodyne detector is adequate for squeezing measurements with a high clearance between dark noise and shot noise over a range of 1.8 GHz.

### A.2.1. Photodetector circuit

---

<sup>2</sup>We used *FCI InGaAs-70* from OSI Optoelectronics.

## A.2. High frequency (homodyne) detectors

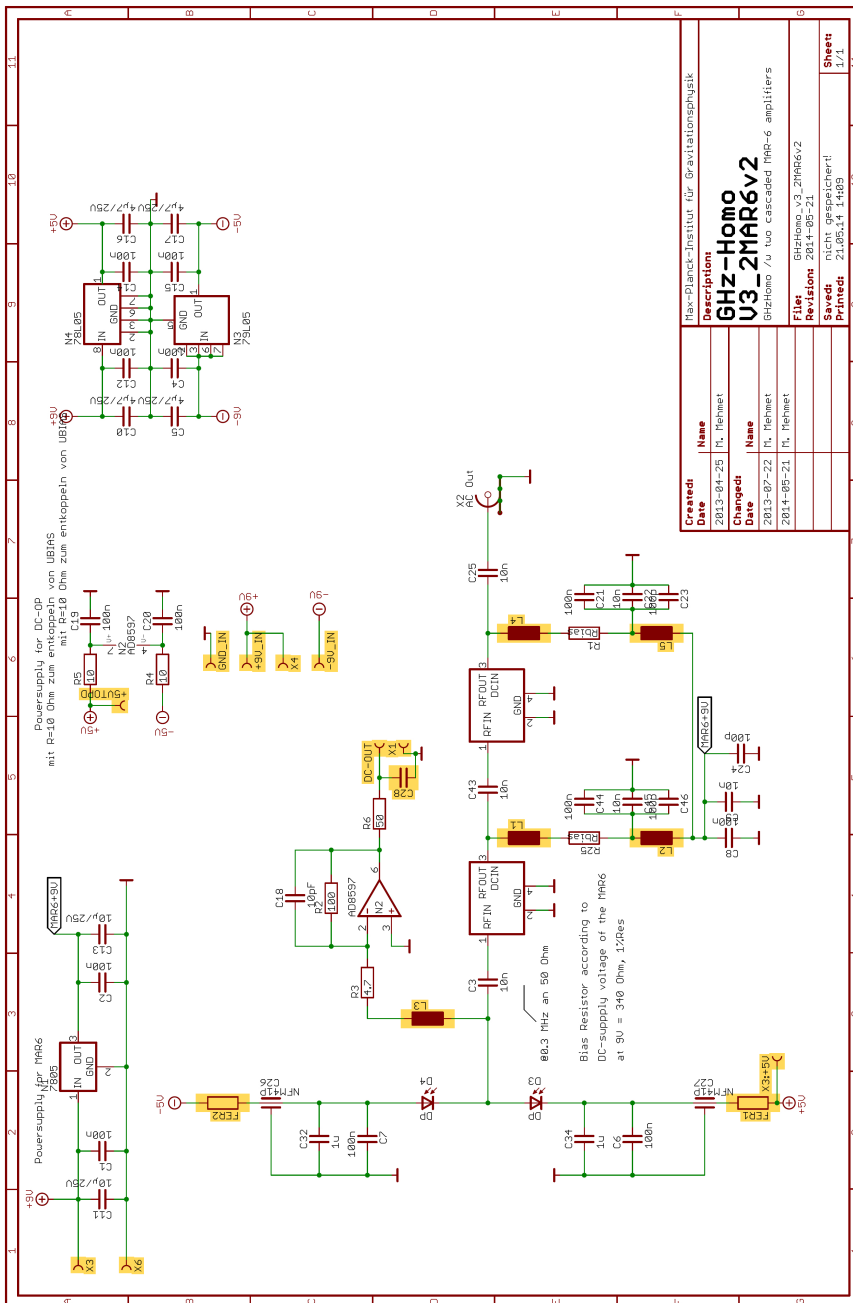
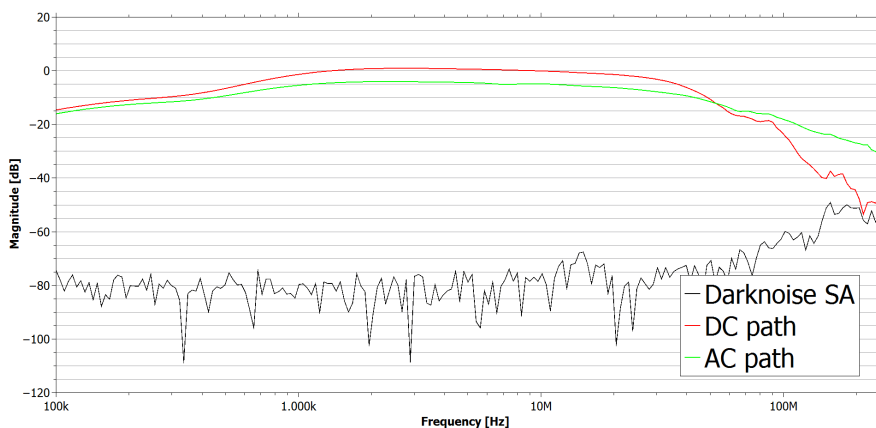


Figure A.3.: Schematic of the high frequency homodyne detector V2.

### A.2.2. High frequency bandwidth photodetector

The benefit of a sensitive photodetection over a broad bandwidth is the free choice of a modulation frequency for a beat signal detection in a possible PDH-stabilization scheme. In many cases the photodiode with its finite capacitance is part of an inductor-capacitor-network to utilize the resonant frequency for increasing the detection sensitivity on resonance. However, in this experimental setup it has to perform another task. To determine the exact frequency of the FSR of the Fabry-Pérot cavity the optical beat between the carrier field and the modulation sidebands is detected. By turning the modulation frequency to the half of the FSR the detected sidebands (of adjoining FSRs) cancel each other out. Therefore it is important to ensure the detection of that beat signal over a broad frequency bandwidth.



**Figure A.4.:** Plot of the transfer function of a broadband frequency photodetector.

The low power operational amplifiers<sup>3</sup> provide approximately 100 MHz bandwidth and low distortion. Fig. A.4 shows a plot of the shotnoise in its AC and DC path. At 80 MHz the shotnoise level of the detector drops down and at 105 MHz the shotnoise-clearance is smaller than 10 dB.

<sup>3</sup>AD810, AD 797A from Analog Devices.

## A.3. High FSR detection for multiplexing experiments

Having a homodyne detector with a high frequency bandwidth available the high-precision phase measurements are feasible even at higher FSRs of the FP cavity. The detection of such a squeezing comb gives rise to a source of quantum states for multiplexed quantum communication systems. In quantum key distribution these squeezed states of each FSR are generating a bit code for secure data transfers between two parties.

### A.3.1. Squeezing comb detection

By using a high frequency photodetector measurements of several FSRs are possible; a squeezing comb is detectable. This measurement was performed by the two high frequency homodyne detectors (which are described in Sec. A.2). In Fig. A.5 and Fig. A.6 the well defined dips in the detected shotnoise belonging to the generated squeezing at each free spectral range of the OPO cavity are observable. Having several squeezing ports available a multiplexed entanglement for quantum communications applications can be applied [HWD<sup>+</sup>10].

#### Squeezing comb with ET light

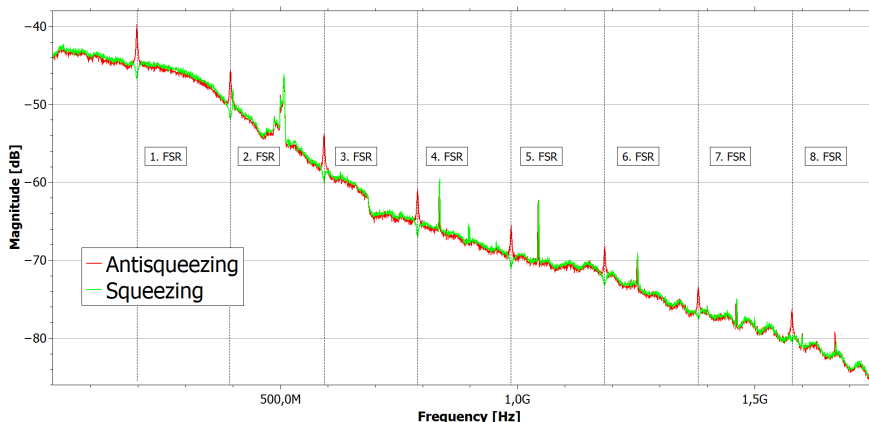
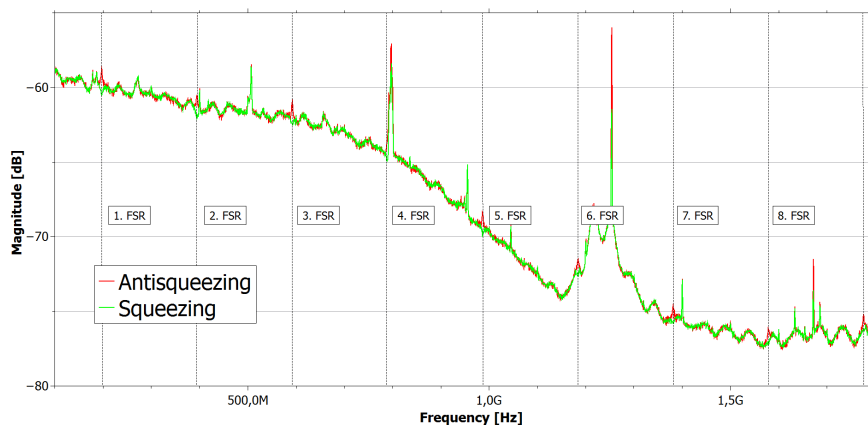


Figure A.5.: Plot of generated squeezing comb at different FSRs over a broad frequency range.

## A. Appendix

---

### Squeezing comb with HFHD V2



**Figure A.6.:** Plot of generated squeezing comb at different FSRs over a broad frequency range.

Both detectors are capable to detect squeezed states at least up to the ninth FSR.



## A.4. Theorems for the Fourier transformation

Some basic theorems play an important role in dealing with Fourier transforms, especially with the unit impulse function  $\int_{-\infty}^{\infty} \delta(t) dt = 1$  or the frequency domain unit impulse function  $\int_{-\infty}^{\infty} \delta(\omega) d\omega = 1$ . Following [Bra99] we establish the unity of the impulse function. Therefore the behavior of the Gaussian function under Fourier transformation is depicted and investigated via a substitution.

### A.4.1. Fourier transform of the Gaussian function

The Fourier transform theorem for the normalized Gaussian functions  $f(t) = e^{-\pi t^2}$  and  $f(\omega) = e^{-\pi \omega^2}$  implies the transformation pair:

$$\begin{aligned}
 FT[f(t)](\omega) &= \int_{-\infty}^{\infty} f(t) e^{-i2\pi\omega t} dt \\
 &= \int_{-\infty}^{\infty} e^{-\pi t^2} e^{-i2\pi\omega t} dt \\
 &= \int_{-\infty}^{\infty} e^{-\pi(t^2 + i2t\omega)} dt \\
 &= e^{-\pi\omega^2} \int_{-\infty}^{\infty} e^{-\pi(t+i\omega)^2} dt \\
 &= e^{-\pi\omega^2} \int_{-\infty}^{\infty} e^{-\pi(t+i\omega)^2} d(t+i\omega) \\
 &= e^{-\pi\omega^2},
 \end{aligned} \tag{A.4}$$

and analogous

$$\begin{aligned}
 FT[f(\omega)](t) &= \int_{-\infty}^{\infty} f(\omega) e^{-i2\pi\omega t} d\omega \\
 &= \int_{-\infty}^{\infty} e^{-\pi\omega^2} e^{-i2\pi\omega t} d\omega \\
 &= e^{-\pi t^2}.
 \end{aligned} \tag{A.5}$$

## A. Appendix

---

### A.4.2. Derivation of the unit impulse function by substitution

Considering these results for the Gaussian function a substitution of variables leads to:

$$\begin{aligned} FT[f(at)](\omega) &= \int_{-\infty}^{\infty} e^{-\pi(at)^2} e^{-i2\pi\omega t} dt \\ &= \int_{-\infty}^{\infty} e^{-\pi\left(t^2 + it\frac{\omega}{|a|}\right)} \frac{dt}{|a|} \\ &= \frac{1}{|a|} e^{-\pi(\omega/a)^2} \int_{-\infty}^{\infty} e^{-\pi\left(t + i\frac{\omega}{|a|}\right)^2} d\left(t + i\frac{\omega}{|a|}\right) \\ &= \frac{1}{|a|} e^{-\pi(\omega/a)^2}. \end{aligned} \tag{A.6}$$

For the case  $a \rightarrow 0$ , the upper line gives a defined representation for the impulse function  $\delta(\omega)$  and the lower line is a Fourier transform integral with unity in the limit.

“1 is the Fourier transform in the limit of  $\delta(\omega)$ .” [Bra99]

## Bibliography

- [AAA<sup>+</sup>13] AASI, Junaid ; ABADIE, J ; ABBOTT, BP ; ABBOTT, Richard ; ABBOTT, TD ; ABERNATHY, MR ; ADAMS, Carl ; ADAMS, Thomas ; ADDESSO, Paolo ; ADHIKARI, RX u. a.: Enhanced sensitivity of the LIGO gravitational wave detector by using squeezed states of light. In: *Nature Photonics* 7 (2013), Nr. 8, S. 613–619 3, 99
- [ABDP62] ARMSTRONG, JA ; BLOEMBERGEN, N ; DUCUING, J ; PERSHAN, PS: Interactions between light waves in a nonlinear dielectric. In: *Physical Review* 127 (1962), Nr. 6, S. 1918 55
- [Bak02] BAKER, HF: On the calculation of the finite equations of a continuous group. In: *Proceedings of the London Mathematical Society* 1 (1902), Nr. 1, S. 332–333 19
- [BBB15] BENNETT, Robert ; BARLOW, Thomas M. ; BEIGE, Almut: A physically motivated quantization of the electromagnetic field. In: *European Journal of Physics* 37 (2015), Nr. 1, S. 014001 7
- [BBC<sup>+</sup>93] BENNETT, Charles H. ; BRASSARD, Gilles ; CRÉPEAU, Claude ; JOZSA, Richard ; PERES, Asher ; WOOTTERS, William K.: Teleporting an unknown quantum state via dual classical and Einstein-Podolsky-Rosen channels. In: *Phys. Rev. Lett.* 70 (1993), Mar, 1895–1899. <http://dx.doi.org/10.1103/PhysRevLett.70.1895>. – DOI 10.1103/PhysRevLett.70.1895 63
- [Boy03] BOYD, Robert W.: *Nonlinear optics*. Academic press, 2003 51, 52, 55
- [BR04] BACHOR, Hans-Albert ; RALPH, Timothy C.: *A guide to experiments in quantum optics*. wiley-vch, 2004 29, 30, 31, 32, 36, 37, 85, 86

## BIBLIOGRAPHY

---

- [Bra99] BRACEWELL, Ronald N.: *The Fourier transform and its applications*. 3rd Edition. Boston [etc.] : McGraw Hill, cop. 2000., 1999 (McGraw-Hill series in electrical and computer engineering., Circuits and systems.). – 496 S. 106, 131, 132
- [BSCH11] BOYSON, TK ; SPENCE, TG ; CALZADA, ME ; HARB, CC: Frequency domain analysis for laser-locked cavity ringdown spectroscopy. In: *Optics express* 19 (2011), Nr. 9, S. 8092–8101 4
- [Cav81] CAVES, Carlton M.: Quantum-mechanical noise in an interferometer. In: *Phys. Rev. D* 23 (1981), Apr, 1693–1708. <http://dx.doi.org/10.1103/PhysRevD.23.1693>. – DOI 10.1103/PhysRevD.23.1693 63
- [CC16] COLLABORATION, LIGO S. ; COLLABORATION, Virgo: Observation of Gravitational Waves from a Binary Black Hole Merger. In: *Phys. Rev. Lett.* 116 (2016), 061102. <http://dx.doi.org/10.1103/PhysRevLett.116.061102>. – DOI 10.1103/PhysRevLett.116.061102 1, 2, 4
- [CG84] COLLETT, MJ ; GARDINER, CW: Squeezing of intracavity and traveling-wave light fields produced in parametric amplification. In: *Physical Review A* 30 (1984), Nr. 3, S. 1386 59
- [Che07] CHELKOWSKI, Simon: *Squeezed light and laser interferometric gravitational wave detectors*, Gottfried Wilhelm Leibniz Universität Hannover Hannover, Diss., 2007 20
- [CWBF13] CLARKE, Jordan ; WANG, Haoyu ; BROWN, Daniel ; FREISE, Andreas: Revisiting 'Sidebands of Sidebands' in Finesse. In: *LIGO DCC* T1300986 (2013) 103
- [Dar27] DARWIN, CG: Free motion in the wave mechanics. In: *Proceedings of the Royal Society of London. Series A* 117 (1927), Nr. 776, S. 258–293 63
- [Deu85] DEUTSCH, D.: Quantum Theory, the Church-Turing Principle and the Universal Quantum Computer. In:

*Proceedings of the Royal Society of London. A. Mathematical and Physical Sciences* 400 (1985), Nr. 1818, 97-117. <http://dx.doi.org/10.1098/rspa.1985.0070>. – DOI 10.1098/rspa.1985.0070 63

- [DHHR06] DUNLOP, A. E. ; HUNTINGTON, E. H. ; HARB, C. C. ; RALPH, T. C.: Generation of a frequency comb of squeezing in an optical parametric oscillator. In: *Physical Review A* 73 (2006), Nr. 1, S. 013817 59, 60, 62, 100, 104, 106
- [DHK<sup>+</sup>83] DREVER, R.W.P. ; HALL, J.L. ; KOWALSKI, F.V. ; HOUGH, J. ; FORD, G.M. ; MUNLEY, A.J. ; WARD, H.: Laser phase and frequency stabilization using an optical resonator. In: *Applied Physics B* 31 (1983), Nr. 2, 97-105. <http://dx.doi.org/10.1007/BF00702605>. – DOI 10.1007/BF00702605. – ISSN 0946-2171 64, 65, 83
- [DLCZ01] DUAN, L. M. ; LUKIN, M. D. ; CIRAC, J. I. ; ZOLLER, P.: Long-distance quantum communication with atomic ensembles and linear optics. In: *Nature* 414 (2001), November, Nr. 6862, 413-418. <http://dx.doi.org/10.1038/35106500>. – DOI 10.1038/35106500. – ISSN 0028-0836 63
- [DSW<sup>+</sup>15] DENKER, T. ; SCHÜTTE, D. ; WIMMER, M. H. ; WHEATLEY, T. A. ; HUNTINGTON, E. H. ; HEURS, M.: Utilizing weak pump depletion to stabilize squeezed vacuum states. In: *Opt. Express* 23 (2015), Jun, Nr. 13, 16517-16528. <http://dx.doi.org/10.1364/OE.23.016517>. – DOI 10.1364/OE.23.016517 58, 84
- [Ein16a] EINSTEIN, Albert: Die grundlage der allgemeinen relativitätstheorie. In: *Annalen der Physik* 354 (1916), Nr. 7, S. 769-822 3
- [Ein16b] EINSTEIN, Albert: Näherungsweise Integration der Feldgleichungen der Gravitation – Sitzungsbericht. In: *Königlich Preuß. Akad. Wiss* (1916), S. 201 2, 3
- [Eke91] EKERT, Artur K.: Quantum cryptography based on Bell's theorem. In: *Phys. Rev. Lett.* 67

## BIBLIOGRAPHY

---

- (1991), Aug, 661–663. <http://dx.doi.org/10.1103/PhysRevLett.67.661>. – DOI 10.1103/PhysRevLett.67.661 63
- [ENKB91] ECKARDT, Robert C. ; NABORS, CD ; KOZLOVSKY, William J. ; BYER, Robert L.: Optical parametric oscillator frequency tuning and control. In: *JOSA B* 8 (1991), Nr. 3, S. 646–667 56
- [ESB<sup>+</sup>10] EBERLE, Tobias ; STEINLECHNER, Sebastian ; BAUCHROWITZ, Jöran ; HÄNDCHEN, Vitus ; VAHLBRUCH, Henning ; MEHMET, Moritz ; MÜLLER-EBHARDT, Helge ; SCHNABEL, Roman: Quantum Enhancement of the Zero-Area Sagnac Interferometer Topology for Gravitational Wave Detection. In: *Phys. Rev. Lett.* 104 (2010), Jun, 251102. <http://dx.doi.org/10.1103/PhysRevLett.104.251102>. – DOI 10.1103/PhysRevLett.104.251102 1, 63
- [FMJB92] FEJER, Martin M. ; MAGEL, GA ; JUNDT, Dieter H. ; BYER, Robert L.: Quasi-phase-matched second harmonic generation: tuning and tolerances. In: *Quantum Electronics, IEEE Journal of* 28 (1992), Nr. 11, S. 2631–2654 57
- [Fri91] FRITSCHEL, Peter K.: *Techniques for laser interferometer gravitational wave detectors*, Massachusetts Institute of Technology, Diss., 1991 115
- [FS10] FREISE, Andreas ; STRAIN, Kenneth: Interferometer Techniques for Gravitational-Wave Detection. In: *Living Rev. Relativity* 13 (2010), Nr. 1 23, 24, 30, 39, 40, 44, 76
- [FSMA08] FOLTYNOWICZ, Aleksandra ; SCHMIDT, Florian M. ; MA, Weiguang ; AXNER, Ove: Noise-immune cavity-enhanced optical heterodyne molecular spectroscopy: Current status and future potential. In: *Applied Physics B* 92 (2008), Nr. 3, S. 313–326 4, 99
- [GBML06] GROSSE, Nicolai B. ; BOWEN, Warwick P. ; MCKENZIE, Kirk ; LAM, Ping K.: Harmonic Entanglement with Second-Order Nonlinearity. In: *Phys. Rev.*

*Lett.* 96 (2006), Feb, 063601. <http://dx.doi.org/10.1103/PhysRevLett.96.063601>. – DOI 10.1103/PhysRevLett.96.063601 83

- [GC85] GARDINER, CW ; COLLETT, MJ: Input and output in damped quantum systems: Quantum stochastic differential equations and the master equation. In: *Physical Review A* 31 (1985), Nr. 6, S. 3761 14, 47, 48
- [GD08] GRIFFITHS, David J. ; DICK, Gale: Introduction to quantum mechanics. In: *Physics Today* 48 (2008), Nr. 9, S. 94–94 12
- [Gio62] GIORDMAINE, JA: Mixing of light beams in crystals. In: *Physical Review Letters* 8 (1962), Nr. 1, S. 19 55
- [GK05] GERRY, Christopher ; KNIGHT, Peter: *Introductory quantum optics*. Cambridge university press, 2005 15, 16, 17, 18, 19, 22
- [Gla63] GLAUBER, Roy J.: Coherent and incoherent states of the radiation field. In: *Physical Review* 131 (1963), Nr. 6, S. 2766 17
- [GZ04] GARDINER, Crispin ; ZOLLER, Peter: *Quantum noise: A handbook of Markovian and non-Markovian quantum stochastic methods with applications to quantum optics*. Bd. 56. Springer Science & Business Media, 2004 14
- [HC80] HANSCH, T.W. ; COUILLAUD, B.: Laser frequency stabilization by polarization spectroscopy of a reflecting reference cavity. In: *Optics Communications* 35 (1980), Nr. 3, 441 - 444. [http://dx.doi.org/http://dx.doi.org/10.1016/0030-4018\(80\)90069-3](http://dx.doi.org/http://dx.doi.org/10.1016/0030-4018(80)90069-3). – DOI [http://dx.doi.org/10.1016/0030-4018\(80\)90069-3](http://dx.doi.org/10.1016/0030-4018(80)90069-3). – ISSN 0030-4018 64, 66, 69, 83, 116
- [HKEB06] HERZOG, Frank ; KUDIELKA, Klaus ; ERNI, Daniel ; BÄCHTOLD, Werner: Optical phase locking by local oscillator phase dithering. In: *Quantum Electronics, IEEE Journal of* 42 (2006), Nr. 10, S. 973–985 64, 66, 83, 91

## BIBLIOGRAPHY

---

- [HPJH09] HEURS, M. ; PETERSEN, I. R. ; JAMES, M. R. ; HUNTINGTON, E. H.: Homodyne locking of a squeezer. In: *Opt. Lett.* 34 (2009), Aug, Nr. 16, 2465–2467. <http://dx.doi.org/10.1364/OL.34.002465>. – DOI 10.1364/OL.34.002465 64, 68, 69, 83, 89, 110
- [HT75] HULSE, RA ; TAYLOR, JH: Discovery of a pulsar in a binary system. In: *Neutron stars, black holes, and binary X-ray sources* 48 (1975), S. 433 4
- [HWD<sup>+</sup>10] HEURS, M ; WEBB, JG ; DUNLOP, AE ; HARB, CC ; RALPH, TC ; HUNTINGTON, EH: Multiplexed communication over a high-speed quantum channel. In: *Physical Review A* 81 (2010), Nr. 3, S. 032325 62, 129
- [Jac99] JACKSON, John D.: *Classical electrodynamics*. Wiley, 1999 34
- [Jon47] JONES, R C.: A new calculus for the treatment of optical system. In: *J. Opt. Soc. Am* 37 (1947), Nr. 2, S. 107–112 35
- [Ken27] KENNARD, EH: Zur quantenmechanik einfacher Bewegungstypen. In: *Zeitschrift für Physik* 44 (1927), Nr. 4-5, S. 326–352 63
- [Ken08] KENYON, Ian R.: *The light fantastic: a modern introduction to classical and quantum optics*. Oxford University Press, USA, 2008 41
- [KL66] KOGELNIK, H ; LI, Tingye: Laser beams and resonators. In: *Proceedings of the IEEE* 54 (1966), Nr. 10, S. 1312–1329 9, 44, 45
- [L<sup>+</sup>98] LAM, Ping K. u. a.: *Applications of quantum electro-optic control and squeezed light*. Australian National University, 1998 14, 38
- [LLW<sup>+</sup>08] LANGRIDGE, JM ; LAURILA, T ; WATT, RS ; JONES, RL ; KAMINSKI, CF ; HULT, J: Cavity enhanced absorption spectroscopy of multiple trace gas species using a supercontinuum radiation source. In: *Optics Express* 16 (2008), Nr. 14, S. 10178–10188 5



- [LPS<sup>+</sup>98] LEVENSON, MD ; PALDUS, BA ; SPENCE, TG ; HARB, CC ; HARRIS JR, JS ; ZARE, RN: Optical heterodyne detection in cavity ring-down spectroscopy. In: *Chemical physics letters* 290 (1998), Nr. 4, S. 335–340 5
- [LYS61] LOUISELL, WH ; YARIV, A ; SIEGMAN, AE: Quantum Fluctuations and Noise in Parametric Processes. I. In: *Physical Review* 124 (1961), Nr. 6, S. 1646 53
- [Max61] MAXWELL, James C.: XLIV. On physical lines of force. In: *The London, Edinburgh, and Dublin Philosophical Magazine and Journal of Science* 21 (1861), Nr. 140, S. 281–291 2
- [McK08] MCKENZIE, Kirk: *Squeezing in the audio gravitational wave detection band*, Australian National University, Diss., 2008 15, 46, 56, 71
- [MLS<sup>+</sup>87] MILBURN, GJ ; LEVENSON, MD ; SHELBY, RM ; PERLMUTTER, SH ; DEVOE, RG ; WALLS, DF: Optical-fiber media for squeezed-state generation. In: *JOSA B* 4 (1987), Nr. 10, S. 1476–1489 53
- [MMG<sup>+</sup>05] MCKENZIE, Kirk ; MIKHAILOV, Eugeny E. ; GODA, Keisuke ; LAM, Ping K. ; GROSSE, Nicolai ; GRAY, Malcolm B. ; MAVALVALA, Nergis ; MCCLELLAND, David E.: Quantum noise locking. In: *Journal of Optics B: Quantum and Semiclassical Optics* 7 (2005), Nr. 10, S. S421 84
- [MSM<sup>+</sup>02] MCKENZIE, Kirk ; SHADDOCK, Daniel A. ; MCCLELLAND, David E. ; BUCHLER, Ben C. ; LAM, Ping K.: Experimental demonstration of a squeezing-enhanced power-recycled Michelson interferometer for gravitational wave detection. In: *Physical review letters* 88 (2002), Nr. 23, S. 231102 3, 99
- [New87] NEWTON, Isaac: *Philosophiae naturalis principia mathematica* (“Mathematical principles of natural philosophy”). In: *London (1687)* (1987) 3
- [PCK92] POLZIK, ES ; CARRI, J ; KIMBLE, HJ: Spectroscopy with squeezed light. In: *Physical review letters* 68 (1992), Nr. 20, S. 3020 5

## BIBLIOGRAPHY

---

- [PDGVHG92] PUTMAN, Constant A. ; DE GROOTH, Bart G. ; VAN HULST, Niek F. ; GREVE, Jan: A detailed analysis of the optical beam deflection technique for use in atomic force microscopy. In: *Journal of Applied Physics* 72 (1992), Nr. 1, S. 6–12 5
- [PHS<sup>+</sup>98] PALDUS, BA ; HARB, CC ; SPENCE, TG ; WILKE, B ; XIE, J ; HARRIS, JS ; ZARE, RN: Cavity-locked ring-down spectroscopy. In: *Journal of applied physics* 83 (1998), Nr. 8, S. 3991–3997 4
- [RSS<sup>+</sup>02] ROBINS, N. P. ; SLAGMOLEN, B. J. J. ; SHADDOCK, D. A. ; CLOSE, J. D. ; GRAY, M. B.: Interferometric, modulation-free laser stabilization. In: *Opt. Lett.* 27 (2002), Nov, Nr. 21, 1905–1907. <http://dx.doi.org/10.1364/OL.27.001905>. – DOI 10.1364/OL.27.001905 64, 83
- [Sch26] SCHRÖDINGER, Erwin: Der stetige Übergang von der Mikro-zur Makromechanik. In: *Naturwissenschaften* 14 (1926), Nr. 28, S. 664–666 63
- [Sch13] SCHWABL, Franz: *Quantenmechanik (QMI)*. Springer-Verlag, 2013 85
- [SH98] SVELTO, Orazio ; HANNA, David C.: *Principles of lasers*. Springer, 1998 43, 47, 52, 96
- [SHY<sup>+</sup>86] SLUSHER, R. E. ; HOLLBERG, L. W. ; YURKE, B. ; MERTZ, J. C. ; VALLEY, J. F.: Observation of Squeezed States Generated by Four-Wave Mixing in an Optical Cavity. In: *Phys. Rev. Lett.* 56 (1986), Feb, 788–788. <http://dx.doi.org/10.1103/PhysRevLett.56.788>. – DOI 10.1103/PhysRevLett.56.788 1, 53, 63
- [SRH<sup>+</sup>13] SCHACKERT, Flavius ; ROY, Ananda ; HATRIDGE, Michael ; DEVORET, Michel H. ; STONE, A D.: Three-Wave Mixing with Three Incoming Waves: Signal-Idler Coherent Attenuation and Gain Enhancement in a Parametric Amplifier. In: *Physical review letters* 111 (2013), Nr. 7, S. 073903 53
- [TW82] TAYLOR, Joseph H. ; WEISBERG, Joel M.: A new test of general relativity-Gravitational radiation and

- the binary pulsar PSR 1913+ 16. In: *The Astrophysical Journal* 253 (1982), S. 908–920 4
- [TW89] TAYLOR, Joseph H. ; WEISBERG, Joel M.: Further experimental tests of relativistic gravity using the binary pulsar PSR 1913+ 16. In: *The Astrophysical Journal* 345 (1989), S. 434–450 4
- [UBRR15] UPHOFF, Manuel ; BREKENFELD, Manuel ; REMPE, Gerhard ; RITTER, Stephan: Frequency splitting of polarization eigenmodes in microscopic Fabry–Perot cavities. In: *New Journal of Physics* 17 (2015), Nr. 1, S. 013053 115
- [Vah08] VAHLBRUCH, Henning: *Squeezed light for gravitational wave astronomy*, Gottfried Wilhelm Leibniz Universität Hannover Hannover, Germany, Diss., 2008 69
- [VCDS07] VAHLBRUCH, Henning ; CHELKOWSKI, Simon ; DANZMANN, Karsten ; SCHNABEL, Roman: Quantum engineering of squeezed states for quantum communication and metrology. In: *New Journal of Physics* 9 (2007), Nr. 10, S. 371 63
- [VKL<sup>+</sup>10] VAHLBRUCH, Henning ; KHALAIDOVSKI, Alexander ; LASTZKA, Nico ; GRÄF, Christian ; DANZMANN, Karsten ; SCHNABEL, Roman: The GEO 600 squeezed light source. In: *Classical and Quantum Gravity* 27 (2010), Nr. 8, S. 084027 1, 63
- [WKHW86] WU, Ling-An ; KIMBLE, HJ ; HALL, JL ; WU, Huifa: Generation of squeezed states by parametric down conversion. In: *Physical review letters* 57 (1986), Nr. 20, S. 2520 53
- [WM07] WALLS, Daniel F. ; MILBURN, Gerard J.: *Quantum optics*. Springer, 2007 5, 8, 39, 46, 48, 59, 85
- [WRH06] WEBB, James G. ; RALPH, Timothy C. ; HUNTINGTON, Elanor H.: Homodyne measurement of the average photon number. In: *Physical Review A* 73 (2006), Nr. 3, S. 033808 106

## BIBLIOGRAPHY

---

- [WUG<sup>+</sup>98] WILLKE, B ; UEHARA, N ; GUSTAFSON, EK ; BYER, RL ; KING, PJ ; SEEL, SU ; SAVAGE JR, RL u. a.: Spatial and temporal filtering of a 10-W Nd: YAG laser with a Fabry–Perot ring-cavity premode cleaner. In: *Optics letters* 23 (1998), Nr. 21, S. 1704–1706 110
- [YC83] YUEN, Horace P. ; CHAN, Vincent W.: Noise in homodyne and heterodyne detection. In: *Optics Letters* 8 (1983), Nr. 3, S. 177–179 33
- [Yue76] YUEN, Horace P.: Two-photon coherent states of the radiation field. In: *Physical Review A* 13 (1976), Nr. 6, S. 2226 1
- [Yue83] YUEN, Horace P.: Contractive States and the Standard Quantum Limit for Monitoring Free-Mass Positions. In: *Phys. Rev. Lett.* 51 (1983), Aug, 719–722. <http://dx.doi.org/10.1103/PhysRevLett.51.719>. – DOI 10.1103/PhysRevLett.51.719 1
- [Yur84] YURKE, Bernard: Use of cavities in squeezed-state generation. In: *Physical Review A* 29 (1984), Nr. 1, S. 408 13

## Acknowledgements

After more than five years of working on this thesis, it is time for me to draw a conclusion and to thank the people who accompanied me on my way.

Foremost, I would like to thank Prof. Dr. Karsten Danzmann as the head of the institute for providing this scientific environment. It was an honor for me to work at this institute especially in such exciting times.

My gratitude goes out to Juniorprof. Dr. Michèle Heurs for being my PhD advisor and mentor. Thank you for letting me be a part of this young Quantum Control group, for your continuous advice and helpful discussions throughout the course of my thesis and for the possibility to visit the UNSW in Canberra. I want to thank Prof. Dr. Elanor H. Huntington for the opportunity to gain experience in optics laboratory work as well as the Australian way of life. Without this collaboration and her systematic guidance I would have never learned so much about my own mathematical universe.

Of course, there were many, many people involved in the process of understanding, planing and realizing the experiment and every outcome based on that. The majority of the assembled components are in-house designed and built by the electronic and mechanical workshop staff: Thanks to all of you!

I would like to express my gratitude to Stefan, Vitus, Christoph and Henning for many helpful discussions and insightful comments. Even though you were not part of my immediate working group I could always come to you with my thoughts and questions. In this context I especially wish to thank Moritz for the assistance he provided during all stages of this research project.

My office mates Dirk and Max deserve a special thank you for being an important part of my work and private life. You guys even made the long office hours really enjoyable! Since our group has grown my appreciation also goes out to my neighbor office mates Bernd, Daniel and especially Kai for proofreading my thesis. In addition, I would like to thank Johannes for the continuous advice and assistance whenever I felt stuck. Thank you for enduring the discussions (and

## Acknowledgements

---

my justifications) about English and Physics!

A special gratitude goes to my parents Anita and Dieter. Without your help and loving support over all these years I would not be who/where I am today.

*Danke, dass ihr immer an mich und meine gemalten Bäume geglaubt habt!*

Last but not least I want to thank my wife Mirja for her patience, love, encouragement and editing assistance. I can't and won't imagine my life without you.

# Curriculum Vitae

## PERSONAL DATA

---

Name: Timo Denker  
Address: Sedanstraße 43  
30161 Hannover  
Nationality: German  
Date and place of birth: 30.05.1984, Minden

## ACADEMIC CAREER

---

10/2010 – 06/2016 PhD Thesis at Leibniz Universität Hannover  
Institute for gravitational physics  
AG Heurs – Quantum Control  
*High-precision metrology with  
high-frequency nonclassical light sources*

10/2004 – 07/2010 Diploma studies at Leibniz Universität Hannover  
Diploma thesis at Institute for quantum optics  
AG Rasel – CASI  
Cold Atom Sagnac Interferometer  
*Key technologies for atomic quantum sensors*

## EXTRA CURRICULAR ACTIVITIES

---

10/2012 – 07/2013 Managerial skills for a career outside university  
*Promotion plus+ qualifiziert*

02/2013 Seminar *Presentation Skills*

01/2012 Seminar *Write about Science*

08/2008 – 10/2008 Industrial placement: PTB Braunschweig  
*Niedrigdimensionale Elektronensysteme*

## COLLABORATIONS

---

02/2011 – present Member of *Ligo Scientific Collaboration* (LSC)

## Curriculum Vitae

---

10/2010 – 01/2011      Visit to UNSW Canberra  
*School of Engineering  
and Information Technology (SEIT)*

## **EDUCATION**

---

06/1994 – 06/2003      Ratsgymnasium Minden  
06/1990 – 06/1994      Grundschule Dankersen



# Compendium of publications

2016

- [1] Abbott B. P., ..., **T. Denker**, ..., et al.. Observation of Gravitational Waves from a Binary Black Hole Merger. *Phys. Rev. Lett.*, **116**(6),061102.
- [2] Abbott B. P., ..., **T. Denker**, ..., et al.. Astrophysical Implications of the Binary Black-Hole Merger GW150914. *Astrophys. J.*, **818**(2),L22.
- [3] Abbott B. P., ..., **T. Denker**, ..., et al.. Localization and broadband follow-up of the gravitational-wave transient GW150914. *eprint arXiv:*, 1602.08492, (astro-ph.HE).
- [4] Abbott B. P., ..., **T. Denker**, ..., et al.. GW150914: Implications for the stochastic gravitational wave background from binary black holes. *eprint arXiv:*, 1602.03847, (gr-qc).
- [5] Abbott B. P., ..., **T. Denker**, ..., et al.. Calibration of the Advanced LIGO detectors for the discovery of the binary black-hole merger GW150914. *eprint arXiv:*, 1602.03845, (gr-qc).
- [6] Abbott B. P., ..., **T. Denker**, ..., et al.. Characterization of transient noise in Advanced LIGO relevant to gravitational wave signal GW150914. *eprint arXiv:*, 1602.03844, (gr-qc).
- [7] Abbott B. P., ..., **T. Denker**, ..., et al.. Observing gravitational-wave transient GW150914 with minimal assumptions. *eprint arXiv:*, 1602.03843, (gr-qc).
- [8] Abbott B. P., ..., **T. Denker**, ..., et al.. The Rate of Binary Black Hole Mergers Inferred from Advanced LIGO Observations Surrounding GW150914. *eprint arXiv:*, 1602.03842, (astro-ph.HE).
- [9] Abbott B. P., ..., **T. Denker**, ..., et al.. Tests of general relativity with GW150914. *eprint arXiv:*, 1602.03841, (gr-qc).
- [10] Abbott B. P., ..., **T. Denker**, ..., et al.. Properties of the binary black hole merger GW150914. *eprint arXiv:*, 1602.03840, (gr-qc).
- [11] Abbott B. P., ..., **T. Denker**, ..., et al.. GW150914: First results from the search for binary black hole coalescence with Advanced LIGO. *eprint arXiv:*, 1602.03839, (gr-qc).

- [12] Abbott B. P., ..., **T. Denker**, ..., et al.. GW150914: The Advanced LIGO Detectors in the Era of First Discoveries. *eprint arXiv:*, 1602.03838, (gr-qc).
- [13] Adrian-Martinez, S., ..., **T. Denker**, ..., et al.. High-energy Neutrino follow-up search of Gravitational Wave Event GW150914 with ANTARES and IceCube. *eprint arXiv:*, 1602.05411, (astro-ph.HE).
- [14] Aasi, J., ..., **T. Denker**, ..., et al.. Search of the Orion spur for continuous gravitational waves using a loosely coherent algorithm on data from LIGO interferometers. *Phys. Rev.*, **D93**(4),042006.
- [15] Aasi, J., ..., **T. Denker**, ..., et al.. First low frequency all-sky search for continuous gravitational wave signals. *Phys. Rev.*, **D93**(4),042007.

## 2015

- [1] **T. Denker**, D. Schütte, M. H. Wimmer, T. A. Wheatley, E. H. Huntington, and M. Heurs. Utilizing weak pump depletion to stabilize squeezed vacuum states. *Opt. Express*, **23**(13),16517.
- [2] Aasi, J., ..., **T. Denker**, ..., et al.. Advanced LIGO. *Class. Quant. Grav.*, **32**,074001.
- [3] Aasi, J., ..., **T. Denker**, ..., et al.. Directed search for gravitational waves from Scorpius X-1 with initial LIGO data. *Phys. Rev.*, **D91**(6),062008.
- [4] Aasi, J., ..., **T. Denker**, ..., et al.. Characterization of the LIGO detectors during their sixth science run. *Class. Quant. Grav.*, **32**(11),115012.
- [5] Aasi, J., ..., **T. Denker**, ..., et al.. Searches for continuous gravitational waves from nine young supernova remnants. *Astrophys J.*, **813**(1),39.
- [6] Aasi, J., ..., **T. Denker**, ..., et al.. Narrow-band search of continuous gravitational-wave signals from Crab and Vela pulsars in Virgo VSR4 data. *Phys. Rev.*, **D91**(2),022004.
- [7] Aasi, J., ..., **T. Denker**, ..., et al.. Searching for stochastic gravitational waves using data from the two colocated LIGO Hanford detectors. *Phys. Rev.*, **D91**(2),022003.

---

## 2014

- [1] Aartsen, M. G., ..., **T. Denker**, ..., et al.. Multimessenger search for sources of gravitational waves and high-energy neutrinos: Initial results for LIGO-Virgo and IceCube. *Phys. Rev.*, **D90**(10),102002.
- [2] Aasi, J., ..., **T. Denker**, ..., et al.. Application of a Hough search for continuous gravitational waves on data from the fifth LIGO science run. *Class. Quant. Grav.*, **31**,085014.
- [3] Aasi, J., ..., **T. Denker**, ..., et al.. Gravitational waves from known pulsars: results from the initial detector era. *Astrophys. J.*, **785**,119.
- [4] Aasi, J., ..., **T. Denker**, ..., et al.. First Searches for Optical Counterparts to Gravitational-wave Candidate Events. *Astrophys. J. Suppl.*, **211**,7.
- [5] Aasi, J., ..., **T. Denker**, ..., et al.. Constraints on cosmic strings from the LIGO-Virgo gravitational-wave detectors. *Phys. Rev. Lett.*, **122**,131101.
- [6] Aasi, J., ..., **T. Denker**, ..., et al.. Search for gravitational wave ringdowns from perturbed intermediate mass black holes in LIGO-Virgo data from 2005-2010. *Phys. Rev.*, **D89**(10),102006.
- [7] Aasi, J., ..., **T. Denker**, ..., et al.. Methods and results of a search for gravitational waves associated with gamma-ray bursts using the GEO600, LIGO, and Virgo detectors. *Phys. Rev.*, **D89**(12),122004.
- [8] Aasi, J., ..., **T. Denker**, ..., et al.. First all-sky search for continuous gravitational waves from unknown sources in binary systems. *Phys. Rev.*, **D90**(6),062010.
- [9] Aasi, J., ..., **T. Denker**, ..., et al.. Search for gravitational waves associated with  $\gamma$ -ray bursts detected by the Interplanetary Network. *Phys. Rev. Lett.*, **113**(1),011102.
- [10] Aasi, J., ..., **T. Denker**, ..., et al.. Search for gravitational radiation from intermediate mass black hole binaries in data from the second LIGO-Virgo joint science run. *Phys. Rev.*, **D89**(12),122003.
- [11] Aasi, J., ..., **T. Denker**, ..., et al.. Implementation of an  $F$ -statistic all-sky search for continuous gravitational waves in Virgo VSR1 data. *Class. Quant. Grav.*, **31**,165014.
- [12] Aasi, J., ..., **T. Denker**, ..., et al.. The NINJA-2 project: Detecting and characterizing gravitational waveforms modelled using numerical binary black hole simulations. *Class. Quant. Grav.*, **31**,115004.

## Compendium of publications

---

- [13] Aasi, J., ..., **T. Denker**, ..., et al.. Improved Upper Limits on the Stochastic Gravitational-Wave Background from 2009-2010 LIGO and Virgo Data. *Phys. Rev. Lett.*, **113**(23),231101.
- [14] Acernese F., ..., **T. Denker**, ..., et al.. Concepts and research for future detectors. *Gen. Rel. Grav.*, **46**(5),1700.

## 2013

- [1] Aasi, J., ..., **T. Denker**, ..., et al.. Directed search for continuous gravitational waves from the Galactic center. *Phys. Rev.*, **D88**(10),102002.
- [2] Aasi, J., ..., **T. Denker**, ..., et al.. Search for long-lived gravitational-wave transients coincident with long gamma-ray bursts. *Phys. Rev.*, **D88**(12),122004.
- [3] Aasi, J., ..., **T. Denker**, ..., et al.. Prospects for Observing and Localizing Gravitational-Wave Transients with Advanced LIGO and Advanced Virgo. *eprint arXiv.*, 1304.0670, (gr-qc).
- [4] Aasi, J., ..., **T. Denker**, ..., et al.. Enhancing the sensitivity of the LIGO gravitational wave detector by using squeezed states of light. *Nature Photon.*, 7, 613-619.